



MINISTÉRIO DA CIÊNCIA, TECNOLOGIA E INOVAÇÃO
INSTITUTO NACIONAL DE PESQUISAS ESPACIAIS

sid.inpe.br/mtc-m21b/2016/01.19.10.55-TDI

USING MULTI-ANGLE MODIS DATA TO OBSERVE VEGETATION DYNAMICS IN THE AMAZON FOREST

Yhasmin Mendes de Moura

Doctorate Thesis Course Graduate in Remote Sensing, advised by Drs. Lênio Soares Galvão and João Roberto dos Santos, approved in december 08, 2015.

URL of the original document:

[<http://urlib.net/8JMKD3MGP3W34P/3L2FEBH>](http://urlib.net/8JMKD3MGP3W34P/3L2FEBH)

INPE
São José dos Campos
2015

PUBLISHED BY:

Instituto Nacional de Pesquisas Espaciais - INPE

Gabinete do Diretor (GB)

Serviço de Informação e Documentação (SID)

Caixa Postal 515 - CEP 12.245-970

São José dos Campos - SP - Brasil

Tel.:(012) 3208-6923/6921

Fax: (012) 3208-6919

E-mail: pubtc@sid.inpe.br

**COMMISSION OF BOARD OF PUBLISHING AND PRESERVATION
OF INPE INTELLECTUAL PRODUCTION (DE/DIR-544):****Chairperson:**

Marciana Leite Ribeiro - Serviço de Informação e Documentação (SID)

Members:

Dr. Gerald Jean Francis Banon - Coordenação Observação da Terra (OBT)

Dr. Amauri Silva Montes - Coordenação Engenharia e Tecnologia Espaciais (ETE)

Dr. André de Castro Milone - Coordenação Ciências Espaciais e Atmosféricas
(CEA)

Dr. Joaquim José Barroso de Castro - Centro de Tecnologias Espaciais (CTE)

Dr. Manoel Alonso Gan - Centro de Previsão de Tempo e Estudos Climáticos
(CPT)

Dr^a Maria do Carmo de Andrade Nono - Conselho de Pós-Graduação

Dr. Plínio Carlos Alvalá - Centro de Ciência do Sistema Terrestre (CST)

DIGITAL LIBRARY:

Dr. Gerald Jean Francis Banon - Coordenação de Observação da Terra (OBT)

Clayton Martins Pereira - Serviço de Informação e Documentação (SID)

DOCUMENT REVIEW:

Simone Angélica Del Ducca Barbedo - Serviço de Informação e Documentação
(SID)

Yolanda Ribeiro da Silva Souza - Serviço de Informação e Documentação (SID)

ELECTRONIC EDITING:

Marcelo de Castro Pazos - Serviço de Informação e Documentação (SID)

André Luis Dias Fernandes - Serviço de Informação e Documentação (SID)



MINISTÉRIO DA CIÊNCIA, TECNOLOGIA E INOVAÇÃO
INSTITUTO NACIONAL DE PESQUISAS ESPACIAIS

sid.inpe.br/mtc-m21b/2016/01.19.10.55-TDI

USING MULTI-ANGLE MODIS DATA TO OBSERVE VEGETATION DYNAMICS IN THE AMAZON FOREST

Yhasmin Mendes de Moura

Doctorate Thesis Course Graduate in Remote Sensing, advised by Drs. Lênio Soares Galvão and João Roberto dos Santos, approved in december 08, 2015.

URL of the original document:

[<http://urlib.net/8JMKD3MGP3W34P/3L2FEBH>](http://urlib.net/8JMKD3MGP3W34P/3L2FEBH)

INPE
São José dos Campos
2015

Cataloging in Publication Data

Moura, Yhasmin Mendes de.

M865u Using multi-angle modis data to observe vegetation dynamics in the amazon forest / Yhasmin Mendes de Moura. – São José dos Campos : INPE, 2015.
xxii + 85 p. ; (sid.inpe.br/mtc-m21b/2016/01.19.10.55-TDI)

Thesis (Doctorate in Remote Sensing) – Instituto Nacional de Pesquisas Espaciais, São José dos Campos, 2015.

Guiding : Drs. Lênio Soares Galvão and João Roberto dos Santos.

1. Amazon. 2. Anisotropy. 3. MODIS. 4. MAIAC. 5. Multi-angle remote sensing. I.Title.

CDU 528.8:630



Esta obra foi licenciada sob uma Licença [Creative Commons Atribuição-NãoComercial 3.0 Não Adaptada](#).


This work is licensed under a [Creative Commons Attribution-NonCommercial 3.0 Unported License](#).

Aluno (a): **Yhasmin Mendes de Moura**

Título: " USING MULTI-ANGLE MODIS DATA TO OBSERVE VEGETATION DYNAMICS IN THE AMAZON FOREST"

Aprovado (a) pela Banca Examinadora
em cumprimento ao requisito exigido para
obtenção do Título de **Doutor(a)** em
Sensoriamento Remoto

Dr. Lênio Soares Galvão



Presidente / Orientador(a) / INPE / SJCampos - SP

Dr. João Roberto dos Santos



Orientador(a) / INPE / SJCampos - SP

Dra. Liana Oighenstein Anderson



Membro da Banca / CEMADEN / São José dos Campos - SP

Dr. Alexei I. Lyapustin



Convidado(a) / NASA / Washington, D.C. - USA

Dr. Laerte Guimarães Ferreira Júnior



Convidado(a) / UFG / Goiânia - GO

Este trabalho foi aprovado por:

() **maioria simples**

(x) **unanimidade**

São José dos Campos, 08 de Dezembro de 2015

*“Oh, you can’t help that,” said the cat:
“We’re all mad here. I’m mad. You’re mad.”
“How do you know I’m mad?” said Alice.
“You must be,” said the cat,
“or you wouldn’t have come here.”*

Lewis Carrol, Alice in Wonderland

ACKNOWLEDGMENTS

I would like to thank CNPq (National Counsel of Technological and Scientific Development) and CAPES (Brazilian Federal Agency for the support and Evaluation of Graduate Education) for the scholarship that funded my PhD and provided me the opportunity to spend a year at Oregon State University (OSU).

Thank you to my committee, especially my advisors Drs. Lenio Soares Galvão and João Roberto dos Santos for their support and helpful insights during all these years. Thanks also to the Instituto Nacional de Pesquisas Espaciais (INPE), Divisão de Sensoriamento Remoto and to Oregon State University for all the scientific and logistic support.

Special thanks to Dr. Alexei Lyapustin, for all the assistance with the MAIAC data, and to Drs. Liana O. Anderson, Luiz Aragão, Egídio Arai and Michael Keller for helpful comments in the development of this research. Also, would like to thank the Sustainable Landscapes Brazil project supported by the Brazilian Agricultural Research Corporation (EMBRAPA), the US Forest Service, and USAID, and the US Department of State, for the LiDAR data used in this study.

I'm grateful to my friends, which directly or indirectly, gave me all the support I need during these years.

Last, but not least, I'm truly grateful to my partner in science and in life, Thomas.

ABSTRACT

Seasonality and drought in Amazon rainforests have been controversially discussed in the literature, partially due to a limited ability of current remote sensing techniques to detect drought impacts on tropical vegetation. Detailed knowledge of vegetation structure is required for accurate modeling of terrestrial ecosystem. However, direct measurements of the three dimensional distribution of canopy elements using LiDAR are not widely available, especially in the Amazon region. This thesis explores a novel multi-angle remote sensing approach to determine changes in vegetation structure from differences in directional scattering (anisotropy) observed from the analysis of Moderate Resolution Imaging Spectroradiometer (MODIS) data, atmospherically corrected using the Multi-Angle Implementation Atmospheric Correction Algorithm (MAIAC). Chapter 1 presents a general overview of the topic, followed by a theoretical background of the most important types of remote sensing data used in this thesis (Chapter 2). Chapter 3 describes the retrieval of BRDF from MODIS data. Chapters 4 and 5 present two distinct approaches using multi-angular MODIS data. In Chapter 4, the potential of using MODIS anisotropy for modeling vegetation roughness from directional scattering of visible and near-infrared (NIR) reflectance was evaluated across different forest types. Derived estimates were compared to independent measures of canopy roughness (entropy) obtained from the: 1) airborne laser scanning (ALS), 2) spaceborne LiDAR Geoscience Laser Altimeter System (GLAS), and 3) spaceborne SeaWinds/QSCAT. GLAS-derived entropy presented strong seasonality and varied between different forest types. Results from Chapter 4 showed linear relationships between MODIS-derived anisotropy and ALS-derived entropy with a coefficient of determination (r^2) of 0.54 and a root mean squared error (RMSE) of 0.11, even in high biomass regions. Significant relationships were also obtained between MODIS-derived anisotropy and GLAS-derived entropy ($0.52 \leq r^2 \leq 0.61$; $p < 0.05$), with similar slopes and offsets found throughout the season. The RMSE varied between 0.26 and 0.30 (units of anisotropy). The relationships between the MODIS-derived anisotropy and backscattering measurements (σ^0) from SeaWinds/QuikSCAT were also significant ($r^2=0.59$, RMSE=0.11). Results also showed a strong linear relationship of the anisotropy with field- ($r^2=0.70$) and LiDAR-based ($r^2=0.88$) estimates of leaf area index (LAI). In Chapter 5, the method was used to analyze seasonal changes in the Amazonian forests, comparing them to spatially explicit estimates of onset and length of dry season obtained from the Tropical Rainfall Measurement Mission (TRMM). The results of Chapter 5 showed an increase in vegetation greening during the beginning of dry season (7% of the basin), which was followed by a decline (browning) later during the dry season (5% of the basin). Anomalies in vegetation browning were particularly strong during the 2005 and 2010 drought years (10% of the basin). The magnitude of seasonal changes was significantly affected by regional differences in onset and duration of the

dry season. Seasonal changes were much less pronounced when assuming a fixed dry season from June through September across the Amazon basin. The findings reconcile remote sensing studies with field-based observations and model results, supporting the argument that tropical vegetation growth increases during the beginning of the dry season, but declines after extended dry season and drought periods. Overall, we concluded that multi-angle approaches, as the one used in this thesis, are suitable to extrapolate measures of canopy structure across different forest types, and may help quantify drought tolerance and seasonality in the Amazonian forests.

UTILIZAÇÃO DE DADOS MULTIANGULARES DO SENSOR MODIS PARA ANÁLISE DA DINÂMICA DA VEGETAÇÃO NA FLORESTA AMAZÔNICA

RESUMO

Os temas sazonalidade e secas severas na Amazônia vêm sendo discutidos de maneira controversa na literatura, parcialmente devido à habilidade limitada das atuais técnicas de sensoriamento remoto para detecção e análise da resposta de florestas tropicais a estes eventos. O conhecimento detalhado da estrutura da vegetação constitui um dado fundamental para melhoria da modelagem dos ecossistemas terrestres. No entanto, medições diretas da distribuição tridimensional dos elementos do dossel, por exemplo, oriundas de LiDAR, não são disponíveis amplamente, especialmente na região Amazônica. Neste estudo, é proposta uma abordagem de sensoriamento remoto multiangular para avaliar mudanças na estrutura da vegetação a partir de diferenças do espalhamento direcional (anisotropia) observado pelo Moderate Resolution Imaging Spectroradiometer (MODIS), que teve seus dados atmosféricamente corrigidos usando o Multi-Angle Implementation Atmospheric Correction Algorithm (MAIAC). O Capítulo 1 apresenta uma visão geral do problema, seguido de uma base teórica sobre os mais importantes temas e dados de sensoriamento remoto usados nesta tese (Capítulo 2). O Capítulo 3 descreve o modelo utilizado para recuperação dos dados da Função de Distribuição da Reflectância Bidirecional (BRDF) a partir dos dados MODIS. Os Capítulos 4 e 5 apresentam duas abordagens distintas usando dados multiangulares do MODIS. No Capítulo 4 foi avaliado o potencial dos dados de anisotropia de superfície para modelar a rugosidade dos dosséis através do espalhamento direcional nas bandas de reflectância do visível e infravermelho próximo sobre diferentes tipologias florestais. Foram efetuadas comparações entre os dados de anisotropia em relação à medidas independentes de rugosidade de dosséis (entropia) obtidos de dados: 1) LiDAR aerotransportado (ALS), 2) LiDAR orbital do Geoscience Laser Altimeter System (GLAS), e 3) radar orbital do SeaWinds/QSCAT. Dados de entropia do GLAS apresentaram forte sazonalidade entre as tipologias florestais analisadas. Os resultados mostraram uma relação linear entre os dados de anisotropia derivados do sensor MODIS com os dados de entropia estimados do LiDAR aerotransportado com coeficiente de determinação (r^2) de 0.54 e erro médio quadrático (RMSE) de 0.11, mesmo em regiões de floresta densa. Relações significantes foram também obtidas entre anisotropia derivada do MODIS e entropia derivada do GLAS ($0.52 \leq r^2 \leq 0.61$; $p < 0.05$), com inclinações e interceptos aproximadamente similares ao longo de diferentes meses. O RMSE variou entre 0.26 e 0.30 (unidades de entropia). A correlação entre anisotropia do MODIS com medidas de retroespalhamento (σ^0) do sensor SeaWinds/QuikSCAT foi estatisticamente significativa ($r^2=0.59$, RMSE=0.11). Os resultados também mostraram

uma forte correlação linear entre os dados de anisotropia e as estimativas de índice de área foliar (LAI) obtidas em campo ($r^2=0.70$) e a partir de dados LiDAR ($r^2=0.88$). No Capítulo 5, analisou-se as variações sazonais das florestas Amazônicas, em que foram calculadas estimativas espacialmente explícitas do início e duração da estação seca na região utilizando dados do Tropical Rainfall Measurement Mission (TRMM). Os resultados mostraram um aumento em verdejamento da vegetação (“*greening*”) durante o início da estação seca (7% da bacia), seguido de um subsequente declínio (“*browning*”) no final da estação seca (~5% da bacia). As anomalias negativas (“*browning*”) foram particularmente mais fortes durante os anos de seca extrema na região, em 2005 e 2010 (~10% da bacia). Os resultados mostraram que a magnitude dessas mudanças sazonais pode ser significativamente afetada pelas diferenças regionais de início e duração da estação seca. Mudanças sazonais foram muito menos pronunciadas quando se assumiu um período fixo de estação seca (junho até setembro) sobre a bacia Amazônica. Os resultados reconciliam estudos baseados em dados de sensoriamento remoto com observações de campo e modelagem, uma vez que fornecem uma base mais sólida sobre o argumento de que a vegetação tropical aumenta seu crescimento durante o início da estação seca, mas sofre um declínio com o seu prolongamento, e especialmente após períodos de secas severas. Como conclusão geral, a abordagem multiangular utilizada neste trabalho se mostrou satisfatória, permitindo a extrapolação de estimativas estruturais do dossel sobre diferentes tipologias florestais, podendo auxiliar na quantificação sobre os impactos e resiliência das florestas Amazônicas em relação a ocorrências de secas severas.

LIST OF FIGURES

Pág.

Figure 2.1. Illustration for the land surface reflectance anisotropy. Specular scattering, as sunlint are also observed where forward scattering or soil elements are presented. Volumetric scattering, by finite scatterers (leaves or canopies) have anisotropic reflectance. Geometric scattering, given by shadow-casting of three dimensional elements, for example trees or brushland. Source: Adapted from Strahler et al., 1994. ... 5

Figure 2.2. Diagram of different geometry acquisitions over vegetated surfaces. 1) backscattering: represents the configuration where the sensor direction is the same as the incident light (sun); 2) nadir: represents the direction pointing directly below a location, orthogonal to a horizontal flat surface; and 3) forward scattering: where the sensor and sun are in opposite direction. 8

Figure 2.3. Block-diagram of MAIAC algorithm. Source: Adapted from LYAPUSTIN et al., 2008. 11

Figure 2.4. Illustration of the conceptual basis of LiDAR remote sensing. At the left, the intersection of the laser illumination area, or footprint, with a portion of a simplified tree crown, is represented. At the right, the hypothetical return signal (the lidar waveform) recorded by the sensor over the area is shown. By subtracting the range of the ground (last return) from the first detectable canopy return (first return), the canopy height is determined. Source: Adapted from (LEFSKY et al., 2002) 13

Figure 3.1. Modeled BRDF surface for a 1x1 km area of Amazon forest (65°0'0" W, 5°0'0" S) for red reflectance (a), NIR reflectance (c) and EVI (e). The black dots represent the actual MODIS observations accumulated over a 14-day period. The blue dot represents the modeled forward scatter direction (darkspot), while the red dot represents the modeled backscatter direction (hotspot). Figures b, d and f show a time series of anisotropy (red, NIR and EVI, respectively) using the mean time series of MODIS tile h12v09. Sun Zenith Angles (SZA) varied between 45° and 25° degrees to investigate the sensitivity with respect to the sun-sensor configuration. 22

Figure 3.2. Temporal variability of the standard deviation (σ_{BRDF}) between observed and modeled MAIAC reflectance (red and NIR). The graph represents an area of 100 x 100 km to obtain sufficient statistics given high cloud cover in the Amazon (65°0'0" W, 5°0'0" S).....	24
Figure 3.3. Spatial variability of the standard deviation between observed and modeled MAIAC EVI in (a) June and (b) September. Data were averaged over a 30-day period to obtain sufficient statistics given high cloud cover in the Amazon. The Amazon delimitation used in this study follows the definition proposed by EVA et al., 2005....	24
Figure 4.1. Location of the study area within the Amazon basin. The inset shows the Geoscience Laser Altimeter System (GLAS) coverage (strings), airborne laser scanning (ALS) data acquisition and the available field inventory plots across the Xingu basin.	31
Figure 4.2. Vegetation cover map adapted from IBGE (2004) in the left and diagrams of height estimates from ALS LiDAR data in the right to illustrate structural variation between the three predominant forest types in the study area (Dse, Asc and Fse). Each Airborne Laser Scanning (ALS) plot represents an area of 100 m x100 m to describe the heights values in the three different forests.	37
Figure 4.3. Canopy volume models (CVMs) based on the Airborne Laser Scanning (ALS) for (a) Dense ombrophilous forest (Dse); (b) Open ombrophilous Forest (Asc); and (c) Semi-deciduous forest (Fse).	38
Figure 4.4. Seasonal profiles of GLAS-derived entropy for the three different forest types of the study area. GLAS data were obtained only for the months indicated in the x-axis. Just for reference, the shaded area represents the quarter when the Airborne Laser Scanning (ALS) data were collected in 2012.	39
Figure 4.5. MODIS-derived anisotropy images during (a) March, (b) June and (c) October of 2006 to illustrate seasonal and spatial changes in multi-angle reflectance across the Xingu basin.	40
Figure 4.6. Relationship between MODIS-derived anisotropy and ALS-derived entropy (or canopy roughness).	41

Figure 4.7. Relationship between MODIS-derived anisotropy and GLAS-derived entropy using observations for (a) March, (b) June and (c) October of 2006.	42
Figure 4.8. Relationship between MODIS-derived anisotropy and backscattering (σ_0) measurements from SeaWinds/QSCAT over Amazonian tropical forests considering the period 2001 to 2009.....	43
Figure 4.9. Time series profiles of MODIS-derived (a) GLAS entropy estimated using the regression model of Figure 4.7c, and (b) MODIS-derived SeaWinds/QuikSCAT backscattering (σ_0) from the model of Figure 4.8. Results are shown as spatial average for Dense (Dse) and Open (Asc) Ombrophilous Forests and the Semi-Deciduous Forest (Fse) between 2000 and 2012 for the Xingu basin.....	44
Figure 5.1. The first principal component of anisotropy between 2000 and 2012. The droughts years 2005 and 2010 were excluded. The locations of the field and LiDAR estimates of LAI are shown. LiDAR estimates were obtained from Sustainable Landscape Project in three locations: Adolpho Ducke Forest Reserve, Amazonas state, Brazil (); Rio Branco municipality, Acre State, Brazil () and Tapajós National Forest, Pará State, Brazil (). The other field estimates of LAI were collected from the literature: Malhi et al. (2009) (•), Domingues et al. (2005) (○), Doughty and Goulden, (2008c) (*), Juárez et al. (2009) (x), Andreae et al., (2002) (□), Zanchi et al., (2009) (◇), Restrepo-Coupe et al., (2013) (Δ), Figuera et al., (2011) (<), Scurlock et al., (2001) (>), Galvao et al., (2011) (+).....	54
Figure 5.2. Relationship between anisotropy and LAI; a) from field values collected in the literature (see Figure 2), and b) from LiDAR estimates. c) Relationship between directionally normalized (nadir) EVI and LAI. The correlations were performed using the dates described in the field data with the closest MODIS acquisitions available. The location of the plots are provided in Figure 5.1. RMSE for Figures 5.2a and 5.2b were 0.08 and 0.02 (units of anisotropy), respectively.	56
Figure 5.3. Monthly estimates of water deficit (in mm month ⁻¹), based on TRMM observations from 1998 to 2012. Areas with low water deficit are shown in blue, whereas the red color indicates high water deficits; areas with no water deficit are presented without color.	57

Figure 5.4. Beginning (a) and length (b) of dry season across the Amazon calculated on per pixel basis using monthly water deficits. This approach was performed for each year separately in order to consider inter-annual variability. The figure shows mean onset and length of dry season for all years.	58
Figure 5.5. (a) Spatial distribution of changes in anisotropy normalized by the standard deviation using a dry season period from June to September (for all years between 2000 and 2012, except 2005 and 2010). The gray regions represents no dry season or non-forested areas. (b) Spatial distribution of changes in anisotropy normalized by the standard deviation using specific begin and end of dry season based on the water deficit maps. Figures c and d show the corresponding changes in greening (blue bars) and browning (red bars) by months of dry season ($p = 0.05$). The dashed lines in Figures c and d represent the net changes in LAI (averaged across the basin) modelled by the linear relationship between anisotropy and LAI (Figure 5.2a). The solid line shows the corresponding estimates based on the model derived from LiDAR (Figure 5.2b).....	60
Figure 5.6. (a) Spatial distribution of changes in non-normalized anisotropy normalized using a dry season period from June to October (for all years, except 2005 and 2010). The gray regions represents no dry season or non-forested areas. (b) Spatial distribution of changes in non-normalized anisotropy using specific begin and end of dry season based on the water deficit maps.....	61
Figure 5.7. Spatial distribution of the standardized anomalies in anisotropy for 2005 (a) and 2010 (b), considering specifically begin and end of dry season (based on the water deficit maps). The gray regions represents no dry season or non-forested areas. Figures c and d show the corresponding anomalies in greening (blue bars) and browning (red bars) by months into dry season ($p = 0.05$). Circles represents an approximation of the epicenters of the droughts described by Lewis et al. (2011). The dashed lines in Figures c and d represent the anomalies in LAI (averaged across the basin) modelled by the linear relationship between anisotropy and LAI (Figure 5.2a). The solid line shows the corresponding estimates based on the model derived from LiDAR (Figure 5.2b).....	62

LIST OF TABLES

	<u>Pág.</u>
Table 4.1. Characteristics of the airborne laser scanning (ALS) data acquired over Dense Ombrophilous (Dse), Open Ombrophilous (Asc) and Semi-Deciduous (Fse) Forests in the Brazilian Amazon.	32
Table 4.2. Floristic and structural metrics calculated from field inventory data (http://mapas.cnpm.embrapa.br/paisagenssustentaveis/) for Dense Ombrophilous Forest (Dse), Open Ombrophilous Forest (Asc) and Semi-Deciduous Forest (Fse). The mean leaf area index (LAI), determined from Airborne Laser Scanning (ALS), is indicated in the last column of the table.....	38

LIST OF ABBREVIATIONS

ALS = Airborne Laser Scanning
AOT = Aerosol Optical Thickness
ATBD = Algorithm Theoretical Basis Document
BA = Basal Area
BRDF = Bidirectional Reflectance Distribution Function
BRF = Bi-directional Reflectance Factor
CM = Cloud Mask
CVM = Canopy Volume Model
DBH = Diameter at Breast Height
DTM = Digital Terrain Model
EMBRAPA = Empresa Brasileira de Pesquisa Agropecuária
EOS = Earth Observing System
EVI = Enhanced Vegetation Index
GEDI = Global Ecosystem Dynamics
GLAS = Geoscience Laser Altimeter System
HT = Mean Height
ICESat = Ice, Cloud, and land Elevation Satellite
LAI = Leaf Area Index
LiDAR = Light Detection and Ranging
MAIAC = Multi-Angle Implementation of Atmospheric Correction
MCH = Mean Canopy Height
MISR = Multi-angle Imaging SpectroRadiometer
MODIS = Moderate Resolution Imaging Spectroradiometer
NASA = National Aeronautics and Space Administration
NDVI = Normalized Difference Vegetation Index
NIR = Near Infrared
PAR = Photosynthetically Active Radiation

PC = Principal Component

RAA = Relative Azimuth Angle

RMSE = Root-Mean-Square Error

RTLS = Ross-Thick Li-Sparse

SD = Standard Deviation

SR = Surface Reflectance

SST = Sea Surface Temperature

SZA = Solar Zenith Angle

TMS = Time Series

TRMM = Tropical Rainfall Measuring Mission

USAID = United States Agency for International Development

VI's = Vegetation Indices

VZA = View Zenith Angle

CONTENTS

1	INTRODUCTION.....	1
2	THEORETICAL BACKGROUND.....	5
2.1.	Directional scattering in vegetated surfaces.....	5
2.2.	Moderate Resolution Imaging Spectroradiometer (MODIS).....	9
2.3.	Multi-Angle Implementation of Atmospheric Correction (MAIAC)	10
2.4.	Light Detection and Ranging (LiDAR).....	12
3	A NEW APPROACH TO CHARACTERIZE ANISOTROPY SURFACE REFLECTANCE FROM MULTI-ANGLE MODIS/MAIAC DATA.....	17
3.1.	BRDF retrievals from MODIS/MAIAC	18
4	VALIDATION OF VEGETATION STRUCTURE DERIVED FROM ANISOTROPY ACROSS DIFFERENT SCALES.....	27
4.1.	Introduction	27
4.2.	Material and Methods	30
4.2.1.	Study area.....	30
4.2.2.	Field inventory data.....	31
4.2.3.	Airborne Laser Scanning (ALS) data.....	32
4.2.4.	GLAS/ICESat data and structural metrics from vertical profiles	33
4.2.5.	SeaWinds/QuikSCAT data.....	35
4.2.6.	Determination of surface anisotropy from multi-angle MODIS data	36
4.3.	Results	36
4.4.	Discussion	44
4.5.	Conclusions	47
5	USE OF MULTI-ANGLE MODIS ANISOTROPY TO STUDY SEASONAL AND DROUGHT EFFECTS IN THE AMAZONIAN FORESTS	49

5.1. Introduction	49
5.2. Material and Methods	51
5.2.1. LiDAR and field based estimates of Leaf Area	51
5.2.2. Estimates onset and duration of Amazon dry seasons	52
5.3. Results	53
5.4. Discussion	63
5.5. Conclusions	67
6 SUMMARY AND FINAL REMARKS	69
REFERENCES	71

1 INTRODUCTION

Satellite-remote sensing is the only practical way to observe Amazon vegetation and ecosystem dynamics at useful spatial and temporal scales (SHUKLA et al., 1990). Since its launch in 2000, NASA's Moderate Resolution Imaging Spectroradiometer (MODIS) has been the workhorse of Amazon remote sensing (HILKER et al., 2014; HUETE et al., 2002). However, considerable deficiencies in estimation of atmospheric aerosol loadings (SAMANTA et al., 2010, 2012b) and cloud screening (HILKER et al., 2012b) over tropical regions (ASNER; ALENCAR, 2010; HILKER et al., 2012b; SAMANTA et al., 2012b; ZELAZOWSKI et al., 2011) have led to conflicting findings. Over the last decade, the Amazon region has experienced two severe droughts, one in 2005 and another in 2010 (MARENGO et al., 2011). Saleska et al. (2007) reported an increase in greenness based on the interannual analysis of the Enhanced Vegetation Index (EVI) for the 2005 drought, a result that was subsequently challenged (ATKINSON et al., 2011; SAMANTA et al., 2010). In contrast, Xu et al., (2011) observed a widespread decline in greening for the 2010 drought.

Similar to the drought events, the prevailing view of seasonality of vegetation in the Amazonian forests has recently been discussed. Several findings (BRANDO et al., 2010; GRAHAM et al., 2003; HUETE et al., 2006a; HUTYRA et al., 2007; MYNENI et al., 2007; SAMANTA et al., 2012a; WAGNER et al., 2013) support the view that photosynthetic activity increases initially during the dry season in response to an increase in incident photosynthetically active radiation (PAR). On the other hand, a recent study based on NASA's Moderate Resolution Imaging Spectroradiometer (MODIS) (MORTON et al., 2014) argued that seasonal changes are driven by artifacts of the sun-sensor geometry. To date, inter and intra-annual ecosystem dynamics of Amazonian forests remain unclear and debated (HUETE et al., 2006a; MORTON et al., 2014; MYNENI et al., 2007; SAMANTA et al., 2010, 2012b).

One potential reason for these conflicting results might be the range of measurement uncertainties in remote sensing data; a growing body of literature suggests that the

atmospheric correction process, including aerosol retrievals and cloud cover detection (SAMANTA et al., 2010, 2012b; HILKER et al., 2012), could be partially responsible for these contradicting evidences. While progress has been made addressing some of these challenges by using alternative datasets (HILKER et al., 2012b, 2014) remotely sensed images are often limited in their ability to detect changes in vegetation cover. The spectral sensibility and temporal resolution are also sources of uncertainties, as well as, factors that are not sensor-dependent as the differences between forests typologies and climatological variations across the area.

Conventional remote sensing approaches to monitor changes in the Amazon forest rely on vegetation indices to estimate “greenness” as a surrogate for photosynthetic activity. Arguably, most prominently, the Normalized Difference Vegetation Index (NDVI) (TUCKER, 1979) has been used for several decades to provide global measures of vegetation conditions. While this approach can provide simple estimates of the vegetation “greenness”, these estimates are empirical in nature and subject to a well-documented saturation effect in areas with high biomass and leaf area (CARLSON; RIPLEY, 1997), as the case for Amazonian forests. Similarly, the EVI (HUETE et al., 1994) was also designed to measure greenness and to reduce the saturation effect. However, recent studies have shown that EVI is also dependent on sun-viewing geometry (GALVÃO et al., 2011; KEMPENEERS et al., 2008; MOURA et al., 2012). This dependence of canopy level estimates on viewing and solar geometry (VERSTRAETE et al., 1996) limits our ability to compare between measurements taken from different directions or during different times of the day or year (LOS et al., 2005).

Complementary to passive remote sensing techniques, significant advances have been made measuring canopy vegetation structure from Light Detection and Ranging (LiDAR), a laser scanning technique. It allows direct measurements of the three-dimensional distribution of vegetation elements within the canopy from ground-based, airborne and spaceborne platforms. Such measurements have been extensively used to estimate vegetation density, leaf area, height and biomass, among others (COOPS et al., 2007; HILKER et al., 2012a; LEFSKY et al., 2002; POPESCU et al., 2011). While these techniques can potentially improve our knowledge on tropical forests and provide

accurate estimates of vegetation structure, their current availability is limited in space and time. As a result, our ability to evaluate inter-annual and seasonal dynamics of vegetation structure over large areas using LiDAR alone is not feasible.

As an alternative to conventional mono-angle observations, and as a potential tool for scaling between existing or upcoming LiDAR observations, multi-angular data, acquired simultaneously at the same location, provide a means to characterize the anisotropy of surface reflectance (LEBLANC et al., 2005). The anisotropy contains information on the structure of vegetated surfaces and shaded parts of the canopy (CHEN et al., 2003; GAO, 2003b). The combination of multiple view angles may provide new opportunities to mitigate these saturation effects, and allow better insights into seasonal and inter-annual changes of tropical forests. Biophysical changes in the canopy structure affect the directional scattering of light and these effects are observable from multi-angular observations (CHEN et al., 2005). This may help in the discrimination between forests with structural differences and specifically seasonal patterns. The theoretical basis for the influence of canopy structure on multi-angle reflectance has been already developed and well established in the literature (BICHERON, 1999; CHEN et al., 2003; GAO, 2003b; LEBLANC et al., 2005; MYNENI et al., 2002). As a result, multi-angular observations can help overcome the limitations faced by traditional remote sensing techniques and yield reliable estimates of canopy structure. MODIS observations are acquired at different sun-observer geometries depending on orbital overpass and time of the year, and could therefore potentially be combined to derive multi-angle observations. However, bi-directional reflectance is not easily obtained from traditional surface reflectance algorithms, even when data is acquired from multiple view angles. Pixel based algorithms often assume a Lambertian reflectance model, which reduces the anisotropy of the derived surface reflectance (LYAPUSTIN; MULDASHEV, 1999; WANG et al., 2010), thus decreasing the ability to detect directional scattering (HILKER et al., 2009).

New methods for processing MODIS data have been proposed. The Multi-Angle Implementation of Atmospheric Correction (MAIAC) uses an advanced radiative transfer model and does not make a Lambertian assumption. MAIAC can assist in the

generation of a new dataset that preserves the anisotropy of the surface (LYAPUSTIN; KNYAZIKHIN, 2001). MAIAC is a new generation cloud screening and atmospheric correction algorithm that uses an adaptive time series analysis and processing of groups of pixels to derive atmospheric aerosol concentration, cloud mask and surface reflectance without typical empirical assumptions (LYAPUSTIN et al., 2011, 2012b).

In this work, we take advantage of multi-angle derived MODIS data processed by MAIAC to derive anisotropy and study changes in canopy structure across the Amazon basin. We state the following hypotheses:

- Multiple overpasses of MODIS observations process with the MAIAC algorithm may be combined to provide anisotropy of the surface reflectance in spatially and temporally comprehensive manner;
- MODIS derived anisotropy can describe changes in canopy structure in space and time;
- Such derived estimates can help to improve our knowledge of inter-annual and seasonal variability in the Amazonian forests.

The objectives of this thesis were: 1) proposing a new model to derive anisotropy surface reflectance from multi-angle MODIS data to characterize the dynamics of canopy structure in mature Amazonian forests; 2) applying a spatial scaling approach, from airborne to spaceborne LiDAR, to validate MODIS-derived anisotropy and to model continuous coverage of canopy structure across tropical forests, and 3) using a time series approach of anisotropy in order to investigate seasonal and inter-annual variations, as well as, extreme events of droughts across the Amazon basin.

2 THEORETICAL BACKGROUND

2.1. Directional scattering in vegetated surfaces

Surface reflectance is a function of the geometry of data acquisition composed of the sun-sensor-target configuration (Figure 2.1). Differences in this configuration cause the so-called bidirectional reflectance (BRF) effects, which alter the amount of energy received by a sensor. As a result, bi-directional scattering can produce variations in the reflectance that are not necessarily associated with physical variations over the surface (RANSON et al., 1985). Consequently, the effects of surface BRF are important to consider when interpreting remotely sensed changes in vegetation and, particularly, seasonal cycles (ASNER et al., 1998).

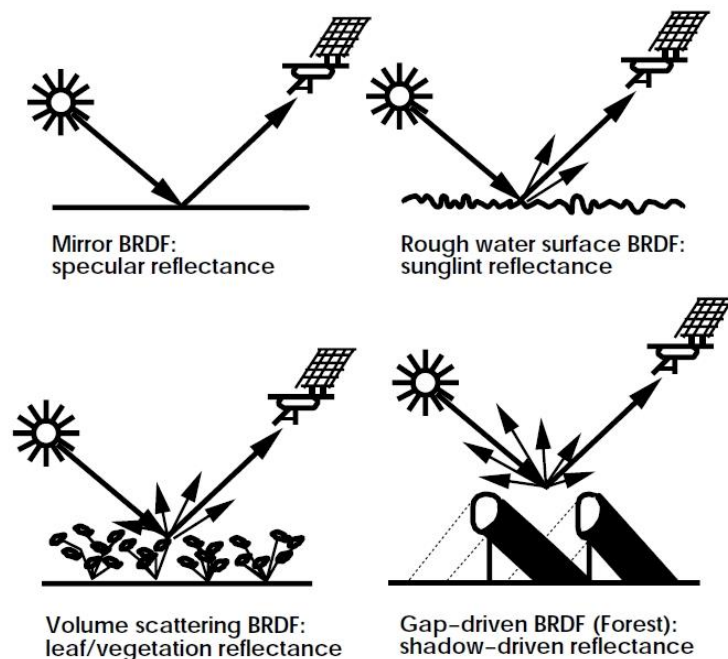


Figure 2.1. Illustration for the land surface reflectance anisotropy. Specular scattering, as sunlint are observed where forward scattering or soil elements are presented. Volumetric scattering, by finite scatterers (leaves or canopies) have anisotropic reflectance. Geometric scattering, given by shadow-casting of three dimensional elements, for example trees or brushland.

Source: Adapted from Strahler; Muller (1999).

Across vegetated surfaces, directional scattering is predominant in the near infrared (NIR) because the energy in this spectral interval is almost entirely reflected by the leaves and other canopy components. Nonetheless, directional scattering significantly affects also the visible reflectance. The BRDF effect on vegetation indices, such as NDVI and EVI, which are commonly used to describe vegetation properties, has been discussed intensively in the literature (GALVÃO et al., 2013; KEMPENEERS et al., 2008; MOURA et al., 2012). Bhandari et al., (2011) demonstrated that the view-illumination effects diminish the ability of vegetation indices to detect seasonal variations over vegetated surfaces. Galvão et al., (2011), using MODIS and Hyperion/Earth Observing-One (EO-1) data, showed that view-illumination geometry influence seasonal signals of EVI in the dry season over tropical forests in the Amazon basin. For instance, the EVI variability at nadir viewing was driven by solar illumination effects rather than changes in LAI. BRDF effects were also demonstrated by Sims et al., (2011) over forested regions (dense evergreen and deciduous forests) in the United States. The authors concluded that view angle effects were stronger on EVI than NDVI, which presented substantial variations across seasons and years. The increased sensitivity of EVI to bidirectional reflectance effects may be explained by the strong NIR band dependence or the influence of empirical weight factors such the L coefficient (GALVAO et al., 2011; HILKER et al., 2015a; MOURA et al., 2012). In case of a normalized difference index (e.g., NDVI), reflectance changes in forward and backscattering are less pronounced, particularly in dense vegetation (HU et al., 2003). Changes in one band are compensated by the relative changes in the other band during the rationing or normalization procedure (KAUFMANN et al., 2000).

Different methods have been proposed for BRDF correction (FRANCH et al., 2013; SCHAAF et al., 2002), thereby eliminating the variability derived from view angle effects. Brando et al., (2010) suggested the use of the MODIS nadir bidirectional reflectance distribution function (BRDF)-adjusted reflectance product to reduce view angle effects on EVI. However, standard correction approaches do typically not account for sun angle effects; an important consideration when observing vegetation seasonality

(BI et al., 2015; MORTON et al., 2014). Besides, other effects (i.e. atmospheric correction) can also have influence in the seasonal patterns.

While eliminating BRDF effects can help to reduce signal variations with respect to differences in acquisition angles, it is important to understand that these effects are a function of structural composition of the surface. For instance, the directional pattern of the scattering is largely controlled by the physical properties and geometrical arrangements of the elements that constitute the surface (WIDLÓWSKI et al., 2004). As a result, BRDF can contain useful information on vegetation structure. Rather than trying to correct for these effects, which essentially eliminates this structural information, a number of studies have tried to incorporate view-illumination effects in order to obtain information on structural changes in addition to greenness. View-illumination effects may be modeled in terms of the BRDF. BRDF is a wavelength dependent model, which considers directional scattering as a function of surface properties and the amount of energy present in a photon. Chen et al., 2003; Gao, 2003a; Rautiainen, 2005; Zhang et al., 2002, used BRDF models to characterize the anisotropy of the surface, retrieving useful information from that about the vegetation structure. The acquisition of measurements over a range of observation angles also allows the estimation of shaded components in the surface, which is dependent of the structural form of the surface, to derive the surface anisotropy (CHEN et al., 2005). The interaction between canopy structure and multi-angle reflectance is associated with canopy elements, expressed by the density (LI, X., STRAHLER, 1986), architecture, foliage orientation and shadow within the canopy (GOEL, 1988), as well as the roughness of the surface in sparse canopies (JACQUEMOUD et al., 1992), among others. Figure 2.2 demonstrates how differences in the geometry of data acquisition can affect the scattering of light and its detection by the sensor in vegetated surfaces.

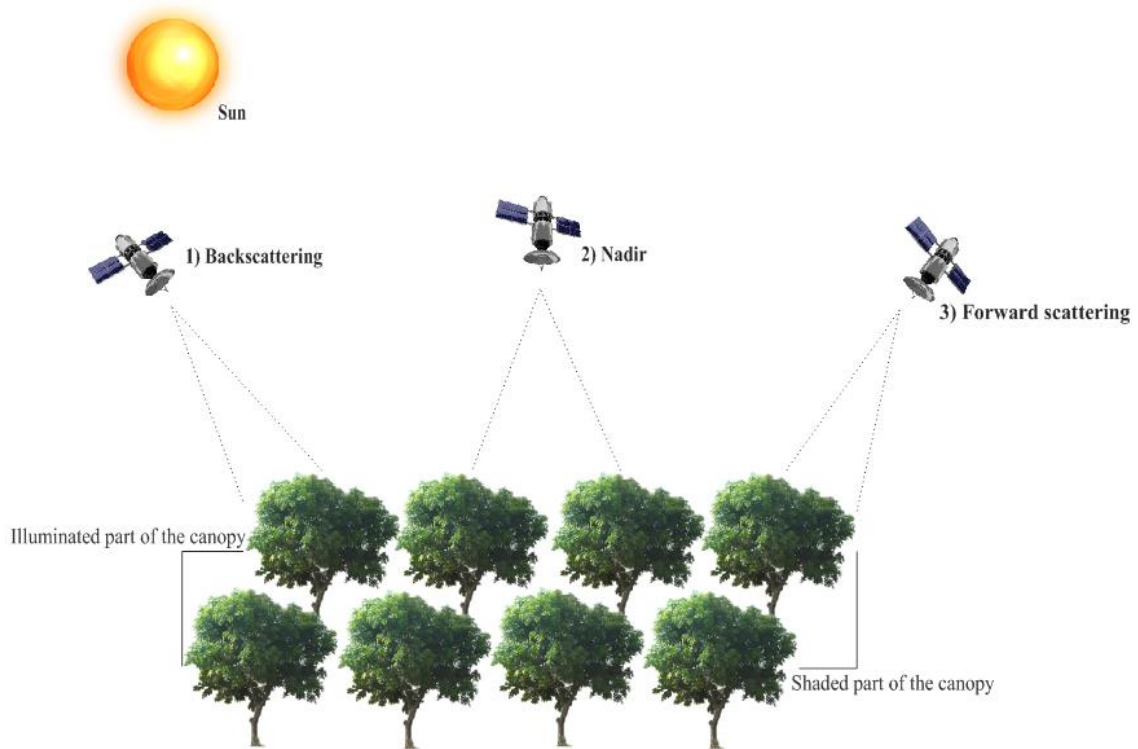


Figure 2.2. Diagram of different geometry acquisitions over vegetated surfaces. 1) backscattering: represents the configuration where the sensor direction is the same as the incident light (sun); 2) nadir: represents the direction pointing directly below a location, orthogonal to a horizontal flat surface; and 3) forward scattering: where the sensor and sun are in opposite direction.

The availability of multi-angular observations over the same target by the Multi-angle Imaging SpectroRadiometer (MISR) has provided new inputs for the characterization of the surface anisotropy. Several studies have shown that the scattering of light is deeply related to structural properties of the surface (CHEN et al., 2005; HAPKE et al., 1998; WIDLOWSKI et al., 2004). In addition to along-track MISR observations, successive cross-track MODIS over-passes provide potentially the necessary multi-angular data to characterize the anisotropy of vegetated surfaces. The use of multi-angle data has indicated also improvements with respect to simulations in ecosystem models (KNORR et al., 2004). However, despite the potentiality of multi-angle data, the complexity of using such approach is still a challenge (WIDLOWSKI et al., 2004).

2.2. Moderate Resolution Imaging Spectroradiometer (MODIS)

The advent of the Earth Observing System program (EOS, KING & GREENSTONE, 1999) has provided a high quality Earth observation collection, allowing important advances in many fields of earth system science. Since its launch in 2000, NASA's MODIS has been the workhorse of Amazon remote sensing (HUETE et al., 2002). The MODIS sensor is flown on two spacecraft. The Terra satellite, launched in 2000, is on an AM overpass, whereas the Aqua platform provides complementary observations in the afternoon. With their wide swath of 2300 km, the MODIS instruments have been providing daily global data of planetary atmospheric aerosol for one and a half decade, allowing scientists to evaluate impacts of population growth as well as climate change on global vegetation (KING & GREENSTONE, 1999). Studies of the Amazonian ecosystem have heavily relied on MODIS daily surface reflectance or 8- and 16-day composite products to analyze seasonal changes as well as severe droughts (ANDERSON, 2012). Despite its undisputed success, MODIS data processing is not free of weaknesses and several issues have been identified, particularly for the frequently cloud covered tropical regions (SAMANTA et al., 2012b). The conventional correction algorithm for atmospheric scattering effects is pixel-based and relies on observations acquired over a single orbit. As a result, only one measurement is available for every pixel characterized by two main unknown parameters: aerosol optical thickness (AOT) and surface reflectance (SR). This lack of information constitutes a fundamental problem of the atmospheric correction process that cannot be resolved without a priori information. As a result, assumptions have to be made. For instance, atmospheric correction is based on the MODIS Dark Target algorithm (KAUFMAN et al., 1997; LEVY et al., 2007; REMER et al., 2005), currently complemented with the Deep Blue method (HSU et al., 2004). Further assumptions include a Lambertian property of surface and the use of ancillary data obtained from other sources and models. While these assumptions may hold over temperate latitudes, previous results (SAMANTA et al., 2012b) have suggested that they may compromise subsequent atmospheric correction, thereby affecting the quality of the reflectance product.

2.3. Multi-Angle Implementation of Atmospheric Correction (MAIAC)

New methods for processing MODIS data, such as the MAIAC, can help overcome some of these limitations by using an advanced radiative transfer model that reduces the number of assumptions made (LYAPUSTIN & KNYAZIKHIN, 2001). Based on a sliding window approach, MAIAC simultaneously processes between 5 (at the poles) and 16 (at the equator) observations gridded to 1 km resolution, exploiting the advantages of time series processing for cloud masking and aerosol-surface retrievals (LYAPUSTIN et al., 2011). For instance, time series processing allows to simultaneously retrieval of atmospheric optical thickness (AOT) and surface bi-directional reflectance factor (BRF). The multi-day data provide different view angles, which are required for the surface BRF retrieval. The algorithm is based on the supposition that the surface reflectance changes little during accumulation period. It assumes that the AOT changes little at short distances (~25 km), because aerosols have a mesoscale range of global variability of 50 to 60 km (LYAPUSTIN et al., 2008).

MAIAC includes water vapor retrievals, cloud masking, aerosol retrievals and atmospheric correction. The separate processing blocks are interdependent because they share the data through the common algorithm memory and may update each other's output. A brief description of MAIAC, based on the Algorithm Theoretical Basis Document (ATBD) (LYAPUSTIN et al., 2008), is illustrated in the diagram of Figure 2.3.

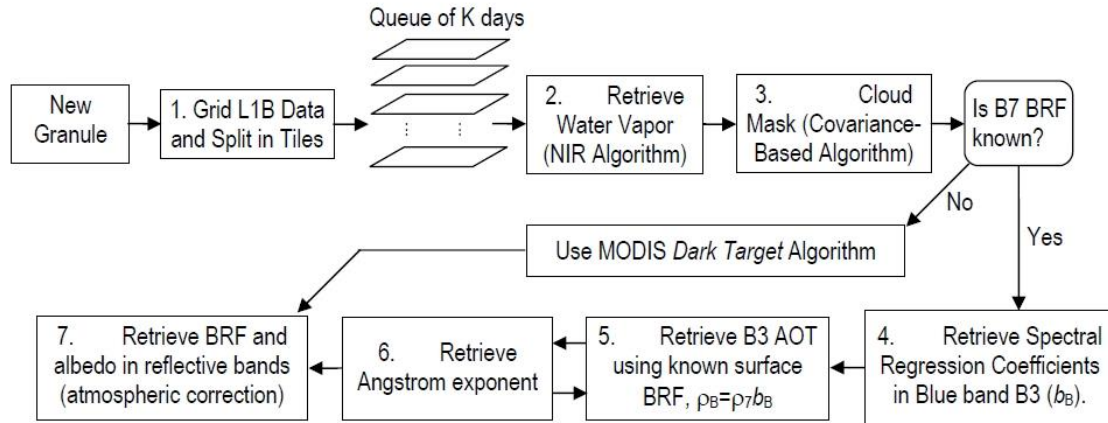


Figure 2.3. Block-diagram of MAIAC algorithm.

Source: Adapted from Lyapustin et al. (2008).

- 1) The process starts by gridding the received MODIS calibrated and geo-located (L1B) data (WOLFE et al., 2002a), splitting them into tiles, and placing the new data in the processing queue with the previous data. In order to limit variation of the footprint with changing view zenith angle (VZA), the resolution is coarsened (by a factor of 2). For example, the grid cell size is 1 km for MODIS 500-m channels B1-B7. MAIAC then uses the MODIS land gridding algorithm (WOLFE et al., 2002b) with minor modifications to better preserve the anisotropy of signal in the gridded data when the measured reflectance is high, for example, over snow, thick clouds or water with sun glint effects.
- 2) To retrieve the water vapor, MAIAC uses a modified version of (GAO, 2003a) algorithm, based on the last MODIS tile in the NIR channels located close to the water vapor absorption at 0.94 μm . The water vapor retrievals are implemented internally to exclude dependence on other MODIS processing streams and unnecessary data transfers.
- 3) The cloud mask (CM) algorithm takes advantage of the time series measurements and use covariance analysis to identify cloud-free blocks. The model assumes that the surface spatial pattern is stable and reproducible in the short-term frame in cloud-free conditions, whereas clouds randomly disturb this pattern. A

reference of clear-skies images are build, which are then used in the pixel level cloud masking as an additional reference. Internally, the MAIAC CM algorithm also has a dynamic land-water-snow classification used to guide the processing of the surface image.

4) The algorithm simultaneously retrieves AOT and spectral regression coefficient (b_{ij}) for the blue band. If the surface reflectance of B7 is not known, MAIAC uses a simplified version of the MODIS Dark Target algorithm.

5) In this step, retrievals of AOT are processed at high 1 km resolution from the last tile, once the surface boundary condition is known. The algorithm uses previous information from spectral regression coefficient for the blue band at a grid resolution.

Surface BRF and albedo are calculated for the reflective MODIS bands for the k-day queue.

MAIAC offers substantial improvement over conventional algorithms by mitigating atmospheric interference and advancing the accuracy of surface reflectance over tropical vegetation by factor of 3-10 (HILKER et al., 2012b). Previous analysis has linked 80% of this improvement to a more accurate and less conservative, but more rigorous cloud mask, which increases the number of clear-sky observations by a factor of 2 to 5 (HILKER et al., 2012b).

2.4. Light Detection and Ranging (LiDAR)

Arguably, the most direct and accurate remote sensing measurements of vegetation structure, cover and density are possible using Light Detection and Ranging (LiDAR). LiDAR is an active remote sensing technique that facilitates direct measurements of the three-dimensional distribution of vegetation canopy components as well as sub-canopy, thereby providing high spatial resolution topographic elevation, and accurate estimates of vegetation height, cover density, and other parameters of canopy structure (LEFSKY et al., 2002). The LiDAR fundamentals are based on the emission of a pulse of light, in which the reflection of that pulse is detected and the precise time of return is recorded. Using the constant speed of light, the time shifts can be then converted into a slant range

distance. With position and orientation of the sensor known, the coordinates (x , y , and z) of the reflective surface can be calculated (Figure 2.4).

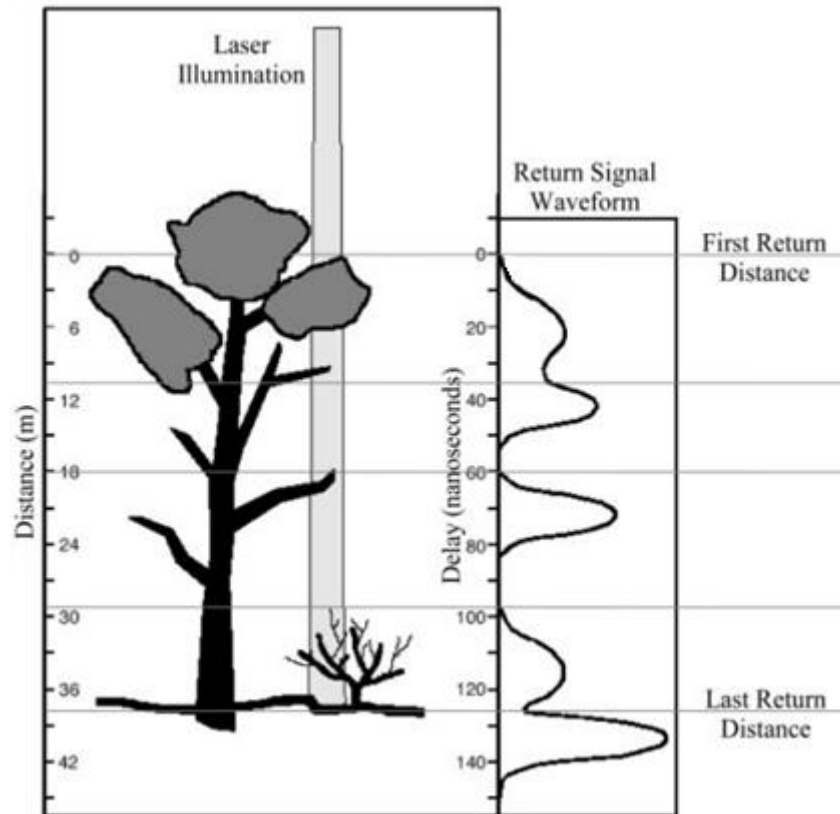


Figure 2.4. Illustration of the conceptual basis of LiDAR remote sensing. At the left, the intersection of the laser illumination area, or footprint, with a portion of a simplified tree crown, is represented. At the right, the hypothetical return signal (the lidar waveform) recorded by the sensor over the area is shown. By subtracting the range of the ground (last return) from the first detectable canopy return (first return), the canopy height is determined.

Source: Adapted from Lefsky et al., (2002)

Each laser pulse emitted from a LiDAR instrument is either reflected from the terrain or from objects on the terrain, such as vegetation or buildings. As a result, they can be distinguished between the first and last pulse returns (LIM et al., 2003a). While the first pulse hits are reflected from the highest surface (e.g. tree canopies), the last hit returns are reflected from the lowest points in the landscape, most often the terrain surface,

except in situations of dense understorey or overstorey vegetation cover. The distance between the LiDAR source and the point of reflectance is determined by the time the light beam requires to travel from the emitting sensor to the surface and back to the sensor. LiDAR measurement error for individual tree heights (of a given species) is typically less than 1.0 m (PERSSON et al., 2002), and less than 0.5 m for plot-based estimates of maximum and mean stand height with full canopy closure (MAGNUSSON et al., 1999; MAGNUSSEN; BOUDEWYN, 2011; MAGNUSSON et al., NÆSSET, 2002). Furthermore, LiDAR estimates of tree and stand height have been shown to be more consistent than field based measurements (NÆSSET, 2002b). LiDAR observations can be distinguished between full waveform and discrete return recording. A full waveform system records the intensity of a reflected light pulse in its entirety, whereas discrete return systems result in binary recordings based on thresholds of light intensity returned.

Most vegetation related LiDAR applications rely on airborne platforms for data acquisition, with measurements acquired at altitudes between 500 and 3000 m (HILKER et al., 2010). While airborne systems are able to cover moderately large vegetation stands to measure vegetation structure (COOPS et al., 2007; NÆSSET, 1997b; WULDER et al., 2012), their availability over the Amazon basin, is limited. Recently, some improvements of airborne LiDAR coverage over the Amazon basin have been made by the Sustainable Landscapes Brazil project, a partnership between the United States Agency for International Development (USAID), the United States Forest Service (USDA) and the Empresa Brasileira de Pesquisa Agropecuária (EMBRAPA).

Alternatively to airborne LiDAR, a few studies have also explored the potential of using spaceborne LiDAR observations for estimating tree heights and mapping biomass (POPESCU et al., 2011; SAATCHI et al., 2011). Most notably, the GLAS (Geosciences Laser Altimeter System) instrument on NASA's ICESat (Ice, Cloud, and land Elevation) satellite, has collected full waveform recordings of spatially discrete samples from 2002 to 2008 (HEALEY et al., 2012a). GLAS measurements ("shots") are based upon time variation in the intensities of returned laser pulses, and resolve elliptical areas approximately 65 meters in diameter (HEALEY et al., 2012b). While not primarily

designed for estimating vegetation heights, GLAS measurements have been shown to be strongly correlated with biomass (SAATCHI et al., 2011), and may be suitable for vegetation monitoring. Across the Amazon basin, GLAS footprints form a dense mesh with footprints spaced at 170 m intervals along the surface, temporal coverage of observations but data availability is still limited.

3 A NEW APPROACH TO CHARACTERIZE ANISOTROPY SURFACE REFLECTANCE FROM MULTI-ANGLE MODIS/MAIAC DATA

Accurate estimates of vegetation structure and its variation in space and time are essential for scientific understanding of the ecological and ecosystem processes in the Amazon (ANDERSON, 2010; ARAGÃO et al., 2009). To date, these observations are limited to spatially discrete field plots or ground surveys. Scaling such measurements across the basin has been extremely challenging. Remote sensing is the main alternative to observe vegetation dynamics in the Amazon basin. As tropical forests are primarily characterized of structurally complex canopies, its reflectance signal tends to be anisotropic. The anisotropy brings information of the structural features of the surface (HAPKE et al., 1998), that is affected by the reflectance scattering. Thus, surface anisotropy may provide more useful information of the structure of the canopies than that provided only by surface reflectance, mostly based on mono angle observations.

Due to the anisotropic behavior of scattering in vegetated surface, there has been an upsurge interest in the potential of off-nadir sensing to provide information regarding canopy structure (BARNESLEY et al., 2004b; DISNEY et al., 2006). For instance, multi-angle remote sensing has the potential to derive information on vegetation canopy structure. However, multi-angle reflectance is not easily obtained and there is still some challenges regarding the processing to retrieve bi-directional reflectance, including issues associated with atmospheric aerosol loadings and cloud screening. Conventional aerosol retrieval algorithms assume a Lambertian surface model, which reduces the anisotropy of the derived reflectance and introduces an error that depends on the aerosol amount and the view-observer geometry (LYAPUSTIN, 1999; WANG et al., 2010).

Multi-angular data, simultaneously acquired at the same location, provide a means to characterize the anisotropy of surface reflectance (LEBLANC et al., 2005), which has been shown to contain information on the structure of vegetated surfaces and shaded parts of the canopy (CHEN et al., 2003; GAO, 2003b). Multi-angular data also allow characterization of the bi-directional reflectance distribution of surface reflectance

(CHEN; LEBLANC, 1997; GAO, 2003b), which facilitates modeling of canopy reflectance independently of the sun-observer geometry. As a result, it can help overcome the limitations faced by traditional mono-angle remote sensing techniques and yield more robust estimates of canopy structure.

MODIS observations are acquired at different sun-observer geometries depending on orbital overpass and time of the year. Using MAIAC algorithm to derive BRDF reflectance, combinations of several MODIS observations may be used to describe the anisotropy of surface reflectance. The novelty of the approach is take an advantage of the use of multi-angle MODIS data processed by MAIAC to describe structural characteristics of the canopies in the Amazonian forests. The MAIAC datasets allow to re-assess the status and dynamics of Amazon vegetation from multi-angle remote sensing, providing a more comprehensive understanding of seasonal and spatial dynamics of ecosystem processes. In this Chapter, I describe the steps to derive multi-angle information from MODIS images and the procedures to obtain anisotropy images for the Amazon basin.

3.1. BRDF retrievals from MODIS/MAIAC

In order to quantify multi-angle scattering, MAIAC data were obtained from 12 MODIS tiles (h10v08 to h13v10, spanning 10°N to 20°S in latitude and 80° W to 42°W in longitude) from Terra and Aqua satellites between 2000 and 2012. MAIAC is based on MODIS Level 1B (calibrated and geometrically corrected) observations, which remove major sensor calibration degradation effects present in earlier collections (LYAPUSTIN et al., 2014). MAIAC grids MODIS L1B data to a 1 km resolution, and accumulates measurements of the same surface area from different orbits (view geometries) for up to 16 days using a moving window approach. These data are used to derive spectral regression coefficients relating surface reflectance in the blue (0.466 μm) and shortwave infrared (2.13 μm) for aerosol retrievals, and to obtain parameters of surface BRDF (LYAPUSTIN et al., 2011, 2012a). Assuming that vegetation is relatively stable during this period, the surface directional scattering can be characterized using the Ross-Thick Li-Sparse (RTLS) BRDF model (ROUJEAN et al., 1992). During periods of rapid

surface change (e.g., green-up or senescence), MAIAC follows the approach of the MODIS BRDF/albedo algorithm (MOD43 product; SCHAAF et al., 2002) to scale the BRDF model with the latest measurement to adjust the magnitude of reflectance while assuming that the shape of BRDF does not change significantly. This approach preserves spectral contrasts of actual surface characteristics.

To first order, reflectance anisotropy can be characterized as the difference of reflectance hotspot (Solar Zenith Angle (SZA) = 45°, VZA = 35°, Relative Azimuth Angle (RAA) = 180°) and darkspot (SZA = 45°, VZA = 35°, RAA = 0°), derived from modeling the BRDF. Under the assumption that the vegetation surface remains constant over a period (16 days), its directional scattering can be characterized in terms of a BRDF model. Different BRDF models exist. One of the most commonly used is the Ross-Thick and Li-Sparse kernel functions (ROUJEAN et al., 1992). In our study, the Ross-Thick and Li-Sparse kernel functions were used based on the radiative transfer theory of (ROSS, 1981) and the geometric-optical model of (LI, X., STRAHLER, 1986):

$$\rho(\theta_v, \theta_s, \Delta\phi) = k_i + k_g K_L(\theta_v, \theta_s, \Delta\phi, \frac{h}{b}, \frac{b}{r}) + k_v K_R(\theta_v, \theta_s, \Delta\phi) \quad (3.1)$$

where

k_i	isotropic scattering component
k_g	geometric scattering component
K_L	Li-Sparse kernel
k_v	volumetric scattering component
K_R	Ross-Thick kernel
θ_v	view zenith angle (VZA)
θ_s	solar zenith angle (SZA)
$\Delta\phi$	relative azimuth angle (RAA)
$\frac{h}{b}$	crown relative height =1 (JUSTICE et al., 1998; WANNER et al., 1995)
$\frac{b}{r}$	crown relative shape =2 (JUSTICE et al., 1998; WANNER et al., 1995)

k_i , k_g and k_v are the empirical components (kernel weights) and are derived from mathematical inversion of the linear model using the MODIS reflectance observations. Once k_i , k_g and k_v are acquired, ρ can be obtained for any view observer geometry by setting $\theta_v, \theta_s, \Delta\phi$.

One advantage of using the RTLS model rather than reflectance directly is the possibility to maintain constant sun-observer geometry and extrapolate measurements to the principal plane to describe backscatter and forward scatter directions. In this study, we selected a view zenith angle (VZA) of 35° rather than the absolute hotspot location at $VZA = 45^\circ$ in order to keep the modeled reflectance closer to the actual range of angles observed by MODIS, thereby minimizing potential errors resulting from extrapolation of the BRDF. For land vegetated surfaces, directional scattering dominates in the NIR region due to the high absorption of visible light. Rather than obtaining anisotropy of the NIR band alone, we calculated forward and backscatter data for blue, red and NIR reflectance and then obtained the Enhanced Vegetation Index (three-band version EVI) for both directions, calculated as:

$$EVI(\theta_v, \theta_s, \Delta\phi) = G \times \frac{\rho_{nir}(\theta_v, \theta_s, \Delta\phi) - \rho_{red}(\theta_v, \theta_s, \Delta\phi)}{\rho_{nir}(\theta_v, \theta_s, \Delta\phi) + C_1 \times \rho_{red}(\theta_v, \theta_s, \Delta\phi) - C_2 \times \rho_{blue}(\theta_v, \theta_s, \Delta\phi) + L} \quad (3.2)$$

where $\rho(\theta_v, \theta_s, \Delta\phi)$ is the atmospherically corrected surface reflectance for a give sun sensor geometry; L is the canopy background adjustment (1.0); C_1 (6.0) and C_2 (7.5) are the coefficients of the aerosol resistance term; and G (2.5) is a scaling factor (HUETE et al., 1994).

The objective of using EVI rather than surface reflectance of a given band was to minimize the effect of non-photosynthetically active elements while optimizing the sensitivity to green canopy structure. However, it can be shown that differences between forward and backward scatter EVI is largely the result of differences in scattering in the NIR region (GALVAO et al., 2011; MOURA et al., 2012).

The left column in Figure 3.1 shows an example of a BRDF surface fitted to retrieve forward and backscatter for red reflectance (a) and NIR reflectance (c). We also illustrated a BRDF surface calculated for EVI (e) to demonstrate the anisotropy of this index. The RTLS surfaces are shown for a 1x1 km area of Amazon forest (65°0'0" W, 5°0'0" S) using all observations acquired between January 1 and 14, 2006. The polar coordinates represent the view zenith and azimuth angles, whereas the z-axis shows the corresponding reflectance (ρ) in the red and NIR bands, and EVI, respectively. The black dots represent the MODIS observations that were used to parameterize the BRDF surface. The red and blue dots show the modeled forward and backscatter reflectance (Figure 3.1, left column) with a fixed sun-observer geometry ($\text{SZA} = 45^\circ$, $\text{VZA} = 35^\circ$, $\text{RAA} = 180^\circ$ in the backscatter direction and $\text{SZA} = 45^\circ$, $\text{VZA} = 35^\circ$, $\text{RAA} = 0^\circ$ in the forward scatter direction). We fitted one such surface for each pixel and 16-day period to derive bi-weekly anisotropy across the Amazon basin.

Figures 3.1b, 3.1d and 3.1f show temporal variations in anisotropy (for red, NIR and EVI, respectively) for different sun-observer geometries to verify the robustness of the method applied. The time series shows a spatial average of MODIS tile h12v09 (south-central Amazon) as an example. We varied the solar zenith angle between 45° (which is the default angle for BRDF normalization in MAIAC) and 25° degrees (which is more commonly found in tropical latitudes).

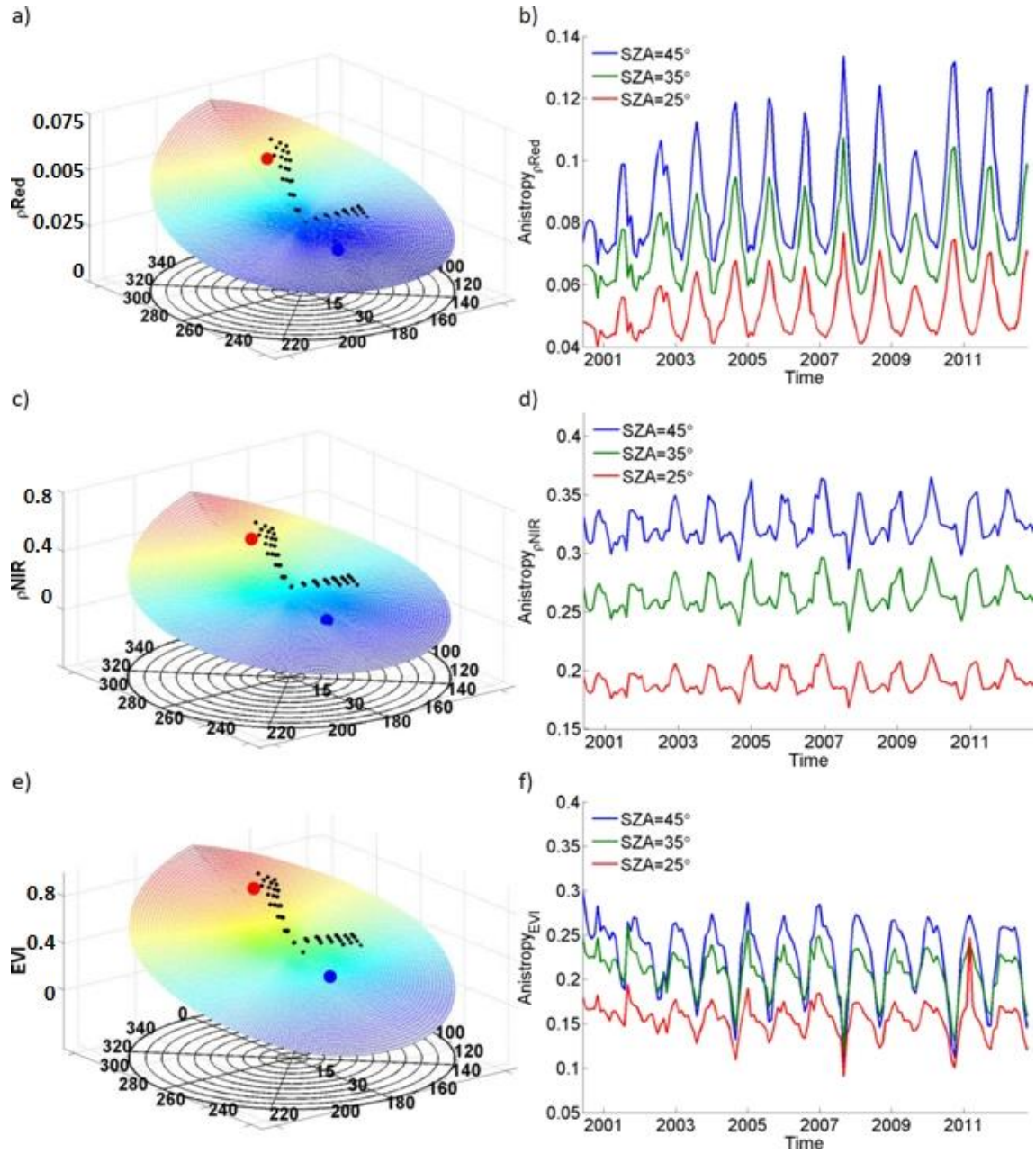


Figure 3.1. Modeled BRDF surface for a 1x1 km area of Amazon forest (65°0'0" W, 5°0'0" S) for red reflectance (a), NIR reflectance (c) and EVI (e). The black dots represent the actual MODIS observations accumulated over a 14-day period. The blue dot represents the modeled forward scatter direction (darkspot), while the red dot represents the modeled backscatter direction (hotspot). Figures b, d and f show a time series of anisotropy (red, NIR and EVI, respectively) using the mean time series of MODIS tile h12v09. Sun Zenith Angles (SZA) varied between 45°

and 25° degrees to investigate the sensitivity with respect to the sun-sensor configuration.

Figure 3.1 illustrates strong seasonal variations for red and NIR reflectance (variations in the blue band are not shown), and resulting EVI, irrespective of the modeled SZA. While reflectance and EVI anisotropy increased with increasing SZA, the seasonal difference is still apparent in all the profiles. The seasonal robustness with respect to a given SZA may be explained by the fact that the region around hotspot and darkspot area is relatively smooth (Figures 3.1a, 3.1c and 3.1e), making estimates of seasonal anisotropy relatively insensitive to the particular sun-sensor configuration selected, as long as this configuration remains constant. While the range of view angles acquired from MODIS is relatively small (Figure 3.1), as the instrument was not specifically designed for multi-angle acquisitions, anisotropy still provided an effective means to characterize vegetation structure across the Amazon forest. Changes in the sun-sensor configuration over the year do not always allow to model forward and backscattering observations within the sampling range of the MODIS instruments. However, the analysis presented in Figure 3.1 has demonstrated a relative robustness with respect to the selected sun-sensor configuration.

The spectral error of MAIAC surface reflectance may be evaluated as the standard error between observed surface reflectance (BRF) and BRDF model prediction: 1) over a time using an area of 50 x 50 km to obtain sufficient statistics given high cloud cover in Amazonia; and 2) in space (pixel by pixel) for the example of two 14 day periods, in June and October. Figures 3.2 and 3.3 provide a quantitative analysis of the standard error (σ) between observed surface reflectance and BRDF model prediction. Figure 3.2 shows the behavior of the standard deviation over a time, using an area of 50 x 50 km area as an example (65°0'0" W, 5°0'0" S). The mean standard error were 0.005 and 0.019 for the red and NIR reflectance, respectively, which is about 10-15% of the seasonal changes illustrated in Figures 3.1a and 3.1b. Slight seasonal variability in σ was found likely because of increased cloud cover during the wet season. Figure 3.3 illustrates the spatial variability of the standard deviation in June (Figure 3.3a) and October (Figure 3.3b). For reasons of brevity, only the variability in EVI is presented.

Similar to Figure 3.2, the standard deviation between observed EVI and model prediction presented in Figure 3.3 was on average about 5-10 % of the observed seasonal changes (compare Figure 3.1).

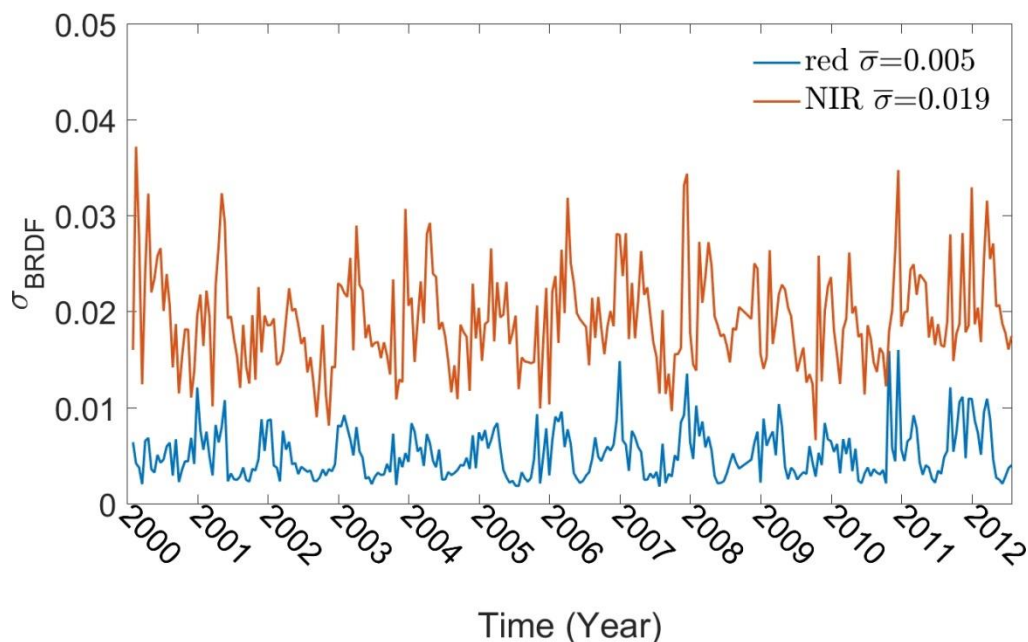


Figure 3.2. Temporal variability of the standard deviation (σ_{BRDF}) between observed and modeled MAIAC reflectance (red and NIR). The graph represents an area of 100 x 100 km to obtain sufficient statistics given high cloud cover in the Amazon ($65^{\circ}0'0''$ W, $5^{\circ}0'0''$ S).

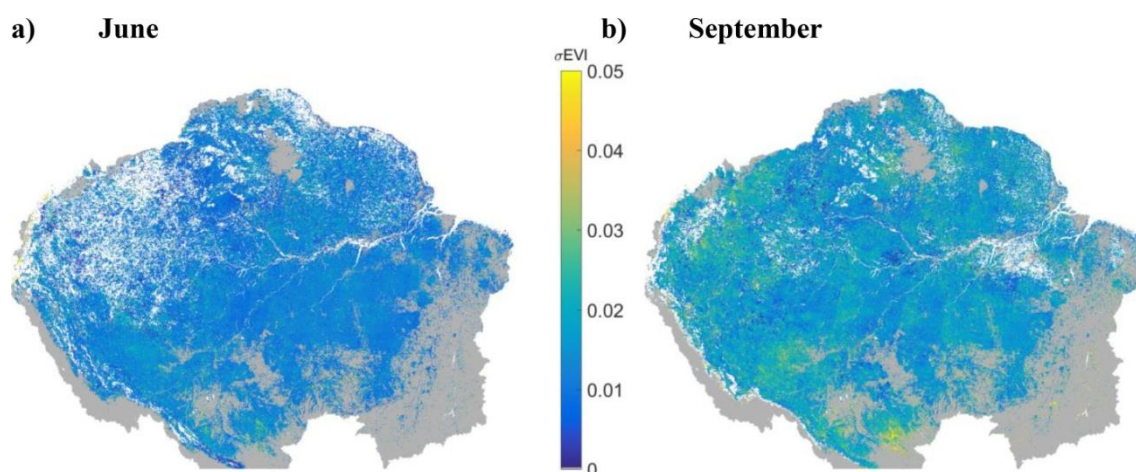


Figure 3.3. Spatial variability of the standard deviation between observed and modeled MAIAC EVI in (a) June and (b) September. Data were averaged over a 30-day

period to obtain sufficient statistics given high cloud cover in the Amazon. The Amazon delimitation used in this study follows the definition proposed by Eva et al., 2005.

The standard deviation between observed and modeled MAIAC reflectance (Figures 3.2 and 3.3) was about 10% of the observed variation in anisotropy (Figure 3.1), confirming the ability of our approach to detect seasonal and inter-annual changes. The results were further within the range of the RMSE reported in next results (see chapter 5, Figure 5.2), thereby confirming the significance of the relationship to canopy structure. The approach should account for error sources from undetected clouds to gridding uncertainties. It should further account for limitations of the RTLS model to describe the BRDF shape and anisotropy of the MAIAC data.

The BRDF model selected in this study allowed us to derive seasonal anisotropy independent of the sun-observer geometry, which is an important consideration for separating vegetation seasonality from artifacts due to seasonal changes in the sun/sensor configuration (MORTON et al., 2014). While it is acknowledged that vegetation may change over a 14 day period, as used in our BRDF approach, this technique should still allow us to observe most seasonality of vegetation and has proven useful in other composite products (HUETE et al., 2002; SCHAAF et al., 2002). Data scarcity may prevent frequent updates of BRDF shapes, which in some cases limit the ability to determine anisotropy and may lead to misinterpretation of changes in canopy structure. However, analysis of observation frequency across the Amazon basin (HILKER et al., 2015b) has shown that MAIAC provides on average between 10 and 60 observations in any given month from Terra and Aqua, respectively, which should allow stable BRDF inversions for most pixels. Other methods to derive multidirectional reflectance (FRANCH et al., 2013; SCHAAF et al., 2002) have been published. Their usefulness to derive MODIS anisotropy will have to be addressed separately.

4 VALIDATION OF VEGETATION STRUCTURE DERIVED FROM ANISOTROPY USING DIFFERENT DATASETS

4.1. Introduction

Terrestrial vegetation plays a significant role in the re-distribution of moisture and heat in the surface boundary layer, as well as in the energy balance of the planet (BASTIAANSSEN et al., 1998). Land atmosphere interactions are driven by the three-dimensional structure of vegetated land cover, including surface roughness, leaf area and canopy volume (VOURLITIS et al., 2015). Canopy roughness, defined as vertical irregularities in the height of the canopy (CHAPIN et al., 2011), plays a key role in earth system modeling. For instance, evapotranspiration is controlled much more by canopy roughness and, therefore, by aerodynamic conductance, than by canopy leaf area or maximum stomatal conductance (CHAPIN et al., 2011).

At stand level scales, significant advances have been made measuring canopy vegetation structure from Light Detection and Ranging (LiDAR). LiDAR allows direct measurements of the three-dimensional distribution of vertical vegetation elements from ground-based (STRAHLER, 2009a), airborne (WULDER et al., 2012) and orbital platforms (SUN et al., 2008). To date, most vegetation related LiDAR applications rely on airborne platforms for data acquisition, with measurements acquired at altitudes between 500 and 3000 m (HILKER et al., 2010).

The Geoscience Laser Altimeter System (GLAS), onboard the Ice, Cloud, and land Elevation Satellite (ICESat), has provided additional capability to map vegetation characteristics from the space (ZWALLY et al., 2002). GLAS is a large-footprint, waveform-recording LiDAR that measures the timing and power of the 1064 nm laser energy returned from illuminated surfaces (SCHUTZ et al., 2005). While not configured for vegetation characterization, the GLAS instrument allows quantification of the vertical distribution of plant components and the underlying ground within each footprint in vegetated terrain (HARDING, 2005; YU et al.; 2015). GLAS has been

successfully used to discriminate forest structure across various biome types (BOUDREAU et al., 2008; GONÇALVES, 2016; LEFSKY et al., 2005; PANG et al., 2008).

Clearly, LiDAR can provide valuable insights into the distribution of canopies, structural elements and vegetation types. However, its availability is currently limited in both space and time. As a result, our ability to evaluate seasonal, degradation levels and spatial variation in the roughness of vegetated canopies using LiDAR alone is limited. On the other hand, optical remote sensing instruments, such as those available from conventional satellite observations acquired at single view angles, are not designed to provide information on the vertical organization of forest canopies. These data provide general information on vegetation “greenness” (CARLSON & RIPLEY, 1997), especially when using vegetation indices (VI’s). Although VIs have been employed as proxies for greenness and vegetation structure, including the roughness lengths for turbulent transfer, field estimates of vegetation structure attributes are often only moderately correlated with VIs and their derivatives (GLENN et al., 2008).

As an alternative to mono-angle observations, the combination of multiple view angles may provide new opportunities for modeling the structure of vegetated land surfaces, which in turn is a function of leaf area distribution and canopy roughness (BREUNIG et al., 2015; SHAW; PEREIRA, 1982). With the advance of multi-angular sensors such as the Multi-angle Imaging SpectroRadiometer (MISR) (DINER et al., 1998), progress has been made in describing the dependence of reflectance on observation angles (BARNESLEY et al., 2004a; DINER et al., 1998). Changes in canopy structure are driven primarily by tree crown size, shape, density and spatial distribution of leaves, all of which affect the directional scattering of light observable from multi-angular remote sensing (CHEN et al., 2005). Data acquired from multiple view angles further decrease the dispersion and saturation in geometrically complex canopies (ZHANG et al., 2002). Therefore, they are better suited to describe the three-dimensional structure of dense vegetation (CHEN; LEBLANC, 1997; STRAHLER; JUPP, 1990). Multi-angular scattering of surface reflectance (anisotropy) has been linked to optical properties and geometric structure of the target (WIDLowski et al., 2004, 2005b), including canopy

roughness (STRAHLER, 2009a), leaf angle distribution (ROUJEAN, 2002), leaf area index (LAI) (WALTHALL, 1997) and foliage clumping (CHEN; MENGES; LEBLANC, 2005; CHOPPING et al., 2011).

Recent progress using the Multi-Angle Implementation of Atmospheric Correction Algorithm (MAIAC) has allowed the acquisition of multi-angle reflectance at high observation frequencies by combining satellite imagery obtained from NASA's Moderate Resolution Imaging Spectroradiometer (MODIS) Terra and Aqua platforms during a few overpasses. MAIAC is a cloud screening and atmospheric correction algorithm that uses an adaptive time series analysis and processing of groups of pixels to derive atmospheric aerosol concentration and surface reflectance without empirical assumptions of the Lambertian reflection of light. A detailed description of the algorithm can be found in Chapter 2 and in LYAPUSTIN et al., 2011, 2012a.

MODIS observations processed with MAIAC could potentially allow periodic and spatially contiguous estimates of vegetation structure parameters from multi-angle reflectance accumulated over a short period of time when the surface properties do not change. Such data, if correlated with more direct measurements of canopy structure by other instruments, such as LiDAR, could allow us to extrapolate canopy roughness estimates in space and time filling key data gaps for improving our understand of ecosystem structure and functioning. In addition to orbital and airborne laser instruments, previous studies have shown the applicability of scatterometers to obtain vegetation structure over dense forests. For instance, the SeaWinds microwave radar, onboard NASA's QuikSCAT satellite, was primarily designed to measure near-surface wind speed and direction over the oceans. However, due to its high sensitivity to water content that drives canopy dielectric properties, it has been also used to study canopy structure (FROLKING et al., 2011; SAATCHI et al., 2013).

In this Chapter, we used different estimates of canopy roughness obtained from 1) airborne laser scanning (ALS), 2) spaceborne LiDAR GLAS, and 3) the spaceborne SeaWinds scatterometer, to evaluate the potential of multi-angular MODIS data for modeling vegetation roughness from directional scattering of visible and NIR

reflectance. We implemented a spatial scaling approach, from airborne to orbital levels of data acquisition, to model continuous coverage of roughness across tropical forests of the Xingu basin area in Brazilian Amazon. Therefore, our objective was to test whether multi-angle MODIS reflectance can be used as a proxy for canopy roughness over Amazonian tropical forests, including different forest types such as Dense and Open ombrophilous Forests, and Semi-Deciduous Forest.

4.2. Material and Methods

4.2.1. Study area

The study area is located in the southeast part of the Amazon, including the Xingu basin and adjacent areas (Figure 4.1). Figure 4.1 also shows the GLAS transects for the study area (SCHUTZ et al., 2005) as well as the ALS and the field data plots. The study area presents a south-north gradient with respect to climate. Following the Köppen classification, the southern portion of the study area is dominated by tropical wet and dry climate (Aw), while the north portion is characterized by tropical monsoon climate (Am). Length and duration of the dry season, defined as months with rainfall less than 100 mm or less than one third of precipitation range (ASNER; ALENCAR, 2010; MYNENI et al., 2007), also varies across the study area. In the southern parts, the dry season lasts about five months, from May to September (MOURA et al., 2012). In the northern parts, a drier climate prevails between July and November (VIEIRA et al., 2004). The area is characterized by three predominant forest types: Dense Ombrophilous Forest (Dse), Open Ombrophilous Forest (Asc) and Semi-Deciduous Forest (Fse) (IBGE, 2004).

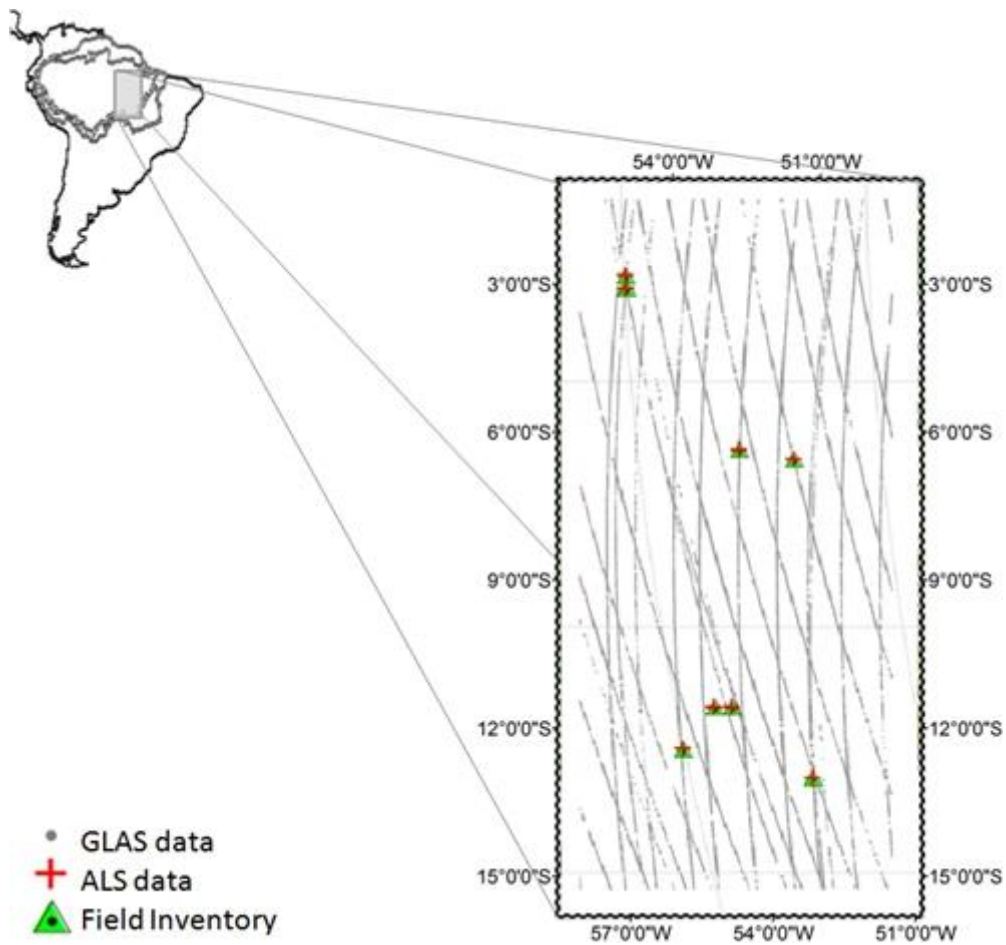


Figure 4.1. Location of the study area within the Amazon basin. The inset shows the Geoscience Laser Altimeter System (GLAS) coverage (strings), airborne laser scanning (ALS) data acquisition and the available field inventory plots across the Xingu basin.

4.2.2. Field inventory data

Estimates of vegetation structure were derived for each of the three different forest types using available inventory plots across the region. For two vegetation types (Asc and Fse), the surveys were provided by the Sustainable Landscapes Brazil project in collaboration with the Brazilian Agricultural Research Corporation (EMBRAPA), the US Forest Service, the USAID, and the US Department of State

(<http://mapas.cnpm.embrapa.br/paisagenssustentaveis/>). The Asc forest type was represented by 22 plots of 40 m x 40 m each. All the trees with a diameter at breast height (DBH) equal to or greater than 10 cm were measured within each plot. For Fse, 10 sample plots (20 m x 500 m) were used. The field data for Dse was obtained in 2012 and described by Silva et al. (2014). The floristic and structural surveys included seven sample plots of 25 m x 100 m over mature forests. Trees with DBH equal to or greater than 10 cm were measured within each plot.

4.2.3. Airborne Laser Scanning (ALS) data

ALS data were acquired by GEOID Ltd. using an Altm 3100/Optech instrument and provided by the Sustainable Landscapes Brazil project (<http://mapas.cnpm.embrapa.br/paisagenssustentaveis/>). The positional accuracy (1σ) of the LiDAR measurements was approximately 0.10 m horizontally and 0.12 m vertically. We used ALS data to obtain structural information in the Tapajós National Forest, Pará State between September and November 2012, for São Félix do Xingu municipality, Pará state (August 2012) and Canarana/Querência municipality, Mato Grosso State (August 2012), to represent Dse, Asc and Fse, respectively. Table 1 shows the specifications of LiDAR data for each site.

Table 4.1. Characteristics of the airborne laser scanning (ALS) data acquired over Dense Ombrophilous (Dse), Open Ombrophilous (Asc) and Semi-Deciduous (Fse) Forests in the Brazilian Amazon.

Forest Type	Total area (ha)	Maximum flight altitude (m)	Flightline overlap (%)	Average return density (ppm ²)	Average first return density (ppm ²)	Field of view (°)
Dse	1049	850	65	25.1	15.28	11.1
Asc	1004	850	65	24.1	15.20	11.0
Fse	1005	850	65	13.7	7.05	11.0

ALS data were delivered as classified LAS-formatted point clouds, along with 1-m resolution bare earth digital terrain models (DTM). For comparison with GLAS, discrete-return data were aggregated to produce pseudo-waveforms. Waveforms were

synthesized by subsetting the LiDAR point cloud co-located with each field plot and counting the number of points observed in vertical bins of 50 cm. In each resulting waveform, the ground (i.e. 0 m) was defined as the vertical bin showing the maximum amplitude in the elevation range associated with the returns classified as “ground”. Using samples of 1 x 1 km of ALS data for each vegetation type, canopy volume models (CVMs) were obtained to quantify the three-dimensional structure of the forest canopies based on the incident radiation levels and photosynthetic potential (HILKER et al., 2010; LEFSKY et al., 2005). The models divide the canopy space into sunlit and shaded vegetation elements as well as gap spaces enclosed within.

4.2.4. GLAS/ICESat data and structural metrics from vertical profiles

We used cloud-free GLAS profiles obtained across the Xingu basin (Figure 1) between 2006 and 2008 (laser operating periods 3E through 2D). Each GLAS footprint is elliptical in shape, spaced at approximately 170-m intervals along-track. In general, the GLAS LiDAR profiles characteristics varied between the campaigns across the study area. The near-infrared elliptical footprint and eccentricity varied between 51.2 (± 1.7) to 58.7 (± 0.6) and 0.48 (± 0.02) to 0.59 (± 0.01), respectively, while the horizontal and vertical geolocation accuracy varied between 0.00 (± 3.41) to 1.72 (± 7.36) and 0.00 (± 2.38) to 1.2 (± 5.14), respectively.

To process GLAS waveforms, we used parameters reported in the GLA01, GLA05, and GLA14 data products following methods described by (GONÇALVES, 2014). First, the waveforms were filtered by convolution with a discrete Gaussian kernel with the same standard deviation as the transmitted laser pulse. This procedure reduced the background noise, while preserving an adequate level of detail for characterization of the canopy (SUN et al., 2008).

The GLAS waveforms used in this study were calibrated and digitized into 1000 discrete bins at a time resolution of 1 ns (~ 15 cm). The locations of the highest (signal

start) and lowest (signal end) detected surfaces within the 150-m waveform were determined, respectively, as the first and last elevations at which the amplitude exceeded a threshold level, for a minimum of n consecutive bins. The peak of the ground return was determined as the lowest peaks in the smoothed waveforms with at least the same width as the transmitted laser pulse, after taking into account the mean noise level.

From the GLAS profiles, we extracted the maximum canopy height, defined as the vertical distance between the ground peak and the signal start. The mean canopy height (MCH) and the standard deviation (SD) of the height profile (HARDING, 2005) were calculated using Equations 1 and 2:

$$MCH = \frac{\int_0^{H100} z w(z) dz}{\int_0^{H100} w(z) dz} \quad (4.1)$$

$$SD = \sqrt{\frac{\int_0^{H100} z^2 w(z) dz}{\int_0^{H100} w(z) dz} - MCH^2} \quad (4.2)$$

where $w(z)$ is the laser power received from the 15-cm bin centered at height z ;

Entropy, a measure of canopy structural diversity, sensitive to crown depth and leaf area (PALACE et al., 2015; STARK et al., 2012), was used as a proxy of canopy roughness.

Entropy (S_z), was calculated using Equations 3 and 4:

$$S_z = - \sum_{i=1}^{n_b} p(w_i) \ln(p(w_i)), \text{ with} \quad (4.3)$$

$$p(w_i) = \frac{w_i(z)}{\int_0^{H100} w_i(z) dz} \quad (4.4)$$

where n_b is the number of vertical bins from the ground peak to the signal start, and $w(z)$ and z are defined as in Equation 1 and 2, but with a vertical resolution of ~ 1 m.

4.2.5. SeaWinds/QuikSCAT data

Estimates of canopy structure were also obtained from SeaWinds Scatterometer data, provided by NASA's Scatterometer Climate Record Pathfinder project. The SeaWinds Scatterometer operates at microwave frequency of 13.4 GHz (Ku-band) with mean incidence angle of 54° for V-polarization and 46° for H-polarization. The sensitivity of radar data to variations in vegetation canopy structure can be explained by the dependence of radar backscatter to surface dielectric properties, which are strongly dependent on the liquid water content of the canopy constituents (FROLKING et al., 2006). Given that the SeaWinds instrument operates at a higher frequency and higher incidence angle than other similar sensors, it has lower penetration into forest canopy. Therefore, it has almost no interference from soil moisture variations in densely vegetated forested areas (SAATCHI et al., 2013).

The product used in this study combines ascending (morning) and descending (evening) orbital passes, and is based on SeaWinds "egg" images (FROLKING et al., 2006). The nominal image pixel resolution for egg images is 4.45 km/pixel. Only backscatter data for horizontal (H) polarization were used in this study, given that previous assessments indicate that results using vertical (V) polarization showed no significant differences (Saatchi et al., 2013). We used data obtained from January 2001 to November 2009, when the sensor stopped collecting data due to failure in the scanning capability. To better match the anisotropy observations from the MODIS instrument, we resample the nominal spatial resolution of the SeaWinds from 4.45 km to 1 km.

4.2.6. Determination of surface anisotropy from multi-angle MODIS data

Using Ross-Thick Li-Sparse (RTLS) model (Wanner et al., 1995), we characterized the bidirectional reflectance distribution function (BRDF) of each 1 km x 1 km grid cell of MODIS data. Based on the RTLS BRDF model, we derived MODIS backscatter ($SZA = 45^\circ$, $VZA = 35^\circ$, $RAA = 180^\circ$) and forward scatter ($SZA = 45^\circ$, $VZA = 35^\circ$, $RAA = 0^\circ$) observations for a fixed view and sun angle. We used estimates of anisotropy, defined as the difference between backscattering and forward scattering, based on the Enhanced Vegetation Index (EVI) to describe roughness of the surface for different vegetation types across the study area. The objective of using EVI rather than surface reflectance of a given band was to minimize the effect of non-photosynthetically active elements (i.e. soil fraction component) while optimizing the sensitivity to green canopy structure.

MODIS-derived anisotropy values were regressed against ALS-derived entropy, GLAS-derived entropy and SeaWinds/QuikSCAT backscatter (σ_0), which were estimated on a per-pixel-basis to generate time series profiles of entropy for each forest type in the study area.

4.3. Results

The Xingu basin contains different forest types. However, it is dominated by Asc and Dse in the north, and by Fse in the south, as illustrated in the vegetation map (Figure 4.2). The GLAS tracks are also shown in this figure to highlight the sampling density of the spaceborne LiDAR over each forest type. An illustration of the mean canopy height (MCH) derived from ALS for three sample areas of 1 ha each is provided in Figure 4.2. Airborne ALS measurements showed in average the greatest tree heights in the Dse domain with values up to 40 meters tall (red color in the inset of Figure 4.2). Asc and Fse reached up to 30 m and 25 meters in height, respectively.

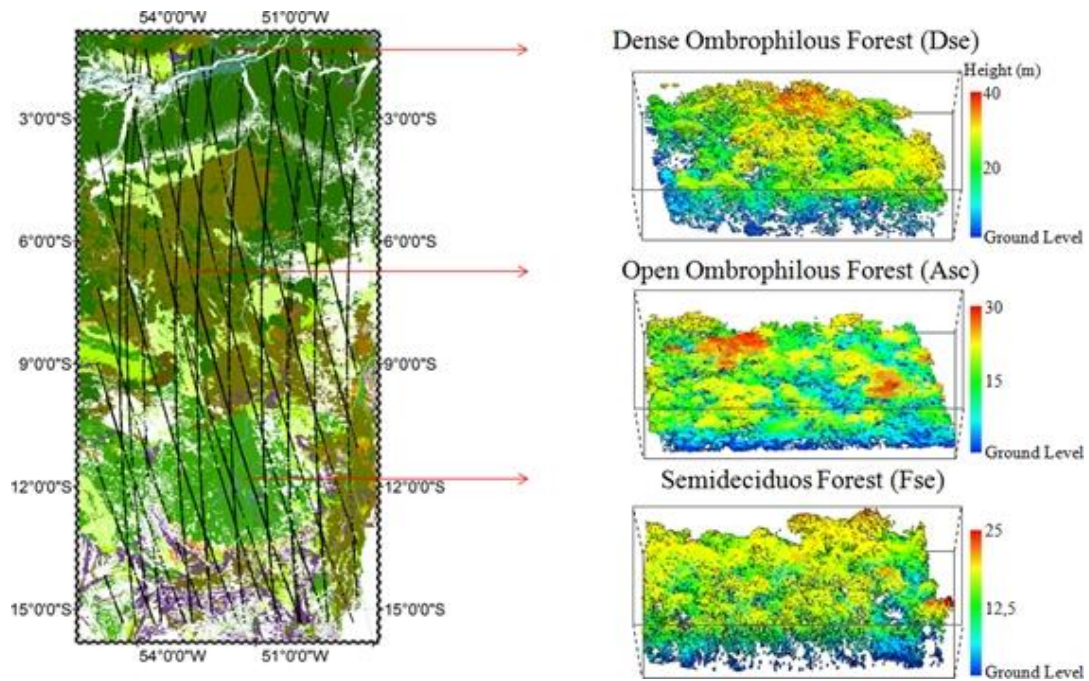


Figure 4.2. Vegetation cover map adapted from IBGE (2004) in the left and diagrams of height estimates from ALS LiDAR data in the right to illustrate structural variation between the three predominant forest types in the study area (Dse, Asc and Fse). Each Airborne Laser Scanning (ALS) plot represents an area of 100 m x100 m to describe the heights values in the three different forests.

LiDAR derived mean tree heights were consistent with existing field measurements, which showed that mean canopy heights from forest inventories were 19.8 m, 17.4 m and 17.0 m for Dse, Asc and Fse, respectively (Table 1). When compared to Asc and Fse, Dse presented larger values of metrics of diversity (species richness (S) and Shannon index (H')) and structure (mean height (HT), mean diameter at breast height (DBH), basal area (BA) and leaf area index (LAI)) (Table 4.2).

Table 4.2. Floristic and structural metrics calculated from field inventory data (<http://mapas.cnpm.embrapa.br/paisagenssustentaveis/>) for Dense Ombrophilous Forest (Dse), Open Ombrophilous Forest (Asc) and Semi-Deciduous Forest (Fse). The mean leaf area index (LAI), determined from Airborne Laser Scanning (ALS), is indicated in the last column of the table.

Forest Type	Plots	S	H'	H _{t(m)}	BA _(m²m⁻²)	LAI _(ALS)
Dse	7	181	4.61	18.1	30.63	6.05
Asc	22	1595	3.67	17.4	11.36	4.32
Fse	10	802	2.20	17.0	12.83	5.33

Differences in canopy structure were also evident from the analysis of canopy volume models (CVMs) (Figure 4.3). While gap spaces were relatively small in all three vegetation types, Asc showed a notably higher proportion of sunlit vegetation that reached down deep into the canopy, suggesting a higher spatial variability of tree heights compared to the other two vegetation types. Similarly, gaps in the upper canopy were mostly present in Asc, as expected for open forest types. Fse showed gaps predominantly in lower height levels, and a higher overall proportion of shaded crown. The total contribution of the components of the canopy (100% of the canopy space filled by either sunlit or shaded canopy elements or fully enclosed gap space) was reached at about 15 m height for both Asc and Dse, and at about 20 m height for Fse.

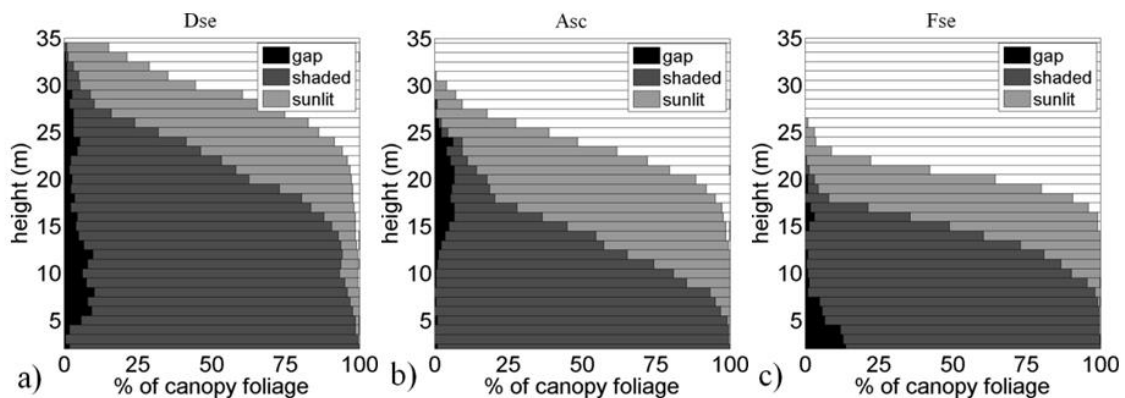


Figure 4.3. Canopy volume models (CVMs) based on the Airborne Laser Scanning (ALS) for (a) Dense ombrophilous forest (Dse); (b) Open ombrophilous Forest (Asc); and (c) Semi-deciduous forest (Fse).

Differences in vegetation structure derived from ALS data were confirmed also with spaceborne GLAS observations. GLAS-derived seasonal profiles of entropy for 2006 showed spatial averages that differed over time between the three vegetation types (Figure 4.4). Despite the differences in the years of data acquisition (2006 for GLAS and 2012 for ALS), the shaded area in Figure 4 was plotted only for reference between the airborne and spaceborne data. GLAS derived seasonal profiles varied between different forest types. The lowest values of entropy were found for the Fse. In contrast, Asc for Dse showed GLAS entropy consistently higher throughout the measurement period. All forest types showed strong seasonality with increasing entropy from February to September, and decreasing values thereafter with predominance of higher entropy during the dry season.

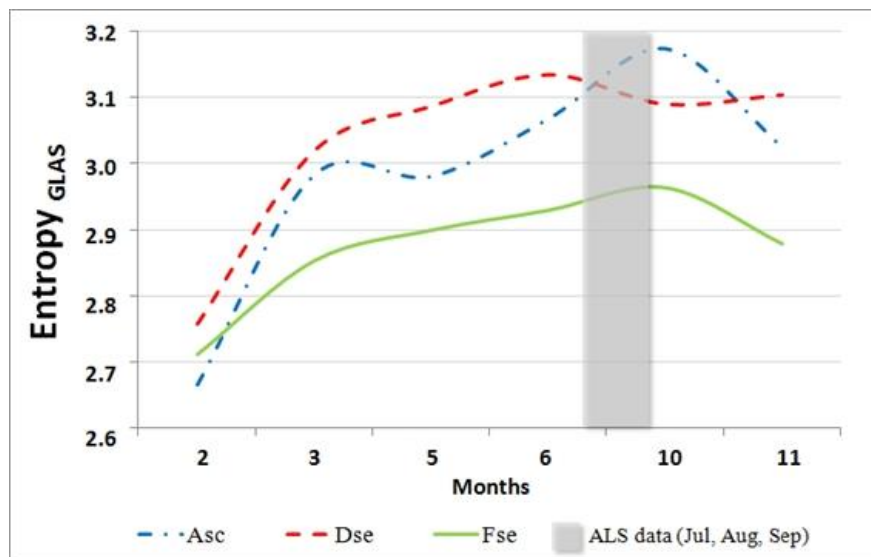


Figure 4.4. Seasonal profiles of GLAS-derived entropy for the three different forest types of the study area. GLAS data were obtained only for the months indicated in the x-axis. Just for reference, the shaded area represents the quarter when the Airborne Laser Scanning (ALS) data were collected in 2012.

Examples of MODIS anisotropy during March, June and October of 2006 illustrated seasonal and spatial changes in multi-angle reflectance across the Xingu basin (Figure 4.5). The MODIS anisotropy was consistently higher in the northern part of the study area, and its spatial distribution coincided well with the forest types indicated in Figure

4.2. A clear limit between forested (high MODIS anisotropy) and non-forested (low anisotropy) areas was evident in the southern part of the map. Furthermore, higher values of anisotropy were found for the Asc and Dse compared to the Fse. While MAIAC observations allowed a notable number of measurements of anisotropy between June (Figure 4.5b) and October (Figure 4.5c), some data gaps were observed in March (Figure 4.5a) due to cloud cover in the rainy season.

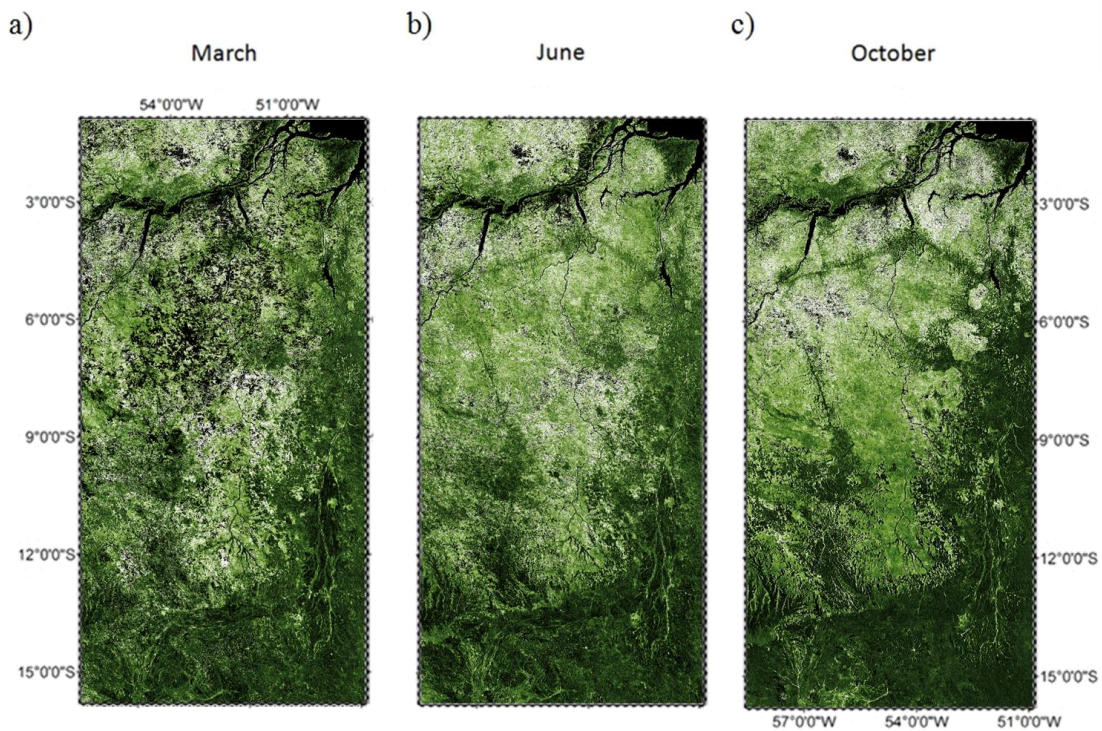


Figure 4.5. MODIS-derived anisotropy images during (a) March, (b) June and (c) October of 2006 to illustrate seasonal and spatial changes in multi-angle reflectance across the Xingu basin.

MODIS-derived anisotropy was linearly correlated to ALS-derived entropy (Figure 4.6). The coefficient of determination (r^2) of the relationship spanning the MODIS pixels that had coinciding within ALS observations was 0.54 and the RMSE was 0.11 units of entropy. Much of the scattering presented in Figure 4.6 was limited to lower values of entropy while the residuals for the higher entropy range were reduced.

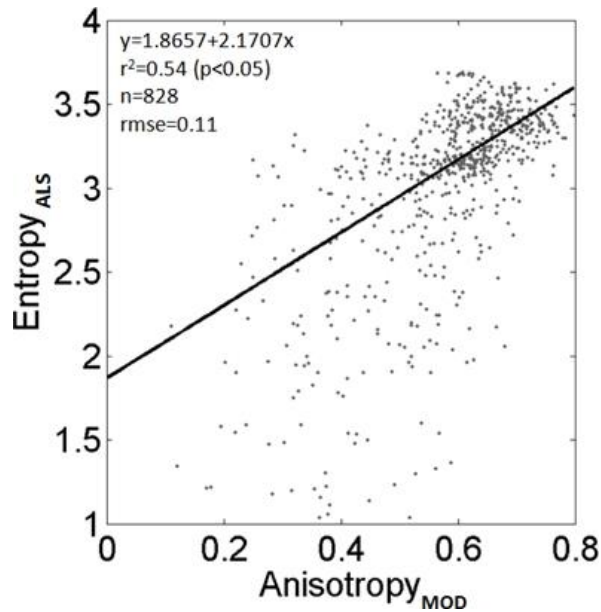


Figure 4.6. Relationship between MODIS-derived anisotropy and ALS-derived entropy (or canopy roughness).

When we correlated the MODIS anisotropy with the GLAS entropy using GLAS data with five or more shots per 1 km x 1 km MODIS, significant relationships were obtained (Figure 4.7). In order to examine seasonal variability in the relationship, we performed the regressions separately for March (Figure 4.7a), June (Figure 4.7b) and October (Figure 4.7c) of 2006. The coefficient of determination varied between 0.52 for March and 0.61 for June ($p < 0.05$) with similar slopes and offsets found throughout the observation period. RMSE varied between 0.26 and 0.30 units of entropy. The highest noise levels in the relationship were observed in March, which is corresponding also to the larger amount of data gaps during the rainy season (Figure 4.5). The availability of GLAS data was somewhat limited during June, but the relationships were still highly significant and consistent with those observed during other months of the year.

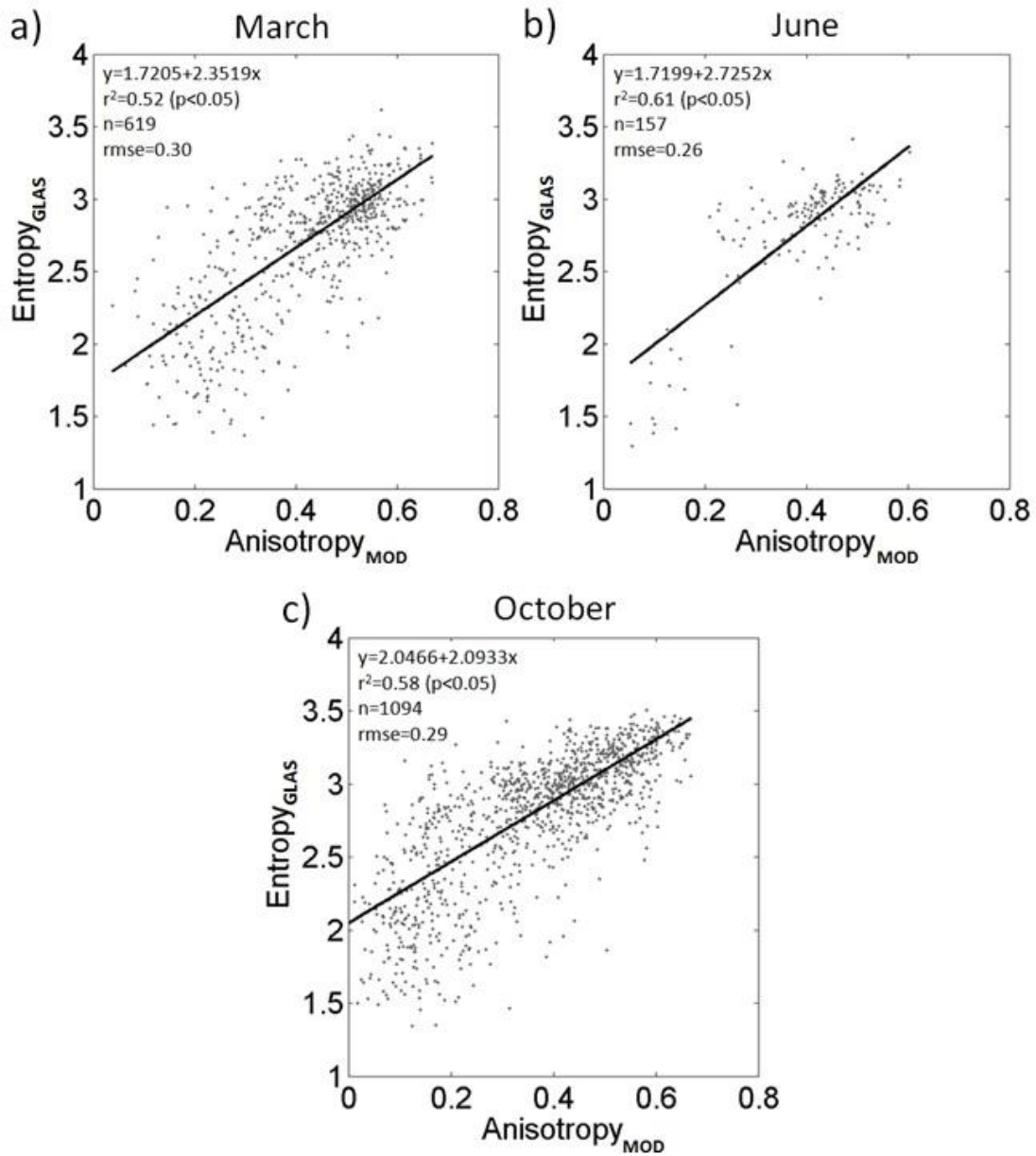


Figure 4.7. Relationship between MODIS-derived anisotropy and GLAS-derived entropy using observations for (a) March, (b) June and (c) October of 2006.

A strong relationship between the MODIS-derived anisotropy and the backscattering measurements (σ^0) from SeaWinds/QuikSCAT is also observed (Figure 4.8). The relationship was obtained for 10,000 randomly sampled MODIS pixels and corresponding SeaWinds/QuikSCAT (σ^0) observations across the Xingu basin for all available QuikSCAT data between 2001 and 2009. It should be noted, however, that

when using radar observations, the relationship to MODIS-derived anisotropy was non-linear ($r^2=0.59$, RMSE=0.11).

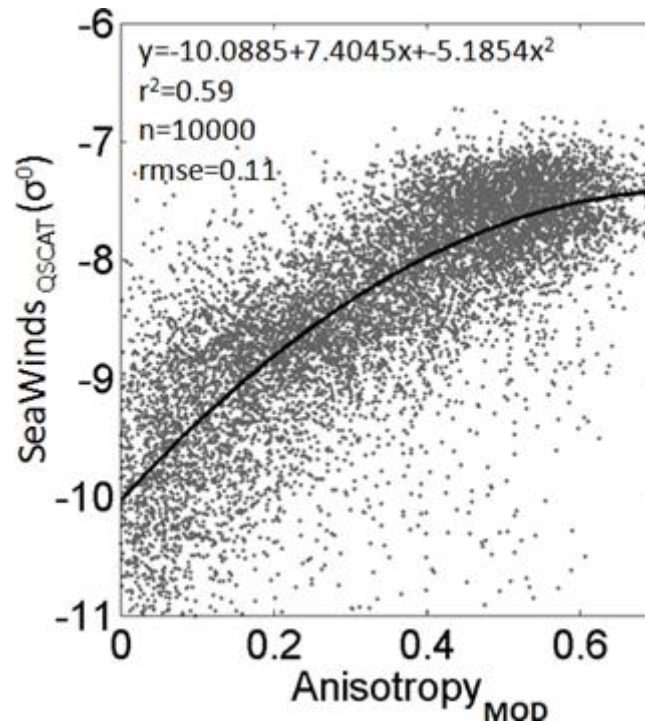


Figure 4.8. Relationship between MODIS-derived anisotropy and backscattering (σ^0) measurements from SeaWinds/QSCAT over Amazonian tropical forests considering the period 2001 to 2009.

Time series profiles of MODIS-derived entropy estimated from the regression model of Figure 4.7c and of MODIS-derived QuikSCAT- σ^0 estimated from model of Figure 4.8 were plotted as spatial averages for Dse, Asc and Fse (Figure 4.9). All three forest types displayed notable seasonal cycles, in terms of temporal variation as well as in terms of differences between vegetation types. The Ombrophilous Forests (Dse and Asc) consistently showed high values of entropy with less seasonal variation. By contrast, the seasonal cycles were much more pronounced in the Fse, as expected for semi-deciduous vegetation. Both models (GLAS-derived entropy and QScat-derived σ^0) yielded very similar seasonal patterns, in terms of temporal variation as well as in terms of differences between vegetation types. The results presented in Figure 4.9 were consistent also with those shown in Figure 4.4. A small negative trend in both entropy

and σ_0 was observed from 2000 until 2009 and a positive trend in all three vegetation types was found from 2010 onwards. This trend was especially pronounced for the canopy entropy based on GLAS observations.

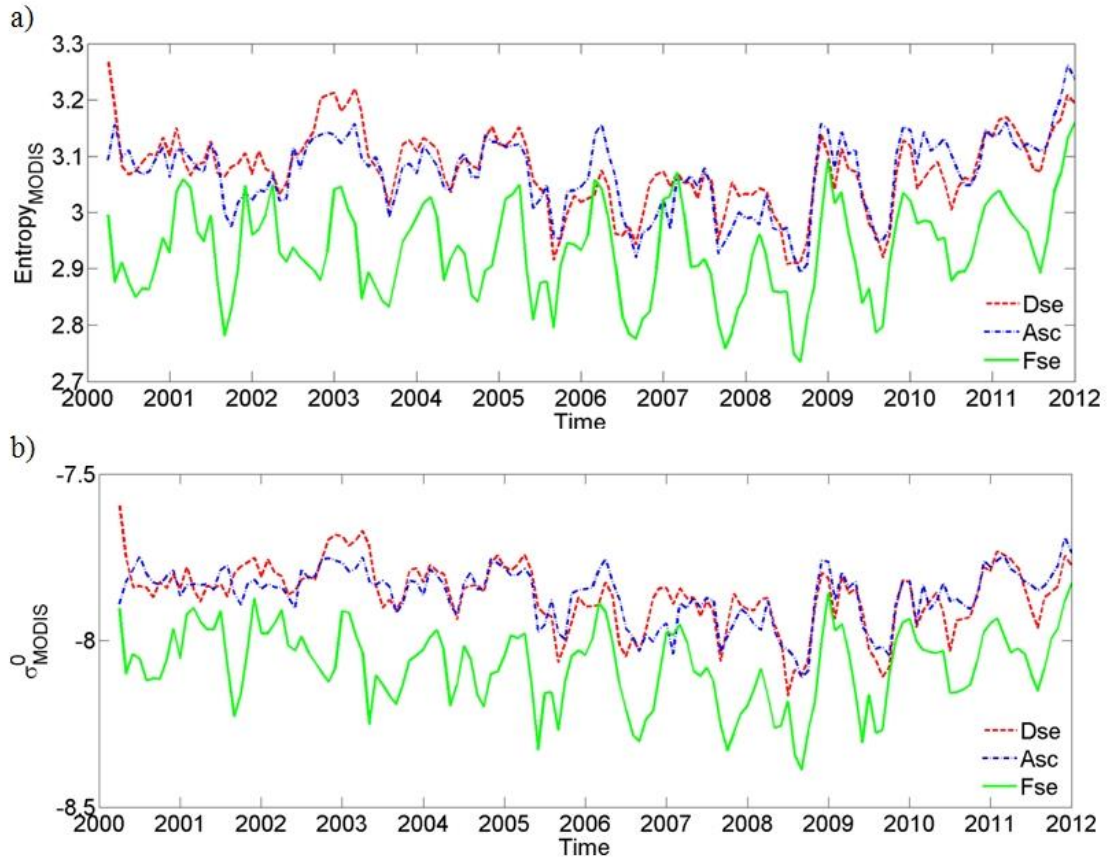


Figure 4.9. Time series profiles of MODIS-derived (a) GLAS entropy estimated using the regression model of Figure 4.7c, and (b) MODIS-derived SeaWinds/QuikSCAT backscattering (σ_0) from the model of Figure 4.8. Results are shown as spatial average for Dense (Dse) and Open (Asc) Ombrophilous Forests and the Semi-Deciduous Forest (Fse) between 2000 and 2012 for the Xingu basin.

4.4. Discussion

This study investigated the potential of multi-angle reflectance obtained from MODIS to derive estimates of vegetated surface roughness as an important structural parameter of land atmosphere interactions. Aside from field observations, airborne laser scanning is arguably the most comprehensive tool to describe the three-dimensional vegetation structure at the stand level (COOPS et al., 2007; LIM et al., 2003b; WULDER et al.,

2012) to date. Recent initiatives such as the “Sustainable Landscapes Brazil“ project (<http://mapas.cnpm.embrapa.br/paisagenssustentaveis/>) seek to improve upon existing lack of data availability and provide new opportunities to generate structural metrics across discrete locations within the Amazon basin.

LiDAR based characterization of vegetation structure (Figures 4.2, 4.3, 4.4 and Table 4.2) exposed a large heterogeneity across the Xingu basin, both spatially and seasonally. ALS observed structural differences between vegetation types that were detectable also from space using photon counting LiDAR (GLAS/IceSat) and microwave backscattering (SeaWinds/QuikSCAT) (Figures 4.4 and 4.9b). This is an important finding, as it opens an opportunity for scaling spatially discrete observations of canopy structure across larger areas from space (POPESCU et al., 2011).

Spatial and temporal heterogeneity in Amazonian vegetation (SILVA et al., 2013a; TOWNSEND et al., 2008) is not easily obtained from conventional vegetation indices (HILKER et al., 2015a), as VIs cannot adequately capture differences in canopy structure among different vegetation types (GLENN et al., 2008; LAGOUARDE et al., 2002). Findings presented in this study (Figures 4.6 to 4.9) suggest that such canopy structural variation may be determined from multi-angular reflectance. The ability of multi-angle observation to derive vegetation structural attributes is well supported by previous results (CHEN; LEBLANC, 1997; CHEN et al., 2003; GAO, 2003b; STRAHLER; JUPP, 1990; YU et al., 2015; ZHANG et al., 2002). While these authors have focused on smaller study areas using specialized sensors, our findings confirm such multi-angle potential to be acquired from the MODIS instrument. This is an important advancement, as it would allow structural estimates over large areas and at high temporal frequencies from space, complementing the data analysis of orbital LiDAR data.

While the range of view angles acquired by MODIS is relatively small, as the instrument was not specifically designed for multi-angle acquisitions, MODIS-derived anisotropy still provided an effective means to characterize vegetation structure across large areas from space. Within the Amazon basin (or tropics in general), this is partially

facilitated by the fact that MODIS view geometry comes very close to the principal plane twice a year. As a result, our BRDF model is representative at the angles used in this study. Consequently, modeled anisotropy is close to its maximum range of possible values, contrary to observed in mid-latitudes where observation are further from the principal plane. In these cases, other geometric configurations might be preferable.

Modeling MODIS anisotropy using the RTLS BRDF model further allowed us to derive anisotropy independent of the sun-observer geometry (ROUJEAN, 2002). As a limitation to this approach, changes in the sun-sensor configuration over the year do not always allow modeling the forward and backscattering observations within the sampling range of the MODIS instruments. Therefore, higher uncertainties may be observed during some times of the year than during others.

The strong and positive correlation found between GLAS-measured entropy and MODIS anisotropy (Figure 4.7) may be explained by geometric scattering of individual tree crowns (CHOPPING et al., 2011; LI, X., STRAHLER, 1986). For instance, a large variability in canopy heights (high canopy roughness) will increase the geometric scattering component, especially of NIR reflectance. However, other structural changes may also influence seasonal patterns of anisotropy, as the canopy optical thickness. In addition to canopy roughness, anisotropy is also affected by leaf angle distribution (ROUJEAN, 2002) and foliage clumping (CHEN et al., 2005) among other variables related to the floristic variability, which tends to be high in tropical forests. The interaction between these variables and multi-angle scattering is not straightforward, requiring further investigation, especially in the components of scattering determined in the RTLS model. For example, increases in leaf area may increase the volumetric scattering component (ROSS, 1981; ROUJEAN et al., 1992) of multi-angle reflectance, but at the same time decrease the surface roughness, at least within a certain range of values. Therefore, the results presented in here should be understood as a first demonstration of the technique.

Due to the complexities described as well as other limitations in terms of footprint size, and range of angular sampling, MODIS-derived estimates of canopy structure should

not be understood as a replacement for direct 3D measures of vegetation, but rather as a complimentary approach for scaling such observations in space and time. The consistency in the modeled relationship obtained from GLAS LiDAR and SeaWinds/QuikSCAT backscattering is encouraging in this respect, suggesting that such scaling approaches may be built on opportunistically sampled observations across platforms. For instance, MODIS data can help interpret estimates of canopy roughness in between GLAS footprints, as well as fill missing observations in time, enabling a more comprehensive seasonal and spatial analysis. Upcoming new LiDAR instruments, such as the Global Ecosystem Dynamics (GEDI) mission (DUBAYAH et al., 2014; STYSLEY et al., 2015), will allow further improvements in the measures of canopy structure, as well as, biomass.

4.5. Conclusions

Our analysis has demonstrated that multi-angular MODIS observations are suitable to determine canopy entropy at different scales of LiDAR measurements across the study area in the Amazon. The sparseness of existing, highly detailed LiDAR observations currently imposes severe restriction on accuracy of modeled carbon and water fluxes, particularly in remote regions, such as the Amazon basin. Complementary measures of vegetation structure from optical satellites are therefore highly desirable to extrapolate spatially or temporally sparse estimates of canopy structure across the landscape. Such approaches will be crucial for improving our understanding of climate tolerance and responses to Amazonian forests to extreme events.

5 USE OF MULTI-ANGLE MODIS ANISOTROPY TO STUDY SEASONAL AND DROUGHT EFFECTS IN THE AMAZONIAN FORESTS

5.1. Introduction

Vulnerability of tropical forests to climate change has received broad attention by the scientific community as increase in equatorial sea surface temperature (SST) can lead to longer dry seasons (FU et al., 2013; MARENGO et al., 2011) and more frequent, severe drought events (LEWIS et al., 2011; MALHI et al., 2009; MARENGO et al., 2008). The feedbacks of such drying on global climate change could be substantial; the Amazon rainforest alone accounts for about 15% of global photosynthesis and host perhaps a quarter of the world's terrestrial species (MALHI et al., 2008). Field studies have indicated that such extreme drought events could alter species composition, biodiversity (ASNER; ALENCAR, 2010; ASNER et al., 2004; PHILLIPS et al., 2009) and plant productivity (ARAGAO et al., 2007; GATTI et al., 2014; MEIR et al., 2008).

Over the last decade, the Amazon region has experienced two severe droughts, one in 2005 and another in 2010 (MARENGO et al., 2011). However, the broad scale response of vegetation to these events remains controversial. (SALESKA et al., 2007b) reported an increase in greenness (higher EVI) for the 2005 drought, a result that was subsequently challenged (ATKINSON et al., 2011; SAMANTA et al., 2010). Xu et al., (2011) observed a widespread decline in greening for the 2010 drought. Similarly, the prevailing view of seasonality of vegetation has recently been discussed. Several findings (BRANDO et al., 2010; GRAHAM et al., 2003; HUETE et al., 2006a; HUTYRA et al., 2007; MYNENI et al., 2007; SAMANTA et al., 2012a; WAGNER et al., 2013) support the view that photosynthetic activity increases initially during the dry season in response to an increase in incident photosynthetically active radiation (PAR). However, a recent study based on NASA's Moderate Resolution Imaging Spectroradiometer (MODIS) (MORTON et al., 2014) argued that seasonal changes are driven by artifacts of the sun-sensor geometry.

A growing body of literature suggests uncertainties in remote sensing of atmospheric aerosol loadings (SAMANTA et al., 2011; 2012a) and deficiencies in cloud detection (HILKER et al., 2012b) to be partially responsible for these contradicting results. While progress has been made addressing some of these challenges by using alternative datasets (HILKER et al., 2014) or higher spatial resolution imagery (ZELAZOWSKI et al., 2011), observations based on remotely sensed vegetation indices are limited in their ability to detect changes in vegetation cover. This occurs especially due to a well-documented saturation effect in areas with high biomass and leaf area (CARLSON; RIPLEY, 1997).

As an alternative to observations from only one view angle, the combination of multiple view angles may provide new opportunities to mitigate these saturation effects, and allow better insights into seasonal and inter-annual changes of tropical forests. Biophysical changes in the canopy structure affect the directional scattering of light and these effects are observable from multi-angular data (CHEN et al., 2005). With the advance of multi-angular sensors such as the Multi-angle Imaging SpectroRadiometer (MISR) (DINER et al., 1998), progress has been made in describing the dependence of reflectance on observation angles (BARNESLEY et al., 2004a; DINER et al., 1998). For instance, the angular component of surface reflectance (anisotropy) has been linked to optical properties and geometric structure of the target (WIDLOWSKI et al., 2004, 2005a) such as canopy roughness (STRAHLER, 2009b), leaf angle distribution (ROUJEAN, 2002), leaf area index (LAI) (WALTHALL, 1997) and foliage clumping (CHEN et al., 2005).

The theoretical basis for the influence of canopy structure on multi-angle reflectance has been developed (BICHERON, 1999; CHEN et al., 2003; GAO, 2003b; LEBLANC et al., 2005; MYNENI et al., 2002). However, multi-angle reflectance is not easily obtained from traditional surface reflectance algorithms, even when data is acquired from multiple view angles. Pixel based algorithms often assume a Lambertian reflectance model, which reduces the anisotropy of the derived surface reflectance (LYAPUSTIN; MULDASHEV, 1999; WANG et al., 2010), thus decreasing the ability to detect directional scattering (HILKER et al., 2009).

New methods for processing remote sensing data, such as the Multi-Angle Implementation of Atmospheric Correction (MAIAC), can help overcome this limitation by using a radiative transfer model that does not make a Lambertian assumption (LYAPUSTIN; KNYAZIKHIN, 2001). MAIAC is a cloud screening and atmospheric correction algorithm that uses an adaptive time series analysis and processing of groups of pixels to derive atmospheric aerosol concentration and surface reflectance. A detailed description of the algorithm can be found in Lyapustin et al., 2011, 2012a. In this Chapter, we take advantage of MAIAC to study changes in anisotropy across the Amazon basin using thirteen years of multi-angle MODIS observations. We define anisotropy as difference in reflectance between the backscattering (relative azimuth angle (RAA) = 180°) and the forward scattering (RAA = 0°) directions for a fixed view and sun zenith angle. Estimates of such defined anisotropy were then related to field and LiDAR-based estimates of LAI in order to validate its relation to vegetation structure. Our objectives were to demonstrate spatial and temporal changes in anisotropy, particularly during the onset of the dry season as a measure of changes in vegetation. We re-visited the two last major droughts in the Amazon basin (2005 and 2010) to evaluate anomalies in anisotropy and investigate vegetation response to these drought events on a monthly basis.

5.2. Material and Methods

5.2.1. LiDAR and field based estimates of Leaf Area

Estimates of anisotropy were validated against existing and independent field observations of LAI ($n = 16$) obtained from the literature (ANDREAE, 2002; DOMINGUES et al., 2005; DOUGHTY; GOULDEN, 2008; FIGUERA et al., 2011; GALVAO et al., 2011; MALHI et al., 2009; NEGRÓN JUÁREZ et al., 2009; RESTREPO-COUBE et al., 2013; SCURLOCK et al., 2001; ZANCHI et al., 2009), and Airborne Laser Scanning (ALS) as an example of a measure of canopy structure. LiDAR data were acquired by the Sustainable Landscapes Brazil project supported by the Brazilian Agricultural Research Corporation (EMBRAPA), the US Forest Service,

USAID, and the US Department of State. A detailed description of the LiDAR data can be found at <http://mapas.cnpm.embrapa.br/paisagenssustentaveis>. In order to allow a comparison between LiDAR based LAI and anisotropy, the area of airborne LiDAR acquisition was first subdivided into 1x1 km tiles matching the MODIS pixels. The probability of canopy gap within each tile was then determined as the sum of the total number of hits down to a height z , relative to the total number of independent LiDAR shots (N) (LOVELL et al., 2003; READING et al., 2006):

$$P_{gap}(z) = \frac{1 - \sum_{z=j}^{z=z_{max}} \#z_j}{N} \quad (5.1)$$

where $\#z$ is the number of hits down to a height z above the ground (or the range to which the gap probability is taken). Finally, the leaf area profile $L(z)$ was modeled as a logarithmic function of P_{gap} (LOVELL et al., 2003) assuming an exponential extinction of light within the canopy:

$$L(z) = -\log(P_{gap}(z)) \quad (5.2)$$

A detailed description of the method applied can be found in (COOPS et al., 2007).

5.2.2. Estimates onset and duration of Amazon dry seasons

The most common period used in the literature for describing dry seasons across Amazonia is June through September (SALESKA et al., 2007a; SAMANTA et al., 2010; XU et al., 2011). It is, however, widely acknowledged that the actual onset and duration of the dry season varies greatly across the Amazon basin (SILVA et al., 2013b). In order to investigate the effects of regional variability in precipitation, onset and length of dry season were calculated for each year using monthly estimates of water deficit from precipitation obtained from Tropical Rainfall Measuring Mission (TRMM) (3B43 v7 and 7A, at 0.25° spatial resolution). TRMM data has been extensively used to characterize the seasonal and inter-annual variability in rainfall across the Amazon region (ARAGAO et al., 2007). Dry season months were determined by using the

assumption that moist tropical forests transpire about $100 \text{ mm.month}^{-1}$ (ANDERSON, 2012; ARAGAO et al., 2007): When rainfall drops below $100 \text{ mm.month}^{-1}$, evapotranspiration exceeds precipitation, and soil water availability declines (BORCHERT, 1998; STRAHLER; JUPP, 1990; WILLIAMS et al., 1998).

5.3. Results

Figure 5.1 illustrates the spatio-temporal variation in anisotropy by means of its first principal component (PC1) for the period between 2000 and 2012. The droughts years 2005 and 2010 were excluded from this analysis to only represent normal year variations. PC1 explained about 89% of the total variance in anisotropy; consequently, we focus on this first component to illustrate regional variability in the dataset. Red and yellow represent areas with relatively higher anisotropy, while green to white show areas with relatively lower anisotropy. Notable differences were found not only between the Amazonian rainforest and non-forested savannah regions, but also within the forested area itself (compare traditional vegetation indices for instance in Hilker et al., 2014). High anisotropy was found predominantly in the more densely forested areas in northern and eastern Amazonia whereas the open forest types in the southern regions yielded, on average, lower values of anisotropy. The point symbols in Figure 5.1 illustrate the plot locations for field-based observations of LAI and LiDAR-derived measurements. While the total number of independent LAI estimates is limited across remote forested areas such as the Amazon basin, the field locations presented in Figure 5.1 represented a reasonable range of forest types within the Amazon rainforest.

derived from airborne LiDAR (Figure 5.2b, $r^2=0.88$ $p<0.05$). Importantly, both relationships were found to be linear, at least within the observed range of $LAI \leq 7 \text{ m}^2 \text{ m}^{-2}$ and yielded an improved description of structure in densely vegetated areas compared to estimates obtainable from nadir EVI images alone (Figure 5.2c). The relationship between both field measured and LiDAR LAI estimates with anisotropy followed almost the identical linear functional form, which allowed us to describe leaf area across a range of vegetation types within the Amazonian rainforest from both data sources.

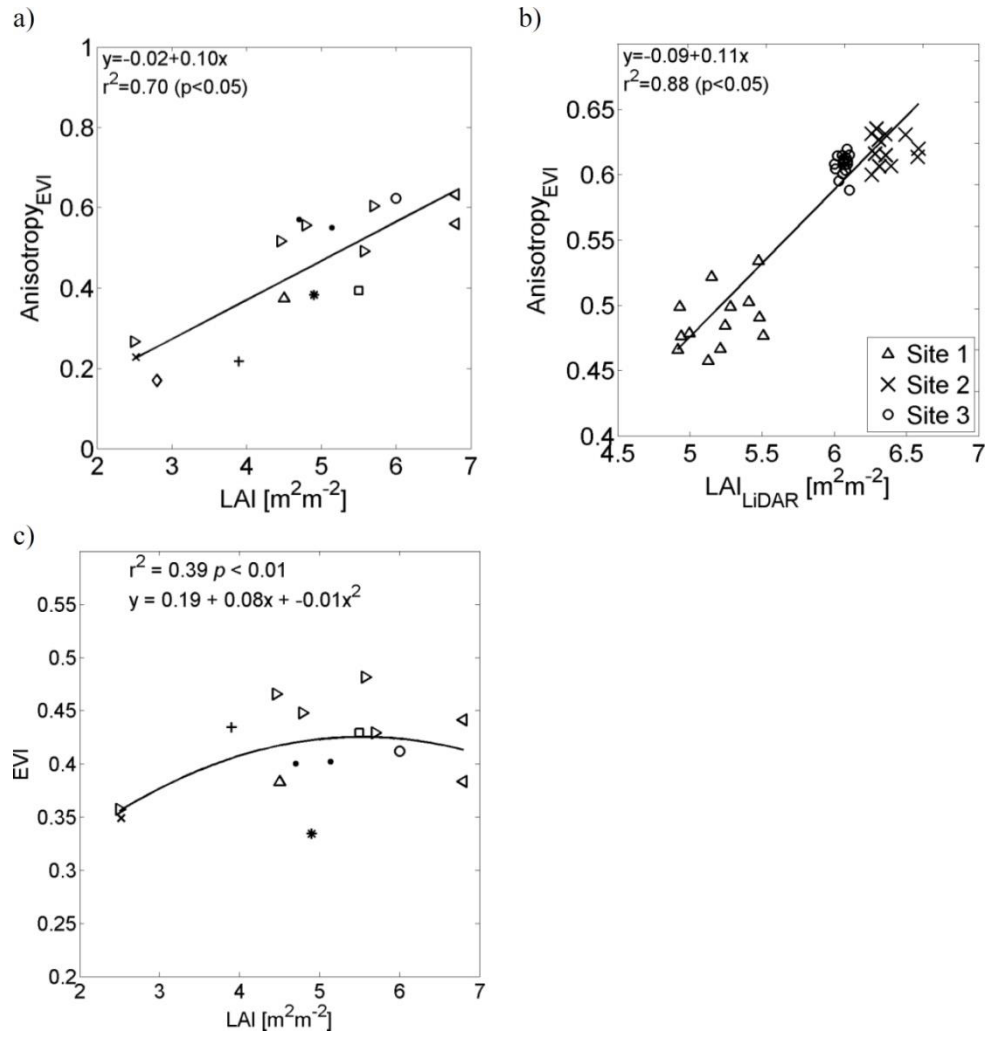


Figure 5.2. Relationship between anisotropy and LAI; a) from field values collected in the literature (see Figure 2), and b) from LiDAR estimates. c) Relationship between directionally normalized (nadir) EVI and LAI. The correlations were performed using the dates described in the field data with the closest MODIS acquisitions available. The location of the plots are provided in Figure 5.1. RMSE for Figures 5.2a and 5.2b were 0.08 and 0.02 (units of anisotropy), respectively.

In addition to a large heterogeneity in vegetation structure (Figure 5.1), our analysis confirmed also a large variability in precipitation across the basin (VILLAR et al., 2009). Figure 5.3 represents estimates of monthly water deficit. Areas with low water deficit are shown in blue, whereas red indicates high water deficits. Areas with no water

deficit are presented without color. High levels of water deficit were found in the northern Amazon region mainly between January and March, corresponding to the dry season in the northern hemisphere, whereas May to August marked the dry season months across large parts of the southern hemisphere. Overall, the largest water deficit was found during June and July (focusing on the south-eastern border of the Amazon), whereas the lowest levels of water deficit were observed during March, with precipitation exceeding 100 mm month⁻¹ almost across the entire basin. The beginning and length of dry season (Figures 5.4a and 5.4b, respectively) varied accordingly and followed a south-west north-east gradient with up to 5 months of water deficit in the south-west. By contrast, large areas of Amazonas state, central Amazon, showed, on average, no water deficit during the observed years (gray area in the map, compare also Steege; Pitman, 2003).

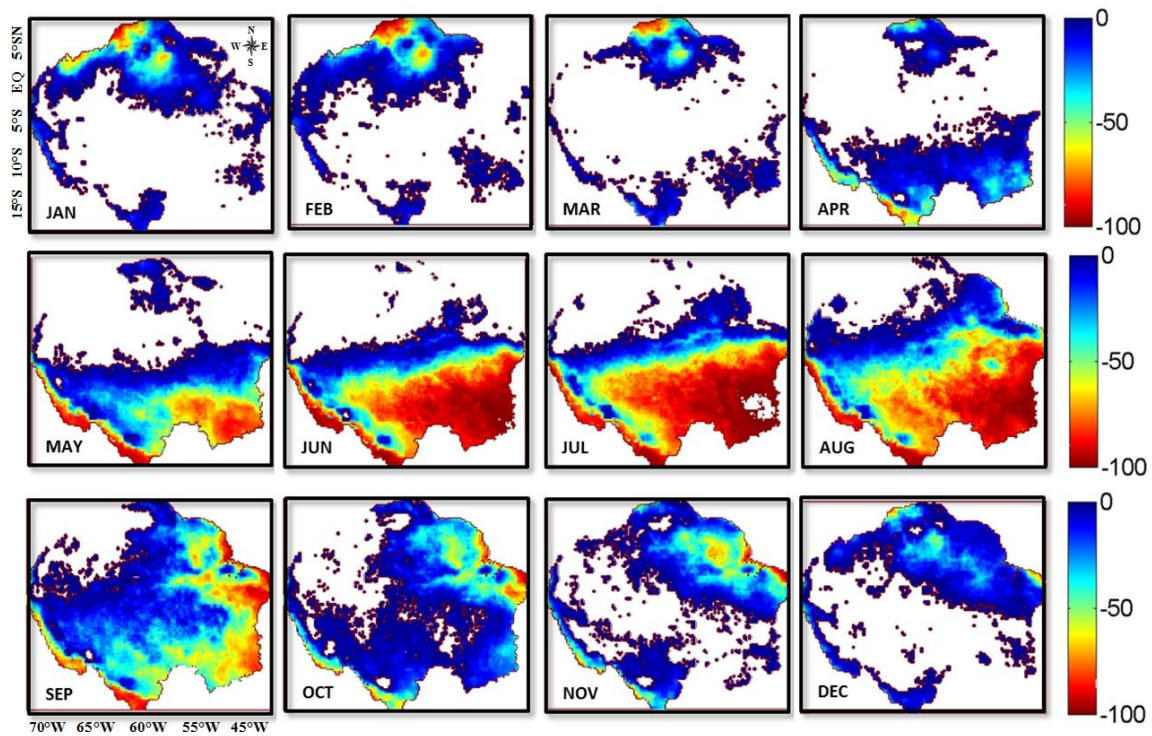


Figure 5.3. Monthly estimates of water deficit (in mm month⁻¹), based on TRMM observations from 1998 to 2012. Areas with low water deficit are shown in blue, whereas the red color indicates high water deficits; areas with no water deficit are presented without color.

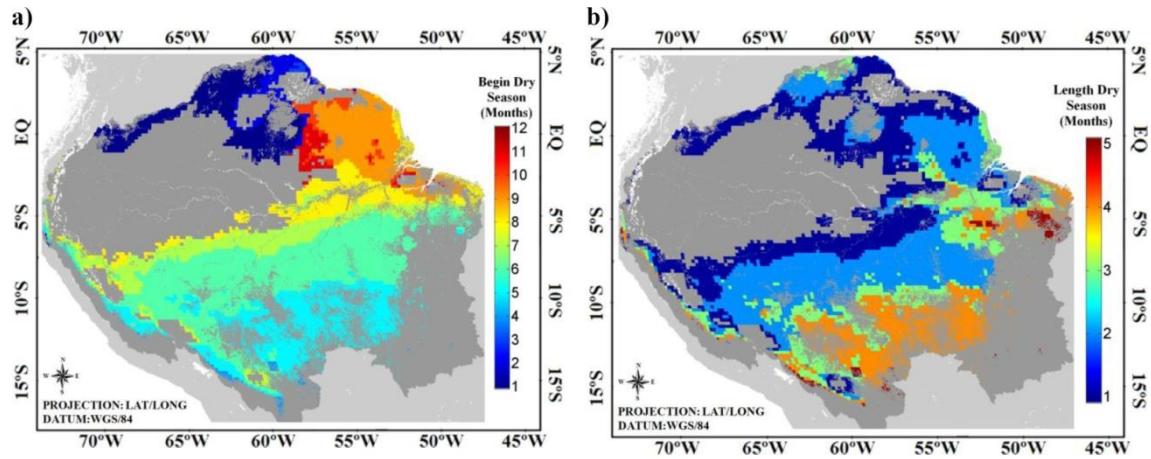


Figure 5.4. Beginning (a) and length (b) of dry season across the Amazon calculated on per pixel basis using monthly water deficits. This approach was performed for each year separately in order to consider inter-annual variability. The figure shows mean onset and length of dry season for all years.

Anisotropy changes in response to these seasonal variations in precipitation are shown in Figure 5.5. Figures 5.5a and 5.5b show total differences in anisotropy between beginning and end of the dry season (positive changes are labelled “greening”, negative changes are labeled “browning”; all changes are normalized with respect to their standard deviations). Absolute changes (non-normalized) in anisotropy at beginning and end of dry season are presented in Figure 5.6. Only those changes that exceeded the RMSE of the field validation (Figure 5.2a and 5.2b) are presented. Non-forested areas were excluded from all analysis using the MODIS land cover product (collection 5, Friedl et al., 2010).

Figure 5.5a uses a fixed dry season assumption from June through September to derive conventional measures of greening/browning. Figure 5.5b shows changes of greening/browning based on onset and length of dry season derived from water deficit. In both cases, the drought years of 2005 and 2010 were excluded from the analyses to reflect “normal year” situations. In case of the fixed dry season assumption (Figure 5.5a), negative net changes in anisotropy were found largely in the west and north-western region of the Amazon basin, while small greening effects were observed in the Amapá state region and south-central Amazonia. When considering the specific length of dry season (Figure 5.5b), it becomes apparent that most of the area showing net

browning effects did actually not experience a seasonal water deficit (Figure 5.5a), at least on average within the time period observed.

Net greening effects shown in Figure 5.5b were similar to those presented in Figure 5.5a. However, regionally, considerable differences were found, particularly in the south western part of the study area. Compared to the normalized results, non-normalized differences in anisotropy between the beginning and end of dry season were prominent across most of the Amazon basin (Figures 5.6a and 5.6b), which can be explained by the relatively small RMSE obtained from the validation dataset (Figure 5.2a and 5.2b).

Figures 5.5c and 5.5d show net greening and browning effects in percentage of total area per month of dry season. Greening and browning effects were defined as percentage of pixels with significant increase / decrease in anisotropy ($\geq 2\sigma$) compared to the annual mean. Figures 5.5c uses a fixed dry season assumption (June through September), while Figure 5.5d shows changes based on onset of dry season derived from water deficit. In case of Figure 5.5d, we also show the last month before a water deficit was observed, in order to illustrate changes in photosynthetic activity with the reduction of rainfall towards the end of the rainy season. Both estimates showed increased anisotropy during the beginning of the dry season with about 2% of area experiencing “greening” when using a fixed dry season assumption and over 5% of total area greening when explicitly considering dry season onset for each pixel.

In both analyses, greening effects turned into net browning effects after an extended length of dry season, reaching about 7% of the area after 3 or more months when accounting for actual dry season onset. Monthly changes in LAI (as deviations from annual means) were calculated using the linear relationships to field and LiDAR measurements presented in Figure 5.2. The dashed line in Figures 5.5c and 5.5d represent estimates based on the relationship with field observations (Figure 5.2a), while the solid line represents estimates based on the relationship with LiDAR observations (Figure 5.2b). Consistent with the net changes in area of greening and browning, our results suggested that total leaf area increases during the beginning of the

dry season by on average $0.2 \text{ m}^2 \text{ m}^{-2}$ across the basin, while LAI dropped below the annual mean after about 2 months of dry season ($0.1 \text{ m}^2 \text{ m}^{-2}$). However, these results should be interpreted carefully as changes in LAI varied greatly across space and may also be the result of changes in other structural parameters (see discussion).

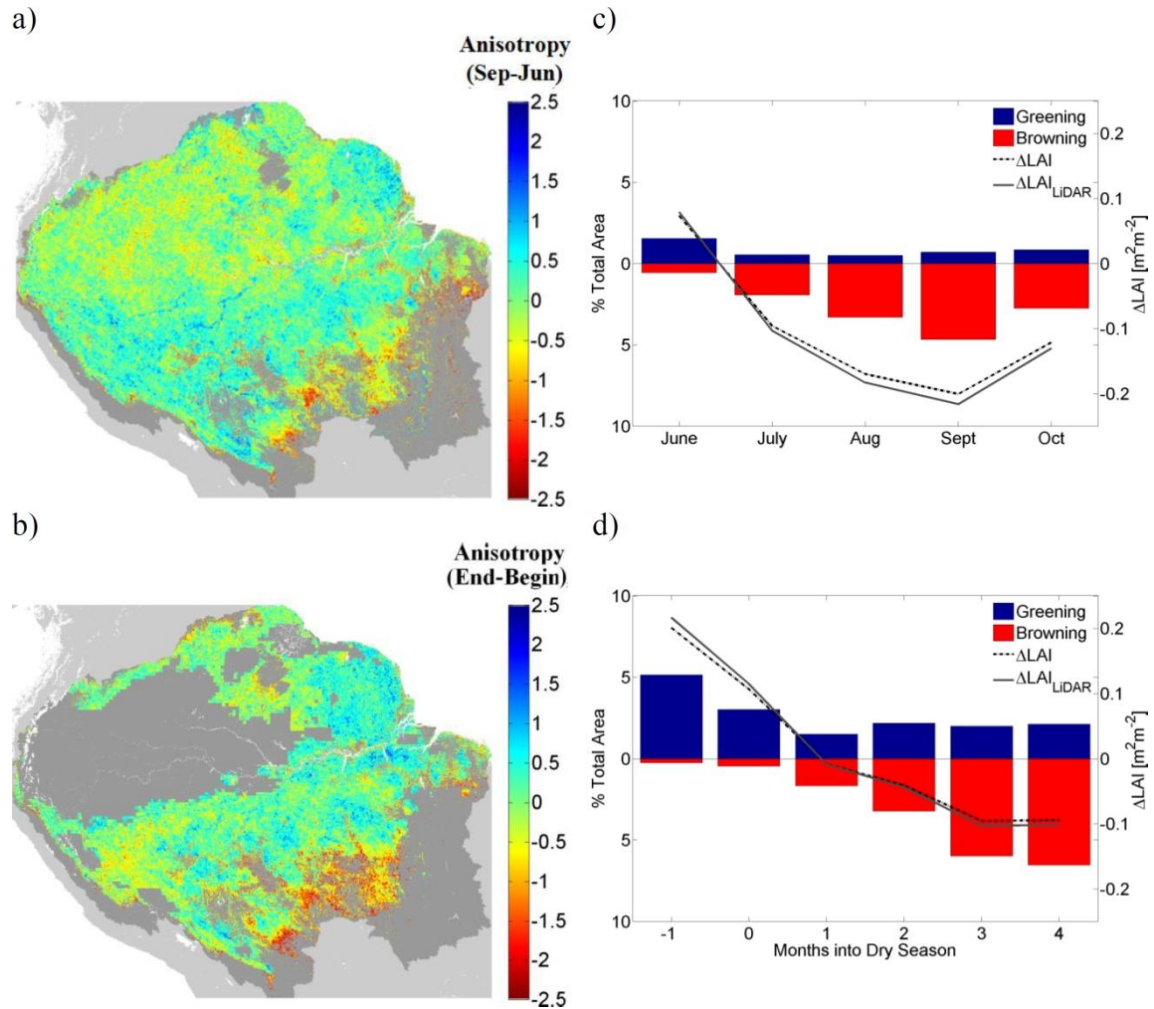


Figure 5.5. (a) Spatial distribution of changes in anisotropy normalized by the standard deviation using a dry season period from June to September (for all years between 2000 and 2012, except 2005 and 2010). The gray regions represents no dry season or non-forested areas. (b) Spatial distribution of changes in anisotropy normalized by the standard deviation using specific begin and end of dry season based on the water deficit maps. Figures c and d show the corresponding changes in greening (blue bars) and browning (red bars) by months of dry season ($p = 0.05$). The dashed lines in Figures c and d represent the net changes in LAI

(averaged across the basin) modelled by the linear relationship between anisotropy and LAI (Figure 5.2a). The solid line shows the corresponding estimates based on the model derived from LiDAR (Figure 5.2b).

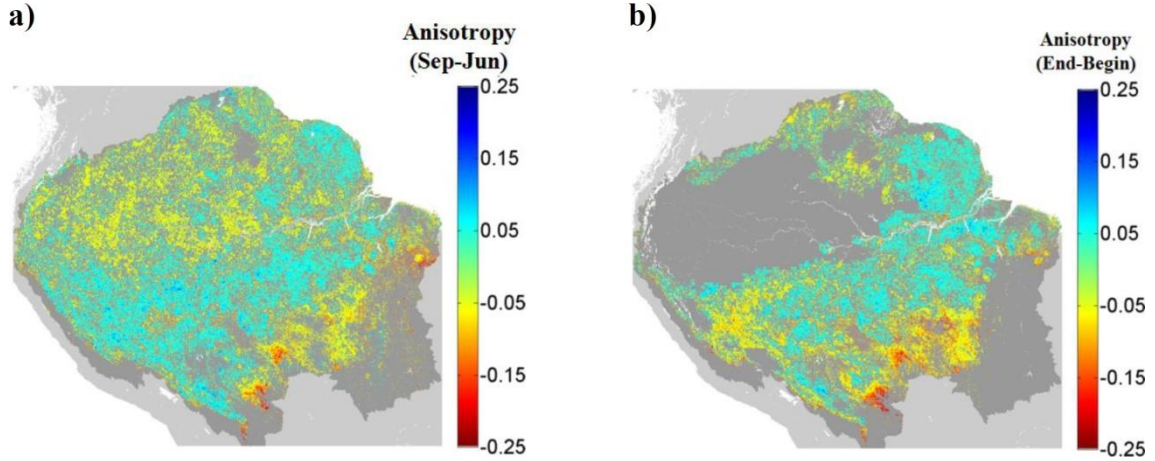


Figure 5.6. (a) Spatial distribution of changes in non-normalized anisotropy normalized using a dry season period from June to October (for all years, except 2005 and 2010). The gray regions represents no dry season or non-forested areas. (b) Spatial distribution of changes in non-normalized anisotropy using specific begin and end of dry season based on the water deficit maps.

The two drought years resulted in strong browning effects; spatial and temporal patterns of anomalies in anisotropy for the 2005 and 2010 droughts are presented in Figure 5.7. For both years, only the specific beginning and end of the dry season (based on the water deficit) are shown. Figure 5.7 shows anomalies i.e. deviations from the normal year patterns presented in Figure 5.5; all anomalies were normalized to the standard deviation ($\geq 2\sigma$) of the years 2000-2012, excluding 2005 and 2010. While positive and negative anomalies were approximately balanced at the beginning of the dry season (Figures 5.7c and 5.7d), negative anomalies in anisotropy outweighed positive effects after about three months, especially during 2010, with negative anomalies being three times larger than positive ones. Estimates of derived LAI showed small positive anomalies during the beginning of the 2005 drought period, but confirmed large negative effects with extended dry season length. In 2010, change was similar to normal years (anomalies were small) during the first few months of the dry season. However,

areas with 6 months of dry season showed negative deviation from normal year decline in structure (Figure 5.7d) of an additional $-0.2 \text{ m}^2 \text{ m}^{-2}$ across the basin (Figure 5.7d).

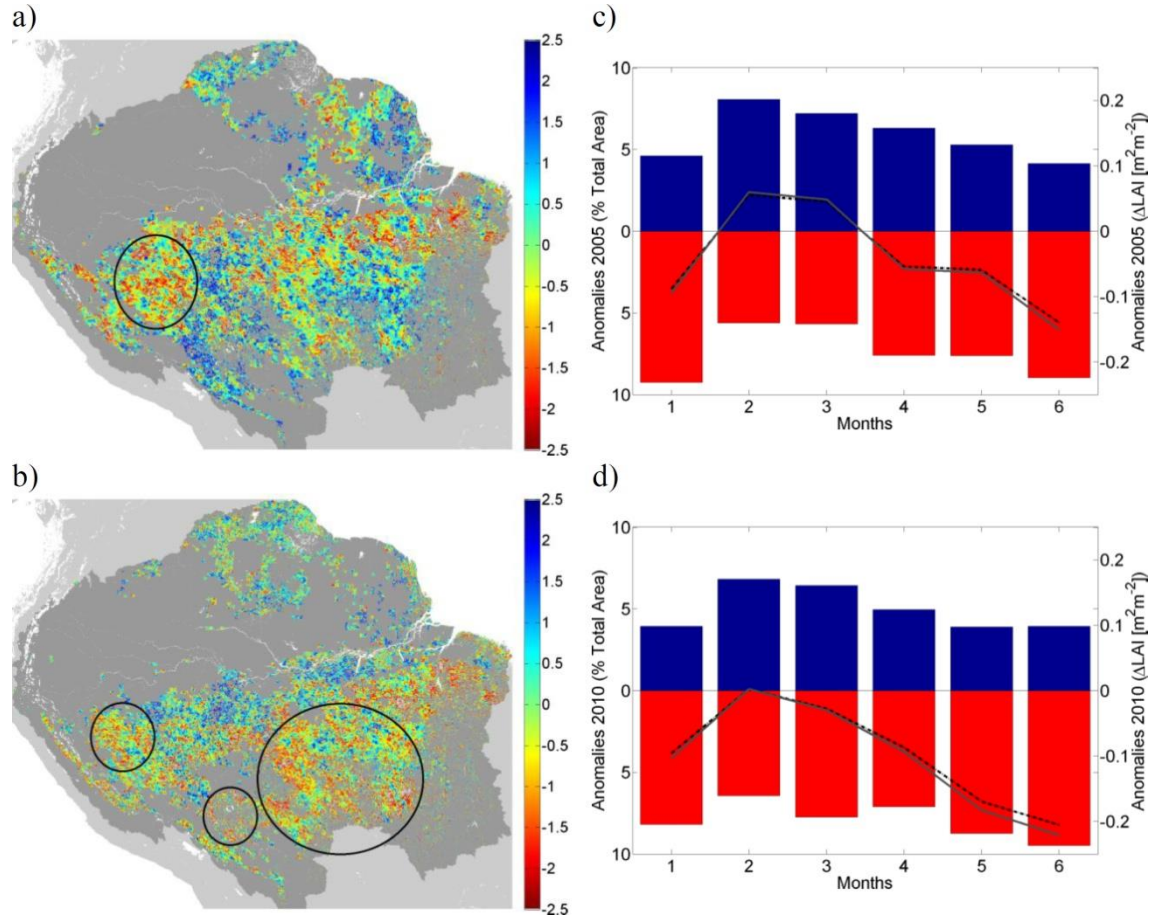


Figure 5.7. Spatial distribution of the standardized anomalies in anisotropy for 2005 (a) and 2010 (b), considering specifically begin and end of dry season (based on the water deficit maps). The gray regions represents no dry season or non-forested areas. Figures c and d show the corresponding anomalies in greening (blue bars) and browning (red bars) by months into dry season ($p = 0.05$). Circles represents an approximation of the epicenters of the droughts described by Lewis et al. (2011). The dashed lines in Figures c and d represent the anomalies in LAI (averaged across the basin) modelled by the linear relationship between anisotropy and LAI (Figure 5.2a). The solid line shows the corresponding estimates based on the model derived from LiDAR (Figure 5.2b).

5.4. Discussion

This study used multi-angle observations from the MODIS instrument to investigate spatial and temporal variability in vegetation structure across the Amazon basin. The ability of multi-angle observation to derive vegetation structural attributes is well supported by previous studies of temperate ecosystems (CHEN et al., 2003; GAO, 2003b). Multi-angle data decrease the dispersion and saturation in geometrically complex canopies (ZHANG et al., 2002) and are therefore better suited to describe the three dimensional structure of forests compared to mono-angle acquisitions (CHEN; LEBLANC, 1997; STRAHLER; JUPP, 1990).

Our strong linear relationship found between anisotropy and LAI estimates (Figure 5.2a and 5.2b, $r^2=0.70$, $r^2=0.88$ $p<0.05$, respectively) confirms these findings. The RMSE for the relationships between anisotropy and field observations has allowed us to link seasonal changes in anisotropy with changes in vegetation structure. However, we do acknowledge that other structural variables can influence seasonal patterns of anisotropy in different ways. For instance, anisotropy is also affected by canopy roughness (STRAHLER, 2009a), leaf angle distribution (ROUJEAN, 2002) and foliage clumping (CHEN et al., 2005). Furthermore, the selected approach of modeling LAI from LiDAR depends, to some extent, on footprint size and point density. While the technique utilized here has been validated elsewhere (COOPS et al., 2007; LOVELL et al., 2003), differences in ecosystem types and LiDAR configuration may affect LAI estimates. As a result, the findings presented with respect to changes in leaf area should be interpreted with care and should be understood more as an example of how anisotropy may be linked to structural variables. Nonetheless, the linear functional form suggests that multi-angle observations may provide an opportunity to address current limitations caused by saturation of conventional (nadir) vegetation indices (HUETE et al., 2006b; KNYAZIKHIN et al., 1998) at least within the range of observed LAI ($\leq 7 \text{ m}^2 \text{ m}^{-2}$). Our results suggest that structural information of vegetation may be obtained frequently over large areas from MODIS. Further research, however, will be needed to investigate potentials for other ecosystems and regions.

While mono-angle observations have been shown to indicate levels of vegetation greenness, they are less well suited to describe the three-dimensional structure of forest canopies (CHEN; LEBLANC, 1997; STRAHLER; JUPP, 1990). The selected approach using anisotropy may provide new insights into structural variability of Amazon forests as it increases the sensitivity of optical observations to changes across dense vegetation types. This should considerably improve our understanding of Amazon forest seasonality and drought tolerance. The findings presented in Figures 5.3 and 5.4 suggest that rainfall patterns in Amazonian forests varied greatly, causing differences in seasonality across the region.

Estimates of water deficit (Figure 5.4a and 5.4b), followed a south-west north-east gradient with up to 5 months of water deficit in the south-west whereas large areas of Amazonas state showed, on average, no water deficit during the observed years (compare Steege; Pitman, 2003). Previous research has suggested that vegetation seasonality may follow this gradient closely, as higher precipitation support higher leaf areas in the wetter regions, while vegetation in drier areas is limited by available soil water (MYNENI et al., 2007). Water availability may further contribute to changes in the spatial distribution of leaves (GUAN et al., 2015; MALHADO; COSTA, 2009; SCHURR et al., 2012; TER STEEGE et al., 2006; WAGNER et al., 2013). Also, the length of dry season has been shown to correlate with aboveground live biomass (Saatchi et al., 2007) and tree species composition (TER STEEGE et al., 2006; WAGNER et al., 2014).

Estimating vegetation seasonality from water deficit provided a simple but effective approach to capture this regional variability in precipitation. Other approaches, for example, based on available photosynthetically active radiation (PAR) are possible and may result in different definition of dry and wet season. While our findings are in good agreement with previous reports (STEEGE; PITMAN, 2003), it should be noted that in the northern part of the Amazon, cloud cover is considerably higher than in the south, which may increase measurement noise in the TRMM data and contribute to larger spatial variation in onset and length of dry season observed.

The findings provided in Figures 5.1, 5.5 and 5.6 suggest large spatial and seasonal variability of Amazonian forests. This result relates well to previous studies on vegetation structure and seasonality of the Amazon (TER STEEGE et al., 2006; VILLAR et al., 2009) as well as estimates of aboveground carbon (SAATCHI et al., 2011). Consideration of this variability will be critical for interpreting the biophysical responses of vegetation to changes in climate.

The results presented in Figures 5.5, 5.6 and 5.7 confirm seasonal swings in the Amazon (MYNENI et al., 2007). While the total area with significant change (Figure 5.5) is relatively small compared to that observed in the Myneni et al. (2007), these variations can be explained by the difference in methods applied. First, Myneni et al., (2007) used the RMSE of the relationship to field observations to determine whether a change is significant or not, but did not normalize by the standard deviation. Our results in Figure 5.6 showed much increase seasonality when using the RMSE of field and LiDAR data (Figure 5.2a and 5.2b) to determine significance. Also, Myneni et al., (2007) calculated seasonality as the difference between the maximum 4-month average LAI in the dry season minus the minimum 4-month average LAI in the wet season for those regions with dry seasons longer than 3 months. For all other regions, they calculated seasonality as the difference between the dry-season average LAI and the minimum 4-month average LAI in the wet season.

The seasonality in anisotropy (Figure 5.1, Figure 5.5) cannot be explained by directional effects, as all observations have been normalized to a fixed forward and backscatter geometry (LYAPUSTIN et al., 2012a). Opposite findings based on conventional MODIS data (MORTON et al., 2014) will require further analysis to be addressed separately. One possible explanation might be noise in the dataset (HILKER et al., 2012b) rendering residual changes below a statistical significance level. Changes in anisotropy (greening/browning) during the dry season (Figures 5.5, 5.6 and 5.7) coincided well with previous reports on Amazon seasonality. The results support the view that photosynthetic activity initially increases during the dry season in response to an increase in incident PAR (BRANDO et al., 2010; GRAHAM et al., 2003; HUETE et al., 2006b; HUTYRA et al., 2007; MALHI et al., 2009; MYNENI et al., 2007;

SAMANTA et al., 2012a; WAGNER et al., 2013) while water supply is maintained through deep root systems of tropical forests (NEPSTAD et al., 1994). Consistent to these findings, Figures 5.7c and 5.7d showed an initial increase and then a decline in anisotropy after extended drought periods.

While the fixed dry season assumption resulted in less clear trends, particularly with respect to area greening, the spatially explicit estimates of dry season onset and dry season length showed clear greening during the dry season onset. On the other hand, after an extended length of the dry season, this effect turned into net browning across areas that experienced 3 or more months of dry season in a given year. The spatial and temporal patterns of anomalies in anisotropy for the 2005 and 2010 droughts (Figure 5.7) allow the conclusions that although productivity of tropical vegetation may increase initially during the dry season (BRANDO et al., 2010; GRAHAM et al., 2003; HUETE et al., 2006b), sustained drought reduces photosynthesis, canopy leaf area and ultimately causes tree mortality (BRANDO et al., 2008; DOUGHTY et al., 2015; PHILLIPS et al., 2009; SALESKA et al., 2007a). This is an important result as it helps reconcile findings from field and modeling studies with remote sensing observations - a key requirement for improving our understanding of drought behavior and quantifying carbon dynamics across vegetation and moisture gradients in Amazonia (BAKER et al., 2008).

During both drought events (Figures 5.7c and 5.7d), positive and negative anomalies were roughly balanced at the beginning of the dry season, indicating an expected natural variability in one year compared to the mean of all other years. However, browning effects became increasingly prominent, especially during 2010, where the size of areas with negative anomalies was almost three times larger than areas with greening. These strong anomalies may be explained by more intense water deficits causing faster depletion of available water supply and an extended duration of the dry season resulting in prolonged stress events. The spatial patterns presented for the two extensive droughts in the Amazon region were roughly in agreement with the regions of high drought intensity described in Lewis et al., 2011, with a concentration in the southwest for 2005, and more widespread effects in 2010 throughout the southeast. Our findings relate well

also to plot and LiDAR-based studies, which showed that forest structure and density can be strongly affected by extreme droughts with significant reduction of forest productivity and aboveground biomass over time (PHILLIPS et al., 2009; SAATCHI et al., 2013).

5.5. Conclusions

The findings presented in this study contribute to the recent debate on Amazon seasonality and drought tolerance in three major ways. First, we have demonstrated, using reflectance anisotropy obtained from multi-angle MODIS observations that Amazonian forests expose a large heterogeneity both spatially and seasonally and this heterogeneity is related to differences in vegetation structure. The demonstrated approach using anisotropy may allow us to better detect and quantify these changes even in densely vegetated areas typical for tropical ecosystems. Second, our analysis has shown that quantification of seasonal changes in vegetation depends on the definition of onset and duration of the dry season. This conclusion underlines the need for explicit consideration of temporal differences, as the assumption of a fixed period of dry season may lead to erroneous conclusions about phenological cycles in Amazonian forests. Finally, our analysis reconciles remote sensing studies with field based observations and model results as it provides a sounder basis for the argument that tropical vegetation undergoes strong seasonal effects, leading to increased growth during the beginning of the dry season, but to vegetation decline after extended drought periods, particularly during the 2005 and 2010 extreme events.

6 SUMMARY AND FINAL REMARKS

Comprehensive assessments of forest structure are key elements to improving our understanding of vegetation seasonality, and the effects of drought and climate change on tropical ecosystems. This thesis has demonstrated the potential of multi-angle MODIS data for mapping structural characteristics of vegetation and its changes over time. Reflectance anisotropy, here defined as difference between backscattering and forward scatter remote sensing observations, was successfully related to vegetation leaf area and surface roughness, something that has previously been difficult to accomplish from mono-angle observations. While the concept of anisotropy is not new, this is the first time it has been applied across large areas using the MODIS satellite. A key improvement that allowed us to apply this technique was the Multi-Angle implementation of Atmospheric Correction Algorithm (MAIAC). MAIAC maintains anisotropic characteristics of MODIS reflectance, while providing improved quality and observations frequency. Validation of MODIS derived estimates was based on field, LiDAR and Radar observations. While limited in their spatial extent, LAI estimates from airborne and spaceborne platforms showed promising relationships especially when compared to conventional vegetation indices. Complementary measures of vegetation structure from optical satellites are desirable to extrapolate spatially or temporally sparse estimates of canopy structure across the landscape. Previous studies have shown controversial results when using satellite data and field-based estimates, regarding the response of tropical forests to extreme drought events, as well as, forest seasonality. Our findings support the hypothesis of increased productivity at the beginning of the dry season, but a decrease in the productivity of the Amazonian forests during extended droughts. As a result of the structural relationships presented, the multi-angle approach presented in this thesis may help resolve some of these controversies and provide a valuable scaling tool for upcoming missions on vegetation structure. In combination with LiDAR estimates of forest structure, multi-angle data may contribute to discriminate structural variation in different types of forests across the Amazon, as well as to quantify the impact of land use and land cover changes on the terrestrial carbon cycle.

REFERENCES

- ANDERSON, L. O. **Multitemporal analysis of evergreen forest dynamics in Amazonia**. (Doctoral dissertation, Oxford University), 2010.
- ANDERSON, L. O. Biome-Scale Forest Properties in Amazonia Based on Field and Satellite Observations. **Remote Sensing**, v. 4, n. 12, p. 1245–1271, 4 maio 2012.
- ANDREAE, M. O. Biogeochemical cycling of carbon, water, energy, trace gases, and aerosols in Amazonia: The LBA-EUSTACH experiments. **Journal of Geophysical Research**, v. 107, n. D20, p. 8066, 2002.
- ARAGÃO, L. E. O. C. et al. Above- and below-ground net primary productivity across ten Amazonian forests on contrasting soils. **Biogeosciences**, v. 6, n. 12, p. 2759–2778, 1 dez. 2009.
- ARAGAO, L. E. O. C.; LIANA O., S. M. Y. C. R. M. R. S. S. A.; EDEMIR, Y. Spatial patterns and fire response of recent Amazonian droughts. **Geophysical Research Letters**, v. 34, p. 1–5, 2007.
- ASNER, G. P. et al. Ecological research needs from multiangle remote sensing data. **Remote Sensing of Environment**, v. 63, n. 2, p. 155–165, fev. 1998.
- ASNER, G. P. et al. **Drought stress and carbon uptake in an Amazon forest measured with spaceborne imaging spectroscopy**. Proceedings of the National Academy of Sciences of the United States of America, v. 101, n. 16, p. 6039-6044, 2004.
- ASNER, G. P.; ALENCAR, A. Drought impacts on the Amazon forest: the remote sensing perspective. **The New phytologist**, v. 187, n. 3, p. 569–78, ago. 2010.
- ATKINSON, P. M.; DASH, J.; JEGANATHAN, C. Amazon vegetation greenness as measured by satellite sensors over the last decade. **Geophysical Research Letters**, v. 38, n. 19, p. n/a–n/a, 12 out. 2011.
- BAKER, I. T. et al. Seasonal drought stress in the Amazon: reconciling models and observations. **Journal of Geophysical Research**, v. 113, p. G00B01, jul. 2008.
- BARNESLEY, M. J. et al. The PROBA/CHRIS mission: a low-cost smallsat for hyperspectral multiangle observations of the Earth surface and atmosphere. **IEEE Transactions on Geoscience and Remote Sensing**, v. 42, n. 7, p. 1512–1520, jul. 2004a.
- BARNESLEY, M. J. et al. The PROBA/CHRIS mission: a low-cost smallsat for hyperspectral multiangle observations of the Earth surface and atmosphere. **IEEE**

Transactions on Geoscience and Remote Sensing, v. 42, n. 7, p. 1512–1520, 1 jul. 2004b.

BASTIAANSEN, W. G. M. et al. A remote sensing surface energy balance algorithm for land (SEBAL). 1. Formulation. **Journal of Hydrology**, v. 212-213, p. 198–212, dez. 1998.

BHANDARI, S.; PHINN, S.; GILL, T. Assessing viewing and illumination geometry effects on the MODIS vegetation index (MOD13Q1) time series: implications for monitoring phenology and disturbances in forest communities in Queensland, Australia. **International Journal of Remote Sensing**, v. 32, n. 22, p. 7513–7538, 20 nov. 2011.

BI, J. et al. Sunlight mediated seasonality in canopy structure and photosynthetic activity of Amazonian rainforests. **Environmental Research Letters**, v. 10, n. 6, p. 064014, 1 jun. 2015.

BICHERON, P. A Method of Biophysical Parameter Retrieval at Global Scale by Inversion of a Vegetation Reflectance Model. **Remote Sensing of Environment**, v. 67, n. 3, p. 251–266, mar. 1999.

BORCHERT, R. Responses of tropical trees to rainfall seasonality and its long-term changes. In: **Potential Impacts of Climate Change on Tropical Forest Ecosystems**. Springer Netherlands, 1998. p. 241-253.

BOUDREAU, J. et al. Regional aboveground forest biomass using airborne and spaceborne LiDAR in Québec. **Remote Sensing of Environment**, v. 112, n. 10, p. 3876–3890, 15 out. 2008.

BRANDO, P. M. et al. Drought effects on litterfall, wood production and belowground carbon cycling in an Amazon forest: results of a throughfall reduction experiment. **Philosophical transactions of the Royal Society of London. Series B, Biological sciences**, v. 363, n. 1498, p. 1839–48, maio 2008.

BRANDO, P. M. et al. Seasonal and interannual variability of climate and vegetation indices across the Amazon. **Proceedings of the National Academy of Sciences of the United States of America**, v. 107, n. 33, p. 14685–90, 17 ago. 2010.

BREUNIG, F. M. et al. Spectral anisotropy of subtropical deciduous forest using MISR and MODIS data acquired under large seasonal variation in solar zenith angle. **International Journal of Applied Earth Observation and Geoinformation**, v. 35, p. 294–304, mar. 2015.

CARLSON, T. N.; RIPLEY, D. A. On the relation between NDVI, fractional vegetation cover, and leaf area index. **Remote Sensing of Environment**, v. 62, n. 3, p. 241–252, dez. 1997.

CHAPIN, F. I.; MATSON, P.; VITOUSEK, P. **Principles of terrestrial ecosystem ecology**. Springer Science & Business Media, 2011.

CHEN, J. M. et al. Multi-angular optical remote sensing for assessing vegetation structure and carbon absorption. **Remote Sensing of Environment**, v. 84, n. 4, p. 516–525, abr. 2003.

CHEN, J. M.; LEBLANC, S. G. A four-scale bidirectional reflectance model based on canopy architecture. **IEEE Transactions on Geoscience and Remote Sensing**, v. 35, n. 5, p. 1316–1337, 1997.

CHEN, J. M.; MENGES, C. H.; LEBLANC, S. G. Global mapping of foliage clumping index using multi-angular satellite data. **Remote Sensing of Environment**, v. 97, n. 4, p. 447–457, set. 2005.

CHEN, J. M., LIUB, J., LEBLANC, S. G., LACAZEC, R., ROUJEAN, J. L. **Multi-angular optical remote sensing for assessing vegetation structure and carbon absorption**. v. 84, n. 4, p. 516-525, 2003.

CHOPPING, M. et al. Forest structure and aboveground biomass in the southwestern United States from MODIS and MISR. **Remote Sensing of Environment**, v. 115, n. 11, p. 2943–2953, nov. 2011.

COOPS, N. C. et al. Estimating canopy structure of Douglas-fir forest stands from discrete-return LiDAR. **Trees**, v. 21, n. 3, p. 295–310, jan. 2007.

DINER, D. J. et al. Multi-angle Imaging SpectroRadiometer (MISR) instrument description and experiment overview. **IEEE Transactions on Geoscience and Remote Sensing**, v. 36, n. 4, p. 1072–1087, 1 jul. 1998.

DISNEY, M.; LEWIS, P.; SAICH, P. 3D modelling of forest canopy structure for remote sensing simulations in the optical and microwave domains. **Remote Sensing of Environment**, v. 100, n. 1, p. 114–132, jan. 2006.

DOMINGUES, T. F. et al. Parameterization of Canopy Structure and Leaf-Level Gas Exchange for an Eastern Amazonian Tropical Rain Forest (Tapajós National Forest, Pará, Brazil). **Earth Interactions**, v. 9, n. 17, p. 1–23, out. 2005.

DOUGHTY, C. E. et al. Drought impact on forest carbon dynamics and fluxes in Amazonia. **Nature**, v. 519, n. 7541, p. 78–82, 4 mar. 2015.

DOUGHTY, C. E.; GOULDEN, M. L. Seasonal patterns of tropical forest leaf area index and CO₂ exchange. **Journal of Geophysical Research**, v. 113, p. G00B06, 14 out. 2008.

DUBAYAH, R. et al. The global ecosystem dynamics investigation. **American Geophysical Union**, 2014.

FIGUERA, A. M. S. et al. **LBA-ECO CD-04 Leaf Area Index, km 83 Tower Site, Tapajos National Forest, Brazil**. Data set. Available on-line [<http://daac.ornl.gov>] from Oak Ridge National Laboratory Distributed Active Archive Center, Oak Ridge, Tennessee, U.S.A., 2011.

FRANCH, B. et al. Analysis of directional effects on atmospheric correction. **Remote Sensing of Environment**, v. 128, p. 276–288, jan. 2013.

FRIEDL, M. A. et al. MODIS Collection 5 global land cover: Algorithm refinements and characterization of new datasets. **Remote Sensing of Environment**, v. 114, n. 1, p. 168–182, jan. 2010.

FROLKING, S. et al. Evaluation of the Sea Winds scatterometer for regional monitoring of vegetation phenology. **Journal of Geophysical Research: Atmospheres**, v. 111, n. 17, p. 1–14, 2006.

FROLKING, S. et al. Tropical forest backscatter anomaly evident in SeaWinds scatterometer morning overpass data during 2005 drought in Amazonia. **Remote Sensing of Environment**, v. 115, n. 3, p. 897–907, mar. 2011.

FU, R. et al. Increased dry-season length over southern Amazonia in recent decades and its implication for future climate projection. **Proceedings of the National Academy of Sciences of the United States of America**, v. 110, n. 45, 2013.

GALVAO, L. S. et al. On intra-annual EVI variability in the dry season of tropical forest: A case study with MODIS and hyperspectral data. **Remote Sensing of Environment**, v. 115, n. 9, p. 2350–2359, set. 2011.

GALVAO, L. S. et al. View-illumination effects on hyperspectral vegetation indices in the Amazonian tropical forest. **International Journal of Applied Earth Observation and Geoinformation**, v. 21, n. 1, p. 291–300, abr. 2012.

GALVÃO, L. S. et al. View-illumination effects on hyperspectral vegetation indices in the Amazonian tropical forest. **International Journal of Applied Earth Observation and Geoinformation**, v. 21, p. 291–300, abr. 2013.

GAO, B.-C. Water vapor retrievals using Moderate Resolution Imaging Spectroradiometer (MODIS) near-infrared channels. **Journal of Geophysical Research**, v. 108, n. D13, p. 4389, 2003a.

GAO, F. Detecting vegetation structure using a kernel-based BRDF model. **Remote Sensing of Environment**, v. 86, n. 2, p. 198–205, 30 jul. 2003b.

- GATTI, L. V et al. Drought sensitivity of Amazonian carbon balance revealed by atmospheric measurements. **Nature**, v. 506, n. 7486, p. 76–80, 6 fev. 2014.
- GLENN, E. P. et al. Relationship Between Remotely-sensed Vegetation Indices, Canopy Attributes and Plant Physiological Processes: What Vegetation Indices Can and Cannot Tell Us About the Landscape. **Sensors**, v. 8, n. 4, p. 2136–2160, mar. 2008.
- GOEL, N. S. Models of vegetation canopy reflectance and their use in estimation of biophysical parameters from reflectance data. **Remote Sensing Reviews**, v. 4, n. 1, p. 1–212, 19 jan. 1988.
- GONÇALVES, F. G. **Vertical structure and aboveground biomass of tropical forests from lidar remote sensing**, 23 jan. 2016. Disponível em: <<http://ir.library.oregonstate.edu/raja/torrent.com/xmlui/handle/1957/54938>>. Acesso em: 29 set. 2015
- GRAHAM, E. A et al. Cloud cover limits net CO₂ uptake and growth of a rainforest tree during tropical rainy seasons. **Proceedings of the National Academy of Sciences of the United States of America**, v. 100, n. 2, p. 572–6, jan. 2003.
- GUAN, K. et al. Photosynthetic seasonality of global tropical forests constrained by hydroclimate. **Nature Geoscience**, v. advance on, 9 mar. 2015.
- HAPKE, B.; NELSON, R.; SMYTHE, W. The Opposition Effect of the Moon: Coherent Backscatter and Shadow Hiding. **Icarus**, v. 133, n. 1, p. 89–97, maio 1998.
- HARDING, D. J. ICESat waveform measurements of within-footprint topographic relief and vegetation vertical structure. **Geophysical Research Letters**, v. 32, n. 21, p. L21S10, 2005.
- HEALEY, S. P. et al. A sample design for globally consistent biomass estimation using lidar data from the Geoscience Laser Altimeter System (GLAS). **Carbon balance and management**, v. 7, n. 1, p. 10, 2012a.
- HEALEY, S. P. et al. A sample design for globally consistent biomass estimation using lidar data from the Geoscience Laser Altimeter System (GLAS). **Carbon balance and management**, v. 7, n. 1, p. 10, 2012b.
- HILKER, T. et al. A new data fusion model for high spatial- and temporal-resolution mapping of forest disturbance based on Landsat and MODIS. **Remote Sensing of Environment**, v. 113, n. 8, p. 1613–1627, ago. 2009.
- HILKER, T. et al. Comparing canopy metrics derived from terrestrial and airborne laser scanning in a Douglas-fir dominated forest stand. **Trees**, v. 24, n. 5, p. 819–832, jun. 2010.

HILKER, T. et al. Comparison of Terrestrial and Airborne LiDAR in Describing Stand Structure of a. **Journal of Forestry**, n. March, p. 97–104, 2012a.

HILKER, T. et al. Remote sensing of tropical ecosystems: Atmospheric correction and cloud masking matter. **Remote Sensing of Environment**, v. 127, p. 370–384, dez. 2012b.

HILKER, T. et al. Vegetation dynamics and rainfall sensitivity of the Amazon. **Proceedings of the National Academy of Sciences**, v. 111, n. 45, p. 16041–16046, out. 2014.

HILKER, T. et al. On the measurability of change in Amazon vegetation from MODIS. **Remote Sensing of Environment**, v. 166, p. 233–242, jun. 2015a.

HILKER, T. et al. On the measurability of change in Amazon vegetation from MODIS. **Remote Sensing of Environment**, v. 166, p. 233–242, jun. 2015b.

HSU, N. C. et al. Aerosol Properties Over Bright-Reflecting Source Regions. **IEEE Transactions on Geoscience and Remote Sensing**, v. 42, n. 3, p. 557–569, mar. 2004.

HU, J. et al. Performance of the MISR LAI and FPAR algorithm: a case study in Africa. **Remote Sensing of Environment**, v. 88, n. 3, p. 324–340, dez. 2003.

HUETE, A. et al. Overview of the radiometric and biophysical performance of the MODIS vegetation indices. **Remote Sensing of Environment**, v. 83, n. 1-2, p. 195–213, 2002.

HUETE, A.; JUSTICE, C.; LIU, H. Development of vegetation and soil indices for MODIS-EOS. **Remote Sensing of Environment**, v. 49, n. 3, p. 224–234, set. 1994.

HUETE, A. R. et al. Amazon rainforests green-up with sunlight in dry season. **Geophysical Research Letters**, v. 33, n. 6, p. L06405, 2006a.

HUETE, A. R. et al. Amazon rainforests green-up with sunlight in dry season. **Geophysical Research Letters**, v. 33, n. 6, p. L06405, 2006b.

HUTYRA, L. R. et al. Seasonal controls on the exchange of carbon and water in an Amazonian rain forest. **Journal of Geophysical Research**, v. 112, n. G3, p. G03008, ago. 2007.

BRAZIL, IBGE. **Manual Técnico da Vegetação Brasileira**. Manuais Técnicos em Geociências, n. 1, 1992.

JACQUEMOUD, S.; BARET, F.; HANOCQ, J. F. Modeling spectral and bidirectional soil reflectance. **Remote Sensing of Environment**, v. 41, n. 2-3, p. 123–132, ago. 1992.

JUSTICE, C. O. et al. The Moderate Resolution Imaging Spectroradiometer (MODIS): land remote sensing for global change research. **IEEE Transactions on Geoscience and Remote Sensing**, v. 36, n. 4, p. 1228–1249, jul. 1998a.

JUSTICE, C. O. et al. The Moderate Resolution Imaging Spectroradiometer (MODIS): land remote sensing for global change research. **IEEE Transactions on Geoscience and Remote Sensing**, v. 36, n. 4, p. 1228–1249, jul. 1998b.

KAUFMAN, Y. J. et al. The MODIS 2.1- μm channel-correlation with visible reflectance for use in remote sensing of aerosol. **IEEE Transactions on Geoscience and Remote Sensing**, v. 35, n. 5, p. 1286–1298, 1997.

KAUFMANN, R. K. et al. Effect of orbital drift and sensor changes on the time series of AVHRR vegetation index data. **IEEE Transactions on Geoscience and Remote Sensing**, v. 38, n. 6, p. 2584–2597, 2000.

KEMPENEERS, P. et al. Model inversion for chlorophyll estimation in open canopies from hyperspectral imagery. **International Journal of Remote Sensing**, v. 29, n. 17–18, p. 5093–5111, set. 2008.

KING, M. D.; GREENSTONE, R. **1999 EOS reference handbook: a guide to NASA's Earth Science Enterprise and the Earth Observing System**. 1999 EOS reference handbook: a guide to NASA's Earth Science Enterprise and the Earth Observing System, by King, Michael D.; Greenstone, Reynold. Greenbelt, Md.: NASA/Goddard Space Flight Center, [1999], v. 1, 1999.

KNORR, W. et al. **Combining remote sensing techniques with productivity models: a case study for monitoring carbon stocks in northern European forests**. [s.l.] OECD Publications, 2004.

KNYAZIKHIN, Y. et al. Estimation of vegetation canopy leaf area index and fraction of absorbed photosynthetically active radiation from atmosphere-corrected MISR data. **Journal of Geophysical Research**, v. 103, n. D24, p. 32239, dez. 1998.

LAGOUARDE, J.-P. et al. Spatialization of sensible heat flux over a heterogeneous landscape. **Agronomie**, v. 22, n. 6, p. 627–633, set. 2002.

LEBLANC, S. G. et al. Canada-wide foliage clumping index mapping from multiangular POLDER measurements. **Canadian Journal of Remote Sensing**, v. 31, n. 5, p. 364–376, out. 2005.

LEFSKY, M. A. et al. Lidar Remote Sensing for Ecosystem Studies. **BioScience**, v. 52, n. 1, p. 19, 2002.

LEFSKY, M. A. et al. Estimates of forest canopy height and aboveground biomass using ICESat. **Geophysical Research Letters**, v. 32, n. 22, p. L22S02, 2005.

LEVY, R. C. et al. Second-generation operational algorithm: Retrieval of aerosol properties over land from inversion of Moderate Resolution Imaging Spectroradiometer spectral reflectance. **Journal of Geophysical Research: Atmospheres**, v. 112, n. D13, p. n/a–n/a, 16 jul. 2007.

LEWIS, S. L. et al. The 2010 Amazon drought. **Science (New York, N.Y.)**, v. 331, n. 6017, p. 554, 2011.

LI, X., STRAHLER, A. H. Geometric-Optical Bidirectional Reflectance Modeling of a Conifer Forest Canopy. **IEEE Transactions on Geoscience and Remote Sensing**, v. 24, n. 6, p. 906–919, 1986.

LIM, K. et al. LiDAR remote sensing of forest structure. **Progress in Physical Geography**, v. 27, n. 1, p. 88–106, mar. 2003a.

LIM, K. et al. LiDAR remote sensing of forest structure. **Progress in Physical Geography**, v. 27, n. 1, p. 88–106, 1 mar. 2003b.

LOS, S. O. et al. A method to convert AVHRR Normalized Difference Vegetation Index time series to a standard viewing and illumination geometry. **Remote Sensing of Environment**, v. 99, p. 400–411, 2005.

LOVELL, J. L. et al. Using airborne and ground-based ranging lidar to measure canopy structure in Australian forests. **Canadian Journal of Remote Sensing**, v. 29, n. 5, p. 607–622, out. 2003.

LYAPUSTIN, A. et al. Science impact of MODIS C5 calibration degradation and C6+ improvements. **Atmospheric Measurement Techniques Discussions**, v. 7, n. 7, p. 7281–7319, 2014.

LYAPUSTIN, A. et al. Multiangle implementation of atmospheric correction (MAIAC): 1. Radiative transfer basis and look-up tables. **Journal of Geophysical Research**, v. 116, n. D3, p. D03210, fev. 2011.

LYAPUSTIN, A. et al. Multi-Angle Implementation of Atmospheric Correction for MODIS (MAIAC). Part 3: Atmospheric Correction. **Remote Sensing of Environment**, v. 127, p. 385–393, 2012a.

LYAPUSTIN, A. I. Atmospheric and geometrical effects on land surface albedo. **Journal of Geophysical Research**, v. 104, n. D4, p. 4127, fev. 1999.

LYAPUSTIN, A. I. et al. Remote sensing of tropical ecosystems: Atmospheric correction and cloud masking matter. **Remote Sensing of Environment**, v. 127, p. 385–393, dez. 2012b.

LYAPUSTIN, A. I. et al. Multi-angle implementation of atmospheric correction for MODIS (MAIAC): 3. Atmospheric correction. **Remote Sensing of Environment**, v. 127, p. 385–393, dez. 2012c.

LYAPUSTIN, A. I.; MULDASHEV, T. Z. METHOD OF SPHERICAL HARMONICS IN THE RADIATIVE TRANSFER PROBLEM WITH NON-LAMBERTIAN SURFACE. **Journal of Quantitative Spectroscopy and Radiative Transfer**, v. 61, n. 4, p. 545–555, mar. 1999.

LYAPUSTIN, A.; KNYAZIKHIN, Y. Green's function method for the radiative transfer. **Applied Optics**, v. 40, n. 21, p. 3495–3501, 2001.

LYAPUSTIN, A.; WANG, Y.; FREY, R. An automatic cloud mask algorithm based on time series of MODIS measurements. **Journal of Geophysical Research**, v. 113, n. D16, p. D16207, ago. 2008.

LYAPUSTIN, A.I.; MARTONCHIK, J.; WANG, Y.; LASZLO, I.; KORKIN, S. Multiangle implementation of atmospheric correction (MAIAC): 1. radiative transfer basis and look-up tables. **Journal of Geophysical Research: Atmospheres**, v. 116, n. D3, 2011.

MAGNUSSEN, S.; BOUDEWYN, P. Derivations of stand heights from airborne laser scanner data with canopy-based quantile estimators. **Canadian Journal of Forest Research**, v. 28, n. 7, p. 1016-1031, 1998.

MAGNUSSON, M.; FRANSSON, J. E. S.; HOLMGREN, J. Effects on estimation accuracy of forest variables using different pulse density of laser data. **Forest science**, v. 53, n. 6, 619-626, 2007.

MALHADO, A.; COSTA, M. Seasonal leaf dynamics in an Amazonian tropical forest. **Forest Ecology and Management**, v. 258, n.7, p.1161-1165, 2009.

MALHI, Y. et al. Climate change, deforestation, and the fate of the Amazon. **Science**, v. 319, n. 5860, p. 169-172, 2008.

MALHI, Y. et al. Exploring the likelihood and mechanism of a climate-change-induced dieback of the Amazon rainforest. **Proceedings of the National Academy of Sciences of the United States of America**, v. 106, n. 49, p. 20610–5, 8 dez. 2009.

MARENGO, J. A. et al. The drought of Amazonia in 2005. **Journal of Climate**, v. 21, n. 3, p. 495–516, fev. 2008.

MARENGO, J. A. et al. The drought of 2010 in the context of historical droughts in the Amazon region. **Geophysical Research Letters**, v. 38, n. 12, 2011.

MEIR, P. et al. The fate of assimilated carbon during drought: impacts on respiration in Amazon rainforests. **Philosophical transactions of the Royal Society of London. Series B, Biological sciences**, v. 363, n. 1498, p. 1849–55, 2008.

MORTON, D. C. et al. Amazon forests maintain consistent canopy structure and greenness during the dry season. **Nature**, v. doi:10.103, n. 7487, p. 221–4, fev. 2014.

MOURA, Y. M. et al. Use of MISR/Terra data to study intra- and inter-annual EVI variations in the dry season of tropical forest. **Remote Sensing of Environment**, v. 127, p. 260–270, dez. 2012.

MYNENI, R. . et al. Global products of vegetation leaf area and fraction absorbed PAR from year one of MODIS data. **Remote Sensing of Environment**, v. 83, n. 1-2, p. 214–231, nov. 2002.

MYNENI, R. B. et al. Large seasonal swings in leaf area of Amazon rainforests. **Proceedings of the National Academy of Sciences of the United States of America**, v. 104, n. 12, p. 4820–3, 20 mar. 2007.

NÆSSET, E. Estimating timber volume of forest stands using airborne laser scanner data. **Remote Sensing of Environment**, v. 61, n. 2, p. 246–253, ago. 1997a.

NÆSSET, E. Estimating timber volume of forest stands using airborne laser scanner data. **Remote Sensing of Environment**, v. 61, n. 2, p. 246–253, ago. 1997b.

NÆSSET, E. Predicting forest stand characteristics with airborne scanning laser using a practical two-stage procedure and field data. **Remote Sensing of Environment**, v. 80, n. 1, p. 88–99, abr. 2002a.

NÆSSET, E. Predicting forest stand characteristics with airborne scanning laser using a practical two-stage procedure and field data. **Remote Sensing of Environment**, v. 80, n. 1, p. 88–99, abr. 2002b.

NEGRÓN JUÁREZ, R. I. et al. An improved estimate of leaf area index based on the histogram analysis of hemispherical photographs. **Agricultural and Forest Meteorology**, v. 149, n. 6-7, p. 920–928, jun. 2009.

NEPSTAD, D. C. et al. The role of deep roots in the hydrological and carbon cycles of Amazonian forests and pastures. **Nature**, v. 372, n. 6507, p. 666–669, dez. 1994.

PALACE, M. W. et al. Estimating forest structure in a tropical forest using field measurements, a synthetic model and discrete return lidar data. **Remote Sensing of Environment**, v. 161, p. 1–11, maio 2015.

PANG, Y. et al. Temperate forest height estimation performance using ICESat GLAS data from different observation periods. **Remote Sensing and Spatial Information Sciences**. v. 37, 1 jan. 2008.

PERSSON, A.; HOLMGREN, J.; SÖDERMAN, U. Detecting and measuring individual trees using an airborne laser scanner. **Photogrammetric engineering and remote sensing**, v. 68, n. 9, p. 925–932, 2002.

PHILLIPS, O. L. et al. **Drought sensitivity of the Amazon Rainforest**. Disponível em: <<http://www.sciencemag.org/content/323/5919/1344.full.pdf>>. Acesso em: 5 ago. 2014.

POPESCU, S. C. et al. Satellite lidar vs. small footprint airborne lidar: Comparing the accuracy of aboveground biomass estimates and forest structure metrics at footprint level. **Remote Sensing of Environment**, v. 115, n. 11, p. 2786–2797, nov. 2011.

RANSON, K. J. et al. Sun-view angle effects on reflectance factors of corn canopies. **Remote Sensing of Environment**, v. 18, n. 2, p. 147–161, out. 1985.

RAUTIAINEN, M. Retrieval of leaf area index for a coniferous forest by inverting a forest reflectance model. **Remote Sensing of Environment**, v. 99, n. 3, p. 295–303, 30 nov. 2005.

READING, R. P.; BEDUNAH, D. J.; AMGALANBAATAR, S. **Rangelands of Central asia**: proceedings of the conference on transformations, issues, and future challenges. Fort Collins, CO: Department of Agriculture, Forest Service, Rocky Mountain Research Station, 2006

REMER, L. A. et al. The MODIS Aerosol Algorithm, Products, and Validation. **Journal of the Atmospheric Sciences**, v. 62, n. 4, p. 947–973, 24 abr. 2005.

RESTREPO-COUBE, N. et al. What drives the seasonality of photosynthesis across the Amazon basin? A cross-site analysis of eddy flux tower measurements from the Brasil flux network. **Agricultural and Forest Meteorology**, v. 182-183, p. 128–144, dez. 2013.

ROSS, I. The radiation regime and architecture of plant stands. **Springer Science & Business Media**, 2012.

ROUJEAN, J.-L. Global mapping of vegetation parameters from POLDER multiangular measurements for studies of surface-atmosphere interactions: A pragmatic method and its validation. **Journal of Geophysical Research**, v. 107, n. D12, p. 4150, 2002.

ROUJEAN, JEAN-LOUIS, LEROY, MARC, DESCHAMPS, P.-Y. A bidirectional reflectance model of the earth's surface for the correction of remote sensing data. **Journal of Geophysical Research**, v. 97, n. 92, 1992.

SAATCHI, S. et al. Persistent effects of a severe drought on Amazonian forest canopy. **Proceedings of the National Academy of Sciences of the United States of America**, v. 110, n. 2, p. 565–70, 2013.

SAATCHI, S. S. et al. Benchmark map of forest carbon stocks in tropical regions across three continents. **Proceedings of the National Academy of Sciences of the United States of America**, v. 108, n. 24, p. 9899–904, 2011.

SALESKA, S. R. et al. Amazon forests green-up during 2005 drought. **Science (New York, N.Y.)**, v. 318, n. 5850, p. 612, 2007a.

SALESKA, S. R. et al. Amazon forests green-up during 2005 drought. **Science (New York, N.Y.)**, v. 318, n. 5850, p. 612, 2007b.

SAMANTA, A. et al. Amazon forests did not green-up during the 2005 drought. **Geophysical Research Letters**, v. 37, n. 5, 2010.

SAMANTA, A. et al. Seasonal changes in leaf area of Amazon forests from leaf flushing and abscission. **Journal of Geophysical Research**, v. 117, 2012a.

SAMANTA, A. et al. Why Is Remote Sensing of Amazon Forest Greenness So Challenging? **Earth Interactions**, v. 16, n. 7, 2012b.

SAMANTA, A.; GANGULY, S.; MYNENI, R. B. MODIS Enhanced Vegetation Index data do not show greening of Amazon forests during the 2005 drought. **The New phytologist**, v. 189, n. 1, 2011.

SCHAAF, C. B. et al. First operational BRDF, albedo nadir reflectance products from MODIS. **Remote Sensing of Environment**, v. 83, n. 1-2, p. 135–148, 2002.

SCHURR, F. M. et al. How to understand species' niches and range dynamics: a demographic research agenda for biogeography. **Journal of Biogeography**, v. 39, n. 12, p. 2146–2162, 2012.

SCHUTZ, B. E. et al. Overview of the ICESat Mission. **Geophysical Research Letters**, v. 32, n. 21, 2005.

SCURLOCK, J. M. O.; ASNER, G. P.; GOWER, S. T. Global leaf area index from field measurements, 1932-2000. **Data set. Available on-line [http://www.daac.ornl.gov] from Oak Ridge National Laboratory Distributed Active Archive Center, Oak Ridge, Tennessee, U.S.A., 2001.**

SHAW, R. H.; PEREIRA, A. . Aerodynamic roughness of a plant canopy: A numerical experiment. **Agricultural Meteorology**, v. 26, n. 1, p. 51–65, 1982.

SHUKLA, J.; NOBRE, C.; SELLERS, P. Amazon deforestation and climate change. **Science**, v. 247, n. 4948, p. 1322–1325, 1990.

SILVA, F. B. et al. Large-scale heterogeneity of Amazonian phenology revealed from 26-year long AVHRR/NDVI time-series. **Environmental Research Letters**, v. 8, n. 2, 2013a.

SILVA, F. B. et al. Large-scale heterogeneity of Amazonian phenology revealed from 26-year long AVHRR/NDVI time-series. **Environmental Research Letters**, v. 8, n. 2, 2013b.

SIMS, D. A. et al. Seasonal and inter-annual variation in view angle effects on MODIS vegetation indices at three forest sites. **Remote Sensing of Environment**, v. 115, n. 12, 2011.

STARK, S. C. et al. Amazon forest carbon dynamics predicted by profiles of canopy leaf area and light environment. **Ecology letters**, v. 15, n. 12, p. 1406–14, 2012.

STEEGE, H. TER; PITMAN, N. A spatial model of tree α -diversity and tree density for the Amazon. **Biodiversity & Conservation**, v.12, p. 2255 - 2277, 2003.

STRAHLER, A. H.; MULLER, J. P. MODIS BRDF Albedo product : algorithm theoretical basis document. **MODIS Product ID: MOD43**, v. Version 5., n. April, p. 1–53, 1999.

STRAHLER, A. H. Vegetation canopy reflectance modeling—recent developments and remote sensing perspectives*. **Remote Sensing Reviews**, v. 15, n. 1-4, p. 179–194, out. 2009a.

STRAHLER, A. H. Vegetation canopy reflectance modeling—recent developments and remote sensing perspectives*. **Remote Sensing Reviews**, v. 15, n. 1-4, p. 179–194, 19 out. 2009b.

STRAHLER, A.; JUPP, D. Modeling bidirectional reflectance of forests and woodlands using Boolean models and geometric optics. **Remote Sensing of Environment**, 1990.

STYSLEY, P. R. et al. Long term performance of the High Output Maximum Efficiency Resonator (HOMER) laser for NASA's Global Ecosystem Dynamics Investigation (GEDI) lidar. **Optics & Laser Technology**, v. 68, p. 67–72, 2015.

SUN, G. et al. Forest vertical structure from GLAS: An evaluation using LVIS and SRTM data. **Remote Sensing of Environment**, v. 112, n. 1, p. 107–117, 2008.

TER STEEGE, H. et al. Continental-scale patterns of canopy tree composition and function across Amazonia. **Nature**, v. 443, n. 7110, p. 444–447, 2006.

TOWNSEND, A. R.; ASNER, G. P.; CLEVELAND, C. C. The biogeochemical heterogeneity of tropical forests. **Trends in ecology & evolution**, v. 23, n. 8, p. 424–31, 2008.

TUCKER, C. J. Red and photographic infrared linear combinations for monitoring vegetation. **Remote Sensing of Environment**, v. 8, n. 2, p. 127–150, 1979.

VERSTRAETE, M. M.; PINTY, B.; MYNENI, R. B. Potential and limitations of information extraction on the terrestrial biosphere from satellite remote sensing. **Remote Sensing of Environment**, v. 58, n. 2, p. 201–214, 1996.

VIEIRA, S. et al. Forest structure and carbon dynamics in Amazonian tropical rain forests. **Oecologia**, v. 140, n. 3, p. 468–79, 2004.

VILLAR, E. C. J. et al. Spatio-temporal rainfall variability in the Amazon basin countries (Brazil , Peru , Bolivia , Colombia , and Ecuador). **International Journal of Climatology**, v. 1594, n. December 2008, p. 1574–1594, 2009.

VOURLITIS, G. L. et al. Variations in evapotranspiration and climate for an Amazonian semi-deciduous forest over seasonal, annual, and El Niño cycles. **International journal of biometeorology**, v. 59, n. 2, p. 217–30, 2015.

WAGNER, F. et al. Asynchronism in leaf and wood production in tropical forests: a study combining satellite and ground-based measurements. **Biogeosciences**, v. 10, n. 11, p. 7307–7321, 2013.

WAGNER, F. et al. Pan-tropical analysis of climate effects on seasonal tree growth. **PloS one**, v. 9, n. 3, p. e92337, 2014.

WALTHALL, C. L. A Study of Reflectance Anisotropy and Canopy Structure Using a Simple Empirical Model. **Remote Sensing of Environment**, v. 128, n. May 1995, p. 118–128, 1997.

WANG, Y. et al. Assessment of biases in MODIS surface reflectance due to Lambertian approximation. **Remote Sensing of Environment**, v. 114, n. 11, p. 2791–2801, 2010.

WANNER, W.; LI, X.; STRAHLER, A. H. On the derivation of kernels for kernel-driven models of bidirectional reflectance. **Journal of Geophysical Research**, v. 100, n. D10, p. 21077, 1995.

WIDLOWSKI, J.-L. et al. Canopy Structure Parameters Derived from Multi-Angular Remote Sensing Data for Terrestrial Carbon Studies. **Climatic Change**, v. 67, n. 2-3, p. 403–415, 2004.

WIDLOWSKI, J.-L. et al. Using 1-D models to interpret the reflectance anisotropy of 3-D canopy targets: issues and caveats. **IEEE Transactions on Geoscience and Remote Sensing**, v. 43, n. 9, p. 2008–2017, 2005a.

WIDLOWSKI, J.-L. et al. Using 1-D models to interpret the reflectance anisotropy of 3-D canopy targets: issues and caveats. **IEEE Transactions on Geoscience and Remote Sensing**, v. 43, n. 9, p. 2008–2017, 2005b.

WILLIAMS, M. et al. Seasonal variation in net carbon exchange and evapotranspiration in a Brazilian rain forest: a modelling analysis. **Plant, Cell and Environment**, v. 21, n. 10, p. 953–968, 1998.

WOLFE, R. E. et al. Achieving sub-pixel geolocation accuracy in support of MODIS land science. **Remote Sensing of Environment**, v. 83, n. 1-2, p. 31–49, 2002a.

WOLFE, R. E. et al. Achieving sub-pixel geolocation accuracy in support of MODIS land science. **Remote Sensing of Environment**, v. 83, n. 1-2, p. 31–49, 2002b.

WULDER, M. A. et al. Lidar sampling for large-area forest characterization: A review. **Remote Sensing of Environment**, v. 121, p. 196–209, 2012.

XU, L. et al. Widespread decline in greenness of Amazonian vegetation due to the 2010 drought. **Geophysical Research Letters**, v. 38, n. 7, 2011.

YU, Y.; YANG, X.; FAN, W. Estimates of forest structure parameters from GLAS data and multi-angle imaging spectrometer data. **International Journal of Applied Earth Observation and Geoinformation**, v. 38, p. 65–71, 2015.

ZANCHI, F. B. et al. Estimativa do Índice de Área Foliar (IAF) e Biomassa em pastagem no estado de Rondônia, Brasil. **Acta Amazonica**, v. 39, n. 2, p. 335–347, 2009.

ZELAZOWSKI, P. et al. Reconciling satellite-derived atmospheric properties with fine-resolution land imagery: Insights for atmospheric correction. **Journal of Geophysical Research**, v. 116, n. D18, p. D18308, 2011.

ZHANG, Y. et al. Assessing the information content of multiangle satellite data for mapping biomes. **Remote Sensing of Environment**, v. 80, n. 3, p. 418–434, 2002.

ZWALLY, H. J. et al. ICESat's laser measurements of polar ice, atmosphere, ocean, and land. **Journal of Geodynamics**, v. 34, n. 3-4, p. 405–445, 2002.